UNIVERSITÀ DEGLI STUDI DI PADOVA

UNIVERSITA' DEGLI STUDI DI PADOVA

Dipartimento di Ingegneria Industriale DII

Corso di Laurea Magistrale in Ingegneria dei Materiali

Spinodal decomposition in Alnico alloys

Relatori: prof.ssa Calliari Irene
prof. Mészáros István

Demchan Andriy
2027549

ANNO ACCADEMICO 2021-2022

Abstract

The following study aims to investigate spinodal decomposition in Alnico alloys. Spinodal decomposition is a phase separation process which occurs in several materials at the nanometer level. Alnico alloys, made up mostly of aluminum, nichel, cobalt and iron, are a material where in certain condition spinodal decomposition can arise and bring some important changes in properties. In particular, coercivity development is investigated as a consequence of the process. Furthermore, the importance of the magnetic properties of Alnico alloys is illustrated through the context of geopolitical crisis around rare earth elements and permanent magnets. These are the premises of the study.

The work consists in heat treatments of the samples of two different Alnico alloys. There are three experiments which have been built up during the investigations so there are also three corresponding sets of samples as the experiments are irreversible. After the heat treatments, several investigation techniques are applied in order to characterize the samples. As it was already mentioned, the main purpose of this stage is to investigate the spinodal decomposition process. Thus, hardness tests, magnetic tests, optical microscopy, electronic microscopy and EDS composition analysis were done. Moreover, some other studies are done on the outputs. Finally, all the results are discussed, and new suggestions are done fur the further studies.

Several difficulties were encountered during the experimental phase of the work. The results of the magnetic test of the first and the third sets of samples were found to be completely different from the expected ones. The results were analyzed, and those experiments were defined failed. Thus, other investigations had been conducted during the study on the failure. As a consequence, some important changes had been done on the equipment and on the experimental conditions. Also, a theoretical background supports every result and every action.

The experimental part of this work was carried out in Budapest, at the BME - Budapesti Műszaki és Gazdaságtudományi Egyetem - University of Budapest, in the Department of Materials Science & Engineering under the supervision of Professor Mészáros István.

Summary

1 CHAPTER 1

SPINODAL DECOMPOSITION AND ALNICO ALLOYS

Spinodal decomposition is a process of phase transformation which takes place when certain parameters and conditions are satisfied. This phenomenon can occur in several classes of materials: Alnico alloys are one of these classes. In this chapter the topic Spinodal Decomposition and the topic Alnico alloys are introduced as they are the theoretical base of the following project.

1.1 SPINODAL DECOMPOSITION

1.1.1 Introduction

Spinodal decomposition is a mechanism by which a solution of two or more components separates in two or more distinct phases with different chemical compositions and physical properties but maintains basically the same crystal structure. Typically, it transforms a homogeneous solid solution into an inhomogeneous solid solution in the nanoscale. It requires no nucleation, the initiation of the two new phases occurs by composition fluctuation and the growth of the fluctuations occurs by uphill diffusion, or diffusion with a negative coefficient. The reasons of this transformation can be found analyzing the phase diagram of miscibility gap and the corresponding free energy curve. The spinodal decomposition occurs uniformly through the material, and it provides a very finely dispersed microstructure that can significantly enhance the physical properties of materials.

The process of the spinodal decomposition is of primary interest as due to its simplicity it is possible to describe it through quantitative theory and modelling. Since there are no thermodynamic barriers to the reaction inside the spinodal region on the phase diagram, the composition occurs solely through diffusion. Hence, the process can be treated purely as a diffusion problem, and many of the characteristics of the decomposition can be described by an approximate analytical solution to the general equation. On the other hand, theories of nucleation and growth need thermodynamics of fluctuations, and the diffusion problem used to describe the process is more difficult to solve as it is unrealistic to linearize the diffusion equation.

1.1.2 Phase Diagram and Free Energy Diagram Analysis

A phase diagram is a type of chart used to show conditions (pression, temperature, concentration, etc.) at which thermodynamically distinct phases occur and coexist at equilibrium. The diagram is useful to show the phase separation in the spinodal decomposition.

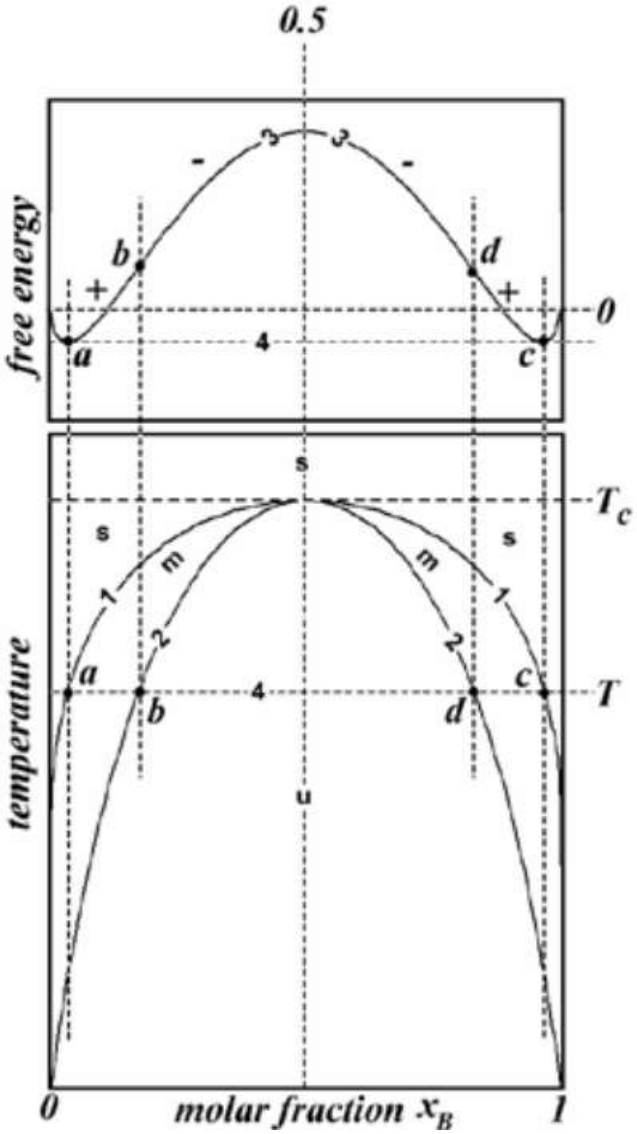

Figure 1: A phase diagram with a miscibility gap (lower frame) and a diagram of the free energy of mixing change (upper frame).[34] *At a given temperature (T) the tie line (4) cuts the phase boundary and the spinodal at points (a,c) and (b,d), respectively. The changes in the free energy of mixing (ΔG), at this given temperature, in respect to x_B are shown by line (3) in the upper frame. Segments (ab) and (cd) correspond to a positive second derivative of ΔG, $\partial^2\Delta G/x_B>0$, while segment (bd) to a negative one, $\partial^2\Delta G/x_B<0$. At points (b) and (d) $\partial^2\Delta G/x_B=0$, these points are called spinodes.*

The phase diagram of *Figure1* is a temperature versus molar fraction diagram of a component x_B. The diagram is symmetrical around x_B=0.5 which is the case of regular solution model. Before analyzing how the diagram is built, it's important to set the technical terms for the main regions and curves:

- *Miscibility Gap*: area within the coexistence curve of an isobaric or an isothermal phase diagram. On an isobaric diagram, a miscibility gap is observed at temperatures below an upper critical solution temperature (UCST) or above the lower critical solution temperature (LCST). Its location depends on the pressure set for the diagram. In the miscibility gap, there are at least two phases coexisting.
- *Binodal Curve* or *Coexistence Curve (curve 1)*: it is a curve that defines the region of composition and temperature in a phase diagram for a binary mixture across which a

transition occurs from miscibility of the components to the condition where single-phase mixtures are metastable or instable.

- *Spinodal Curve (curve 2):* it is a curve that separates the metastable region from the unstable region in the coexistence region of the mixture. Outside from the spinodal region (m), the region between the spinodal curve and the binodal curve, the process of moving towards equilibrium through phase separation occurs by droplets nucleation and growing, while inside the spinodal region (u), defined by spinodal curve, there are periodic modulations of the order parameter which have a small amplitude at first (as known as Spinodal Decomposition). Spinodal curve is not a sharp boundary in real systems as result of fluctuations.
- *Spinodes:* inflection points on the free energy curve where the second derivative of ΔG is zero.

According to the theory of Gibbs, the condition for metastable state of a phase is that the second derivative of the free energy of mixing with respect to molar fraction must be positive. If the derivative is negative than the system is unstable. If zero, the spinodal is defined. The free energy of mixing has the following general forms:

$$\Delta \mathrm{G}^{mix} = \Delta \mathrm{H}^{mix} - T\Delta \mathrm{S}^{mix} \quad (1)$$

As the regular solution model states, the entropy of mixing is the same as for the ideal mixing; $\Delta S^{mix}=-R(X_A \ln X_A + X \ln X_B)$, where X_A and X_B are the molar fractions of components A and B in the mixture ($X_A+X_B=1$). Furthermore, the enthalpy of mixing can be written as $\Delta H^{mix}=X_A X_B \beta$, where β is an interaction parameter lumping the energy of mixing contribution (for the ideal solution the enthalpy of mixing is zero). Under these assumptions, eq. (1) becomes:

$$\Delta \mathrm{G}^{mix} = \mathrm{X}_A \mathrm{X}_B \beta + \mathrm{RT}(\mathrm{X}_A \ln \mathrm{X}_A + \mathrm{X} \ln \mathrm{X}_B) \quad (2)$$

The miscibility-gap and spinodal-region boundaries are obtained by calculating the first and second derivative of the free energy, respectively, and setting them equal to zero. In *Figure 1* (upper frame) the first derivative is zero at the two free energy minima corresponding to the two immiscible phases and the second derivative is zero at the points of inflexion. It must be noticed that also at the free energy maximum both of derivatives are zero. For several values of temperatures, the locus of the free energy minima projected on a temperature-composition diagram defines the phase boundary and the locus of the points of inflexion defines the spinodal curve.[9]

1.1.3 Spinodal Decomposition versus Nucleation and Growth

A qualitative phase diagram for a substance which could undergo the process of spinodal decomposition has been shown. Nevertheless, for the occurring of this process the substance must follow a certain path on the temperature versus concentration (or molar fraction) diagram.

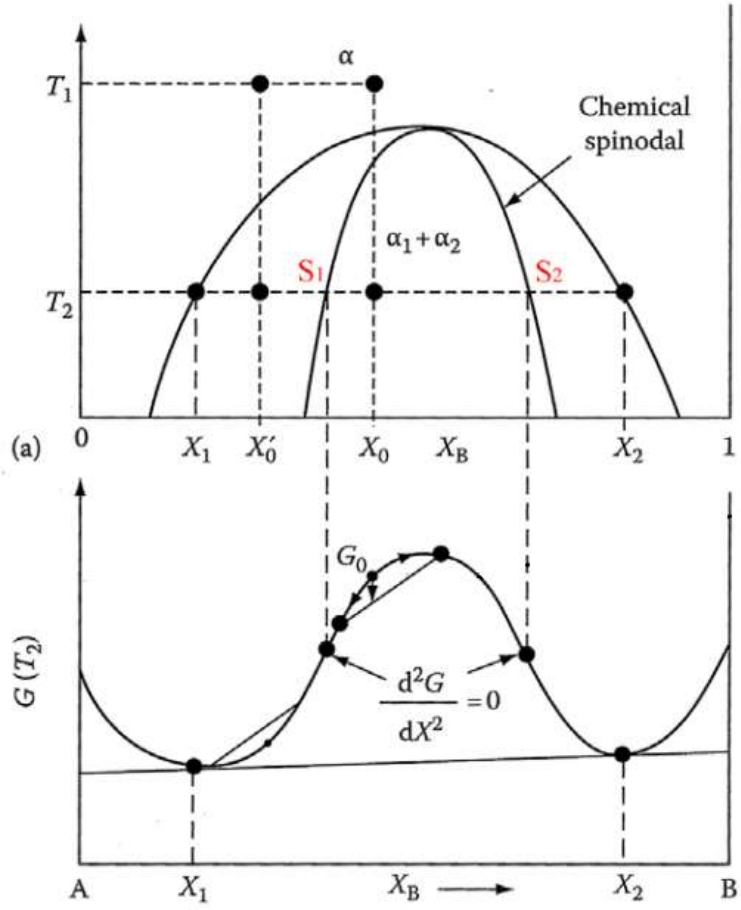

Figure 2: Phase diagram (upper frame) and free energy diagram (lower frame). In the figure two different paths are showed to distinguish nucleation and growth phase transformation and spinodal decomposition phase transformation.[9]

Not all the substances manifest the spinodal decomposition, it depends on the intrinsic nature and properties of the substance, and it can be checked analyzing its free energy in different conditions on the phase diagram. For the alloys which can manifest the spinodal decomposition an important parameter is the composition. Temperature and the path, in terms of time, from one temperature to another temperature are also critical. In general, certain conditions must be satisfied to see the process of spinodal decomposition occur.

From the *Figure 2*, if the substance with the composition of X_0 is solution heat treated to the temperature T_1 and then quenched to a lower temperature T_2, the composition will be initially the same everywhere and the free energy of the substance in those conditions G_0 on the G curve in the following diagram. Under these conditions the alloys will be suddenly unstable because small fluctuations in composition that produce A-rich and B-rich regions will cause total free energy to decrease. Therefore, up-hill diffusion takes place until the equilibrium compositions X_1 and X_2 are reached. This is the spinodal decomposition process.

In comparison, if a substance doesn't belong to the spinodal region composition (this is the case of the X'_0 composition in *Figure 2*), and it is solution heat treated at a high temperature T_1 and then quenched to T_2, small fluctuations will lead to an increase of the free energy of the system, so the substance state is defined metastable. The phase transformation needs the formation of stable

nuclei, with a composition very different from the matrix, to occur. Hence, in the binodal region but outside the spinodal region the transformation must proceed by a process of nucleation and growth.

It has been shown that phase separation occurs if the substance is within the miscibility gap. If the system is in the metastable region than the mechanism is by nucleation and growth whereas if it is in the unstable region, then it occurs by spinodal decomposition. The two different processes are shown in the figure below.

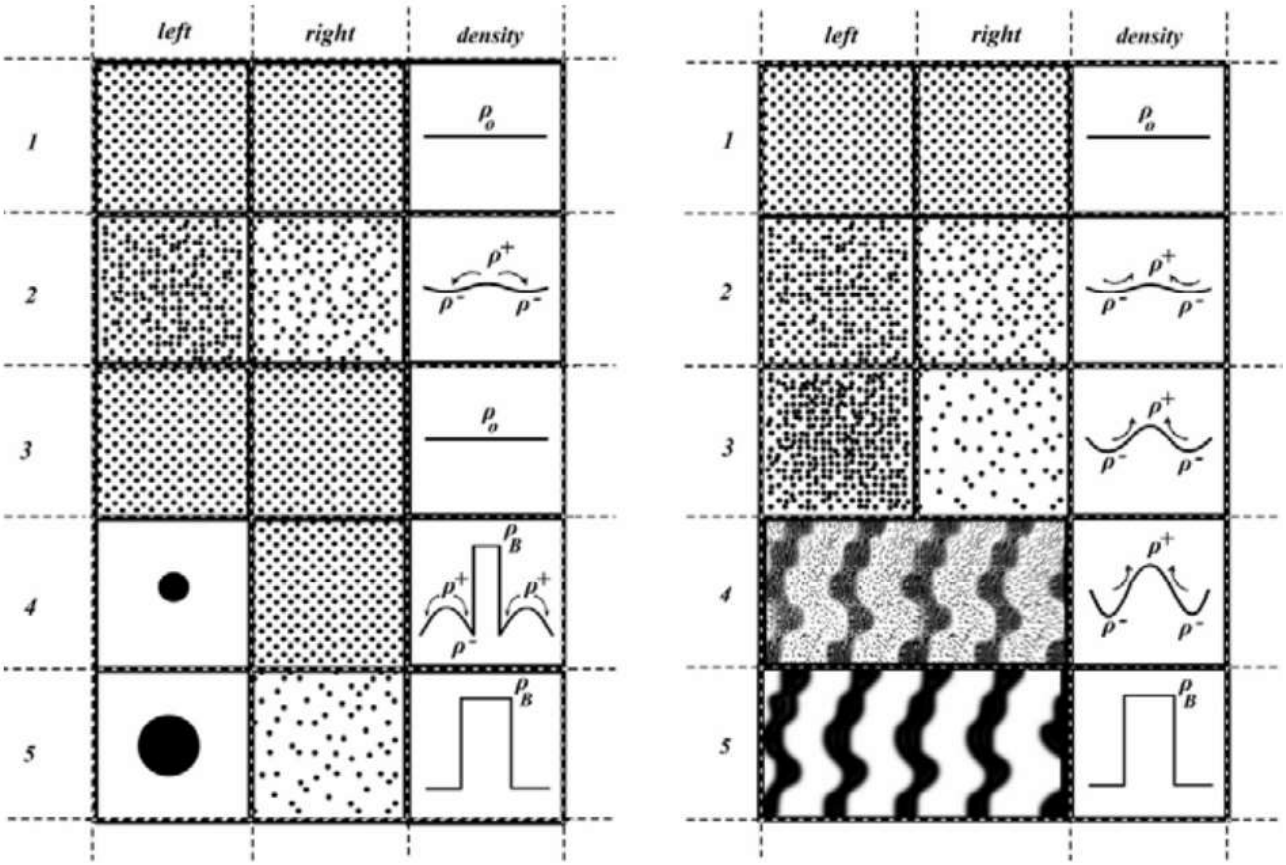

Figure 3 Nucleation and growth process (left) and Spinodal decomposition process (right) [9]

The columns ''left' and ''right'' represent two adjacent regions of a solution while the column density represent the local concentration of the solute. The rows show the evolution stages of the solution in time when some small or big fluctuations take place.

On the left side of the *Figure 3*, nucleation and growth process is shown. Initially, the solution has been brought in the metastable region and the local concentration is constant. In the second stage a small fluctuation occurs but the solution needs to overcome a bigger energy barrier to form two distinct phases, so the diffusion brings the composition locally constant again and the phase transformation is suppressed. The third stage basically represents the initial condition. At the fourth stage a larger fluctuation occurs and it causes the formation of a nucleus of a critical size. Down-hill diffusion takes place now from the right region to the left region. To be noticed that the nucleus is not considered in the calculation of the concentration gradient. Once the solute reaches the nucleus through diffusion process and the equilibrium of the system is established than the separation of the phases is terminated. This process is known as nucleation and growth.

On the right side of the *Figure 3*, spinodal decomposition process is shown. Initially, the solution is taken to the unstable region and the local concentration is constant. In the second stage a small fluctuation occurs. The system is in the unstable place and small fluctuations decrease the free energy, so the up-hill diffusion starts to decrease furthermore the free energy of the system. The diffusion progresses and the concentration increases until it reaches the equilibrium concentrations of the system. This is how the spinodal decomposition phase separation process occurs.

1.1.4 Cahn-Hilliard Model for the Kinetics of Phase Separation

1.1.4.1 Introduction

Since there is no thermodynamic barrier to the reaction, spinodal decomposition is controlled solely by diffusion. Hence, the process can be treated as a diffusion problem and many of features of the decomposition can be provided by an approximate analytical solution to the general diffusion equation. In contrast, theories of nucleation and growth must invoke the thermodynamics of fluctuations and the solving of the diffusion is equation is unrealistic as the equation is not linear. As a result, some quantitative models are available to describe the process.

1.1.4.2 Historical background

The growth of a composition modulation in an initially homogeneous alloy implies up-hill diffusion or a negative diffusion coefficient. Becker and Dehlinger had already predicted a negative diffusivity inside the spinodal region of a binary system. Nevertheless, their treatments could not account for the growth of a modulation of particular wavelength (λ), such as was observed in the Cu-Ni-Fe alloy. In fact, any model based on Fick's law yields a physically unacceptable solution when the diffusion coefficient is negative. The first explanation of the periodicity was given by Mats Hillert, a Swedish metallurgist, in 1955. Starting with a regular solution model, he derived a flux equation for one-dimensional diffusion on a discrete lattice. This equation differed from the usual one by the inclusion of a term which allowed for the effect on the driving force of the interfacial energy between adjacent inter-atomic planes that differed in composition. Hillert solved the flux equation numerically and found that inside the spinodal it yielded a periodic variation of composition with distance. Furthermore, the wavelength of the modulation was of the same order as that observed in the Cu-Ni-Fe alloys. A more flexible continuum model was subsequently developed by John W. Cahn, an American scientist, who included the effects of coherency strains as well as the gradient energy term. The strains are significant in that they dictate the ultimate morphology of the decomposition in anisotropic materials. [33]

1.1.4.3 From Fick equation to Cahn-Hillard equation

As it has been discussed above, spinodal decomposition is a diffusion problem and it admits an analytical solution. Diffusion problems are treated with Fick laws but in this case Fick laws are not able to describe properly the process.

There are two Fick laws in Thermodynamics to describe diffusion phenomenon, they are showed below in the *eq. 3* and *eq. 4*.

$$J(x,t) = -D\nabla c(x,t) \tag{3}$$

$$\frac{\partial c}{\partial t} = -\nabla \cdot (D\nabla c) \tag{4}$$

For the purpose of describing the spinodal decomposition process, Fick's equations do not produce the expected results as they do not predict any phase separation. As can be seen from the phase diagrams already discussed, a thermodynamic system, initially single-phase, brought within the miscibility gap should manifest phase separation. Notably, moreover, if the initial state of the system is within the spinodal region, the separation process is also spontaneous. In contrast to these observations, Fick's law predicts a final state with uniform composition as the thermodynamic equilibrium state, whether the system initially lies within the spinodal region or not.

Fick's equation predicts diffusion according to a concentration gradient of the chemical species involved. The process also goes on until the concentration of the chemical species present is uniform. The thermodynamic equilibrium condition, therefore, produces a single-phase system in which the same atomic structure is repeated throughout the system, with no interfaces or local thickening of concentration of one chemical species over another. From the atomic point of view, the structures present in *Figure 4* (left) are energetically preferred to those in *Figure 4* (right).

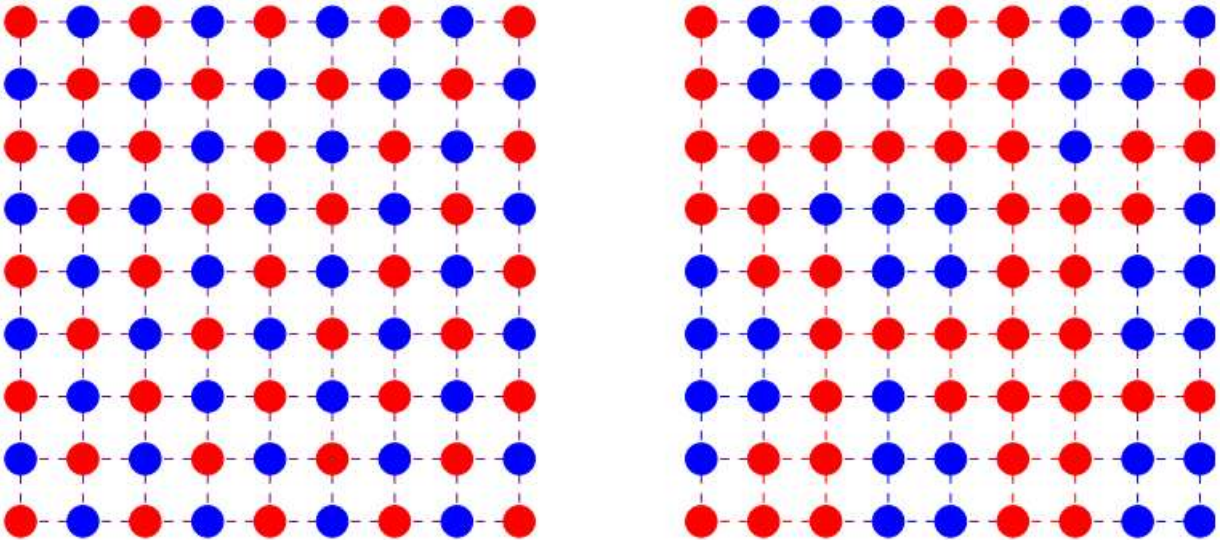

Figure 4 Fick diffusion equilibrium configuration (left): both concentration of component A (blue) and component B (red) are locally uniform, so the average concentration of the system is uniform. Thermodynamic order diffusion (right): regions rich of component A (blue) and regions rich of component B (red) are present according to the phase diagram.

What has not been examined in the discussion made by Fick's equation are the interfaces at the boundaries of the domains that are formed in response to the generation of two distinct phases. In order to include the interfaces between the phases and the energy associated with them, it is necessary to introduce an appropriate term describing the free energy density of the system. The interface formed between regions rich in chemical species A and regions rich in chemical species B are described by the *excess internal energy* of the system, which, expressed per unit area has the dimensions of a voltage surface area. In other words, the energy associated with the interface expresses the work that the system performs to construct the interface. The new term introduced is

$$\sigma = \Delta c\sqrt{2Kg_0^{max}} \ , \tag{5}$$

where K and g_0^{max} are typical characteristics of a material. K, being related to the energy density of the system, considers how the energy contained in the system is distributed between regions of constant composition (of one phase or the other) and interfaces while g_0^{max} considers the interaction between the chemical components.

Moreover, as spinodal decomposition is a diffusive process that belongs to the group of phase transformations to describe and analyze the phenomenon correctly, it is necessary to find an expression for the *diffusive potential* responsible of the flux of components of the chemical species involved. Once this is done, the Cahn-Hilliard equation is derived to describe the spatio-temporal evolution of the chemical composition of the solution. Considering binary solutions, the order parameter of the transformation is given by the concentration of components of only one of the two chemical species present, as the other is determined by the normalization condition. The new term expressing the diffusive potential is:

$$\Phi(x) = \frac{dg_0}{dc_2}(c_2) - 2K\nabla^2 c_2 \, . \tag{6}$$

Once the diffusive potential, that can predict a situation of thermodynamic equilibrium in the presence of a non-uniform concentration profile, is provided it is possible to obtain the equation that describes the spatio-temporal evolution of the process, known as the Cahn-Hilliard equation. In terms of the thermodynamic mobility of the species involved, for a binary compound, Fick's first equation for diffusion is written as

$$J = -M \cdot \frac{\partial^2 g}{\partial^2 c_2^2} \cdot \nabla c_2 = -D \cdot \nabla c_2 \, . \tag{7}$$

To be noticed that this procedure manages to predict an interdiffusivity provided with an algebraic sign, dependent on the sign of the second derivative of the free energy density (linked with the concavity present in the graph of free energy as a function of composition). In terms of the mobility M, it is therefore possible to describe a diffusion process either when $\frac{\partial^2 g}{\partial^2 c_2^2}$ is positive and a diffusion according to the concentration gradient takes place, or a diffusion process in which $\frac{\partial^2 g}{\partial^2 c_2^2}$ is negative and instead diffusion takes place against the concentration gradient. The term second gradient refers to the fact that a chemical species spontaneously tends to diffuse from an area of high concentration to an area where its concentration is lower. Conversely, the term counter gradient indicates the tendency of a chemical species to be recalled from a zone of low concentration to one of higher concentration. This second case is what occurs during a spinodal decomposition process: regions rich in chemical species A become richer in A and regions rich in B species become richer in B. In both cases, mobility is defined as positive in accordance with the principle fundamental of irreversible thermodynamics that the rate of production of entropy density is nonnegative.

In the condition of no other forces capable of generating component flows, the chemical potential is responsible for the motion of species in solution. From this observation we can identify the diffusive potential with the chemical potential, as follows:

$$\mu \equiv \Phi(x) \, , \tag{8}$$

where $\Phi(x)$ is given by the *eq. 6*. Being a function of the mobility M and of the chemical potential, Fick's equation for isotropic systems is given as:

$$
\begin{aligned}
J_2^{[V]} &= -M\nabla(\mu_2 - \mu_1) \\
&= -M\nabla\Phi(x) \\
&= -\frac{D}{\frac{\partial^2 g}{\partial^2 c_2^2}}\,\nabla\left[\frac{dg_0}{dc_2} - 2\nabla(Kc_2)\right].
\end{aligned} \tag{9}
$$

Finally, placing *eq.9* in the Fick's second law for the diffusion *Cahn-Hillard equation* for isotropic systems is obtain. Cahn-Hillard model is a differential equation with the partial derivatives of the fourth order.

$$
\frac{\partial c_2}{\partial \mathrm{t}} = \nabla \cdot \left\{ \frac{D}{\frac{\mathrm{d}^2 g_0}{dc_2^2}} \nabla\left[\frac{dg_0}{dc_2} - 2K\nabla^2 c_2\right] \right\}. \tag{10}
$$

The first is the diffusive term that also appeared in Fick's equation, while the second term, the one containing fourth order derivatives of the concentration profile, is a new one and it introduces the influence of the interfaces as a means of minimizing the internal energy of the system.[31]

1.1.5 Advantages

Spinodal decomposition is a process which changes the microstructure of the material in a particular way. Thus, several suggestions were proposed to exploit this phenomenon to enhance some material properties. Many different properties can be improved using spinodal decomposition, the most common are the mechanical and the magnetic ones.

Regarding to the mechanical properties, several different methods are used to improve them. Precipitation hardening, dispersion strengthening or spinodal decomposition are all valid strategies and they all provide the identical strength values. Nevertheless, there are important advantageous of using spinodal decomposition process. These are the followings:

- the decomposition-product phases have different chemical composition but mostly identical crystalline structure. The principal advantageous of this fact is that there are no local anodes and cathodes to deteriorate corrosion resistance.
- in spinodal decomposition there is no energy barrier to start the reaction. Nucleation and growing, on the other hand, need to overcome the nucleation energy barrier to proceed. Hence, if the radius of the nuclei is less than the critical value, the precipitate phases cannot be nucleated. As a result, the quenching rate and section size considerably influences enlarge of hardening in precipitation strengthening.
- it is homogeneous throughout the section
- spinodal alloys are not probable to over-age or to recrystallize

On the other hand, spinodal decomposition has been typically useful in the fabrication of stable magnet materials, because the morphologies favor high coercivities. The structure can be optimized by thermomechanical processing and magnetic aging. Permanent phase separation or spinodal decomposition appears to be important in the classic Alnicos and copper-nickel-iron alloys, as well as in the recently developed iron-chromium-cobalt materials. [7]

1.2 ALNICO MAGNETS

1.2.1 Rare earth crisis and permanent magnets

The brief geopolitical crisis in 2010 between China and Japan showed the world of the trade the quasi-monopoly of China on such an essential industry input as the rare earth elements are. Rare earth elements are seventeen elements on the periodic table that are divided into two categories: the more common *light earth* elements and the less abundant *heavy rare earth* elements. These elements are the linchpin ingredients of many high technologies for a wide variety of uses—ranging in application from military and medicine to entertainment, communications and petroleum refining, through to lighting and renewable energies. The "unique magnetic, luminescent, and electrochemical properties" of rare earths makes them almost indispensable to many of today's technologies; for example, when used as additives to permanent magnets, they endow resistance to demagnetization at high operating temperatures.[28]

At the moment, China controls almost the whole trade of the rare earth elements. The issue is not just that most extraction of heavy rare earths occurs in China but, more importantly, China has a near-monopoly on processing capacity and on the supply chains for converting the raw elements into end products. Whereas some extraction and processing of light rare earths does occur outside of China, for heavy rare earths it will take years—if not decades—to develop alternative supply chains. Last year, China produced about 97 percent of the rare earths mined on the planet. In recent years that country has been cutting back on the amount of rare earths it exports, reducing quotas by almost 40 percent in 2010.[29] Rising prices and a looming potential shortage have now ignited searches for alternatives to magnet technologies that chew up large amounts of rare earth.

There are two main strategies to overcome the shortage of rare earth elements: lessening the dependence on them or ensuring new supplies through recycling or new mining. In the meanwhile, several sectors affected by the crisis have to reinvent their products and supplies in order to overcome the crisis. The sector of permanent magnets will be discussed.

Rare earth permanent magnets are particularly important for clean energy applications and the automotive industry. The two most common rare earth magnets are Samarium Cobalt (Sm-Co) and Neodymium (Nd-Fe-B). Samarium-Cobalt magnets perform better at higher temperatures, but are brittle, which limits magnet size and shape and can cause problems with integration into certain applications, such as motors. On the other side, Neodymium–Iron–Boron magnets are even stronger than Samarium-Cobalt magnets and, because their size is not as restricted, they are more suitable for large applications, such as wind turbines and other electricity generators. Over the past few decades, China has pursued a concerted strategy to develop its refining and fabrication capacities and thus achieve the world's most integrated supply chain for permanent magnets and other products. At the moment, China is the only country with the capacity to process heavy rare earths. For this reason, new investigations on magnetic materials are stimulated in order to not to make something that can rival today's best magnets but something with a better bottom line for the properties used. The Ames Lab team is dusting off Alnico magnets, commercialized in the 1940s. Made mostly of aluminum, nickel, cobalt and iron, these magnets are reasonably hard but only about one-fifth as strong as the best rare earth magnets. Tweaking the structure of these magnets to line up the iron cobalt grains might up the density energy. In the figure below rare earth-based

magnets and classical magnets are shown with a comparison based on the main parameters of the magnetic materials.

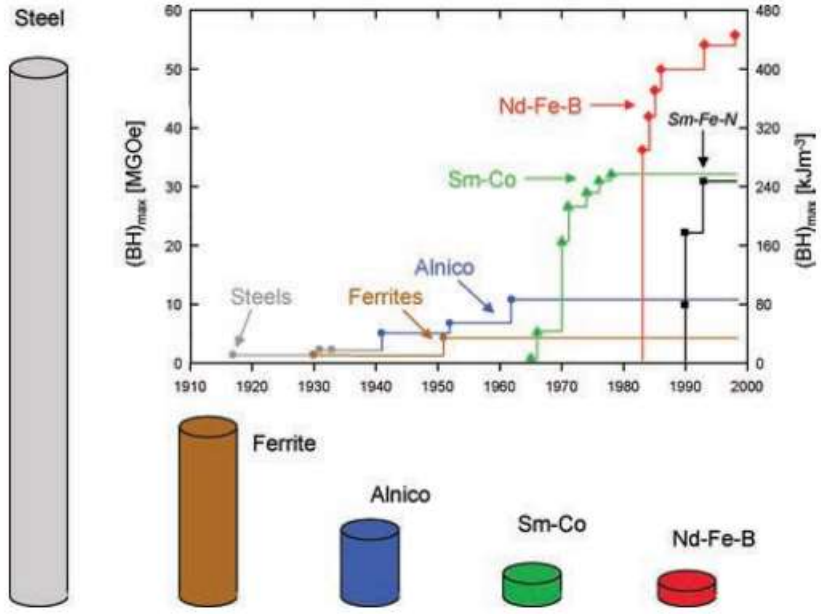

Figure 5 Development of hard magnetic materials in the 20th century: dependence of maximum magnetic energy $(BH)_{max}$[104]

The most significant features describing the performance of a permanent magnet are the remanence, the intrinsic coercivity and the maximum energy product, $(BH)_{max}$. This last can be identified as a key point: magnets with higher $(BH)_{max}$ require less volume to obtain given performance; magnet circuit designers should employ magnets of high $(BH)_{max}$ to reduce the size of their circuits. As it can be noticed from the *Figure5,* alnico alloys cannot compete with rare-earth based magnets, but they still represent the best alternative.

1.2.2 Milestones in the discovering of Alnico alloys

Alnico alloys are nanostructured permanent magnets were developed by Mishima in the 1930s. As the name implies, Alnico is an alloy of aluminum, nickel and cobalt along with iron and copper. Other elements such as silicon, titanium, columbium, zirconium, etc. are often added to achieve specific targets such as refinement of grain structure, improvement in coercivity, improvement in curve shape, inhibition of non-magnetic gamma-phase, etc. There are different grades for different Alnico compositions and they are characterized chiefly by their different magnetic properties. *Table 1* shows some of the milestones in the development of this class of alloys. Different types of alloys were developed in the period from 1931 (Alnico 3) to the 1956 (Alnico 8 and Alnico 9).

Present Designation and Original Constituents	Year First Reported	Reference	Typical Properties		
			$(BH)_m$ (MGOe)	H_{ci} (Oe)	B_r (G)
Alnico 3 (Al, Ni, Fe)	1931	Mishima [1]	1.4	490	6800
Alnico 4 (Al, Ni, Co, Fe)	1931	Mishima [2] Ruder [3]	1.4	700	5500
Alnico 2 (Al, Ni, Co, Fe, Ti)	1934	Horsburgh and Tetley [4]	1.7	560	7300
New KS (Al, Ni, Co, Fe, Ti) (Alnico 12)	1934	Honda et al. [5] Ruder [6]	2.0	790	7200
Alnico 5 (Al, Ni, Cu, Co, Fe)	1938	Oliver and Shedden [7] Jonas [8]	5.5	640	12,500
Alcomax 3 (Al, Ni, Co, Fe, Nb)	1947	Hadfield [9]	5.0	670	12,500
Alnico 5 (Al, Ni, Co, Fe, Cu) crystal orientation	1948	McCaig [10] Bemius [11] Ebeling [12] Swift Levick et al [13]	6.5	680	13,000
Alnico 8 (Al, Ni, Co, Fe, Cu, Ti) and Alnico 9	1956	Koch et al. [14]	4.5 9.2	1450 1500	8500 10600

Table 1 Chronology of discovery of Alnico permanent magnets.[22]

Alnico's 1 through 4 are isotropic. In contrast, Alnico 5 is anisotropic and its magnetic properties are characterized by a knee in the normal demagnetization curve. The variations in the unit properties of the subgrades are a direct result of subtle differences in chemistry but also of heat treat process techniques. In general, increased coercivity is obtained at the expense of reduced remanence. Alnico 6 are derivatives of Alnico 5. Alnico 6 have a finer grain structure because of the titanium addition and they are mechanically tougher. Titanium additions also increase coercivity but at the expense of reduced remanence. Alnico 8 were introduced into the market in the early 1960's. This material exhibits a lower remanent induction but has a coercive force approximately two and a half times of the last Alnico, and an energy product equal to Alnico 5 with an equiaxial crystal structure. In 1964, as a result of further work on changing the alloy composition to improve the coercive force without further reduction of the remanent induction, Alnico 9 was introduced into the American market. Introducing Alnico 8 and 9 a big improvement in magnetic properties was done. This can be seen in *Figure 6* where hysteresis magnetic curves of these materials are shown.

In contrast to Alnico 5 and Alnico 6, Alnico 8 and Alnico 9 require an isothermal heat treatment around 840°C in an external magnetic field to develop the magnetic properties. This plus the fact that Alnico 8 and Alnico 9 are inherently more brittle compared to Alnico 5 and Alnico 6, in general, limits the geometries of the castings to regular shapes such as blocks, cylinders, rings, etc. with straight through orientation.

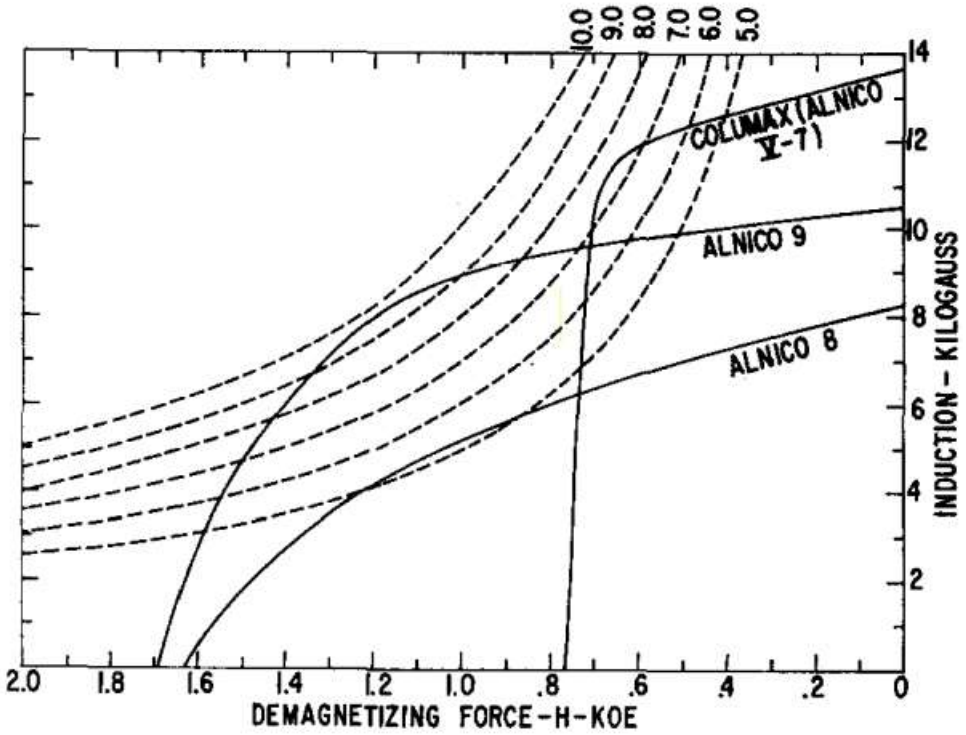

Figure 6 Difference in magnetization curves between different Alnico grades alloys

There are mainly two methods of producing Alnico alloys: by casting or by sintering powders. Different manufacturing methods result in different microstructures and thus in different material properties. Casting is the main method but in order to satisfy certain shape or other type of request, sintering is also an important method. Sintered Alnico's are manufactured through a powder metallurgy process. The magnetic properties of sintered Alnico's have been improving over recent years and the magnetic properties of present day sintered Alnico 2, 6 and 8 are as good as their respective counter parts in cast Alnico. However, sintered Alnico 5 magnetic properties are still somewhat inferior to those of cast Alnico 5. Directional grain is a singular property of cast Alnico 5-7 and Alnico 9 alloys and there are no sintered products with equivalent magnetic properties. Sintered products exhibit superior tensile and rupture strengths so also mechanical properties are influenced by the different methods of manufacturing the alloy.

1.2.3 Improvements

Alnico alloys have not changed greatly in their metallurgical concept over the years. Progress in developing better permanent magnets with Alnico materials was confined almost entirely to variations in chemistry. The advent of World War II delayed the commercial exploitation of this material and it was not until the late 1940's that significant work was started on further improvement of magnetic properties. It is significant to note that during this entire period very little emphasis was placed on controlling the crystalline structure of the Alnico castings, but it was known that pieces cut from casting surfaces that exhibited improved crystalline anisotropy also showed improved magnetic properties parallel to the crystal axis. During the latter 1940's, Bernius and Ebeling demonstrated that the magnetic properties of the Alnico 5 alloys could be considerably

enhanced for a complete casting if a high degree of crystalline anisotropy was introduced by special foundry techniques where a single flat wall of the casting mold contained a cold surface with high thermal conductivity and capacity. Columnar crystal growth from this chill plane could assure a high degree of crystalline anisotropy (the magnetic properties of Alnico 5 were improved using the high degree of crystalline anisotropy). The relative improvement in magnetics of Alnico 5 with columnar grain is shown in *Figure 7*. Curve *A* refers to random grain Alnico 5 and curves *B* and *C* refer to varying degrees of columnar grain. The prospect of obtaining better properties with this strategy led researchers to concentrate more effort on developing techniques which would assure castings with such a crystal structure directly from foundry procedures. The material produced by this method has been known in England as "Columax" and in the United States as "Columax" and ‘’Alnico V-7’’.[4.3]

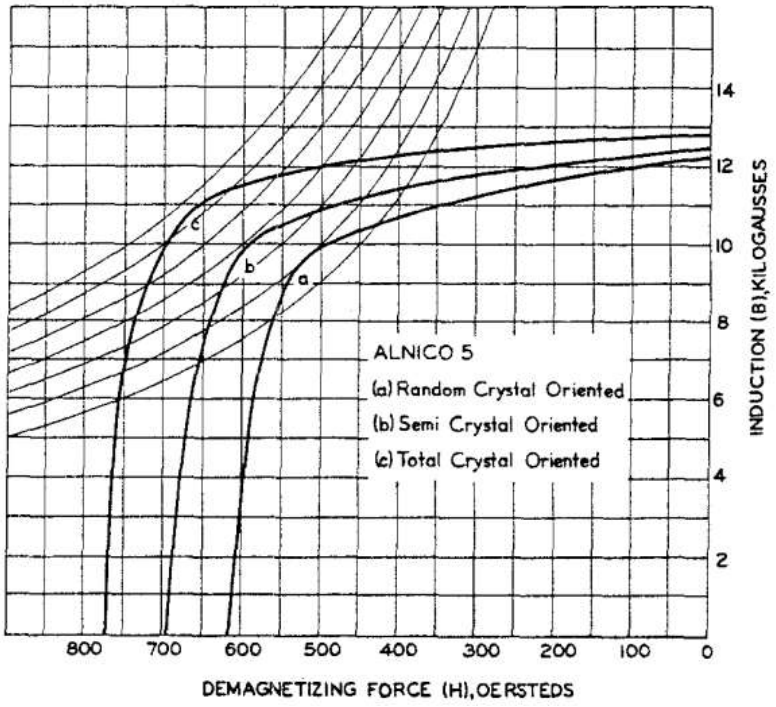

Figure 7 Effect of crystal orientation on magnetic characteristics of Alnico 5 [22]

In the early 1960's, Eberhart Steinort demonstrated that by a *secondary recrystallization method*, a monocrystalline mass could be converted from an existing polycrystalline aggregate of Alnico 5. However, with the introduction into the American market in the early 1960's of Alnico 8, alloys with much better magnetic properties, a new field was open. This material exhibits a lower remanent induction but has a coercive force approximately 2 times and an energy product equal to Alnico 5 with an equiaxial crystal structure. Furthermore, using the square factor theory, researchers noticed that the improvement of the energy density in Alnico 5 alloys was limited by its composition. Since they have not been able to develop an Alnico alloy that will exhibit a higher remanence, their attention has now turned in the direction of increasing coercive force, since it had been demonstrated by the introduction of the isothermally treated, high-cobalt, high-titanium materials known as Alnico 8, that the coercive force does not have any such sharp upper limit or indeed, if it does, it is far beyond the present technology. [23]

Since Alnico 8 has a high titanium content, which is necessary to enhance the coercive force of the material but, at the same time, introduces a very marked grain refining effect, it was originally quite difficult to foresee how columnar crystal growth could be achieved by the best possible techniques developed for the Alnico 5 family. Early experiments indicated that the Alnico 8 alloy didn't show any great amount of crystal growth because of some chemical elements, thus for some time there was considerable doubt in the Alnico industry that any practical results could be achieved.

In the 1962 it was discovered by several independent researchers that the addition of sulfur to Alnico 8, the columnar crystal growth problem was solved and, at the same time, did not seem to produce any deleterious effects upon the magnetic properties. Since that time, further work on changing the alloy composition slightly to improve the coercive force without further reduction of the remanent induction, resulted in the introduction into the American market in early 1964 of a material known as Alnico 9. Furthermore, the addition of approximately 0.45% of niobium further enhances grain growth and enlarges the grain cross section. This phenomenon is fully understood in the steel industry and exhibits the same general characteristics when used in Alnico 5 or other alloys. It also increases the coercive force and it is recommended for Alnico 9 production.

It has been discussed that with but two major exceptions, all significant improvement in magnetic properties of Alnico alloys have been achieved by special foundry techniques to promote crystal anisotropy, and not by alloy composition variations. The exceptions are found in the advent of the family of high-coercive-force alloys using increased amounts of cobalt and titanium known today as Alnico 8 and 9, and in secondary recrystallizing techniques on special forms of Alnico 5 to produce a single large crystal from a polycrystalline aggregate.

1.2.4 Advantages

The magnetic properties of Alnico's have long been overshadowed by the advent of rare earth permanent magnet materials. Despite this fact, Alnico's continue to find applications where one or more of the following criteria are important. The criteria are the followings:

- cost;
- excellent thermal stability and high Curie temperature (up to 550°C). Alnico magnets are a good choice for the application at high temperature (in electric engines, for istance) as the permanent magnets base on niobium need disprosium to be added in order to resista t high temperatures. This solution is too much expensive, nevermind the rare earth element crisis.[25];
- ease of magnetization in assembly of both virgin and non-virgin magnets. This last fact is a direct consequence of the low coercivity of Alnico permanent magnet materials. However, low coercivity also implies susceptibility to demagnetization effects either through mishandling or improper usage of the magnets in the magnetic circuits. Both these aspects should be considered while working and designing with these materials

In order to select a proper material, some other consideration on the Alnico alloys must be done. In a static design, for minimal volume of the magnet the load line of operation of the magnet should be at peak energy product. However, for stability purposes, it is preferable to operate the magnet above the knee. In a dynamic application, the designer should be aware that there could be a

significant loss of flux from saturation should the load line of operation shift well below the knee the second quadrant demagnetization curve. In any case, Alnico magnets lack in ductility and are inherently extremely brittle. They should not be designed for use as structural components. [22]

1.2.5 Heat treatments and spinodal decomposition

The anisotropy of most permanent magnets is of magnetocrystalline origin, meaning that hysteresis and coercivity rely on the atomic-scale interplay between spin-orbit coupling and crystal-field interaction. Alnico magnets are an exception, because their magnetic anisotropy and hysteresis originate almost entirely from magnetostatic dipole-dipole interactions so from a shape anisotropy[13]. The permanent magnetic properties of Alnico alloys are related to the shape anisotropy as well as to the M_s (magnetic saturation) difference between the different phases. A typical microstructure of the rod-like ferromagnetic α_1 phase embedded in the non-ferromagnetic matrix of α_2 phase is developed during the heat treatments. Phase diagram of the alloy is extremely important as it serves as a reference point for several parameters of the treatment.

A complete heat treatment is made up of three characteristic steps. First, the sample is homogenized at a temperature close to 1250°C in order to obtain a microstructure of a unique phase, as the phase diagram predicts. The second step is the thermomagnetic treatment. Usually, a magnetic field is applied with the purpose of developing the rods in a preferential direction, so to achieve the crystalline anisotropy. During this step spinodal decomposition occurs and magnetic properties arise. Finally, the third step is made up of different long-time tempering treatments at a lower temperature for the further improvement of the magnetic properties of the alloy.

During the three steps of the heat treatment several different changes in the microstructure occur. Furthermore, the shape of the microstructure is closely related with the final magnetic properties. For these reasons it's extremely important to fix the main parameters of the heat treatments in order to develop a nanostructure with a proper morphology and size that give to the alloy the best magnetic properties.

1.2.5.1 Solubilization

Solubilization is the first step of the heat treatment and it consists in heating the alloy to a temperature close to 1250°C, in vacuum, for around twenty minutes followed by fast cooling in water or in oil bath. The temperature and time parameters are chosen with the purpose to homogenize the microstructure. This is doable when the material is brought in the conditions where only one phase is predicted by the phase diagram. Considering that only a few phase diagrams are known for ternary or quaternary alloys, it's common to use in these cases a phase diagram for a quasi-binary alloy. A quasi-binary phase diagram is shown in the *Figure 8*.

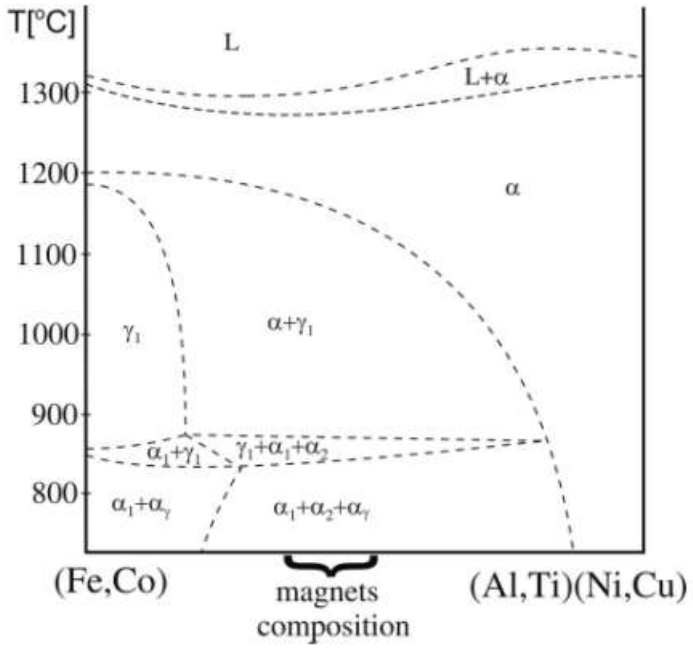

Figure 8 Phase diagram for Alnico magnets [16]

As it can be seen from the diagram, different phases can coexist at different conditions within the range of compositions corresponding to the permanent magnets. The different phases are:

- α_1 -a solid solution rich in Fe and Co. The lattice is a body centered cubic one.
- α_2- a solid solution rich in Al and Ni. The lattice is a body centered cubic one.
- γ_1- a disordered solid solution based on γ Fe with face centered cubic lattice.

The solid solution γ_1 appears at temperature between 900°C and 1100°C. Below these temperatures γ_1 transforms into a body centered cubic phase different from α_1 and α_2. Taking into account its origin, this phase is denoted α_γ.

During the whole standard heat treatment, the structure of α_1 and α_2 should be produced. The solubilization step of the heat treatment has the aim to homogenize the composition to the α phase. Then, the samples are quenched to the room temperature in order to freeze the microstructure as at the room temperature the kinetics of the process are suppressed. A fast cooling is important to avoid the γ_1 phase at high temperatures. If the cooling is carried out from temperatures too low, then an undesired microstructure made up of $\alpha_1 + \alpha_2 + \gamma_1$ will be produced (*Figure 9*). Rapid cooling, applied mainly to avoid the formation of γ_1 phase cannot in this case give the $\alpha_1 + \alpha_2$ microstructure, because the α_1 will have no time to precipitate in a sufficiently large volume[16].

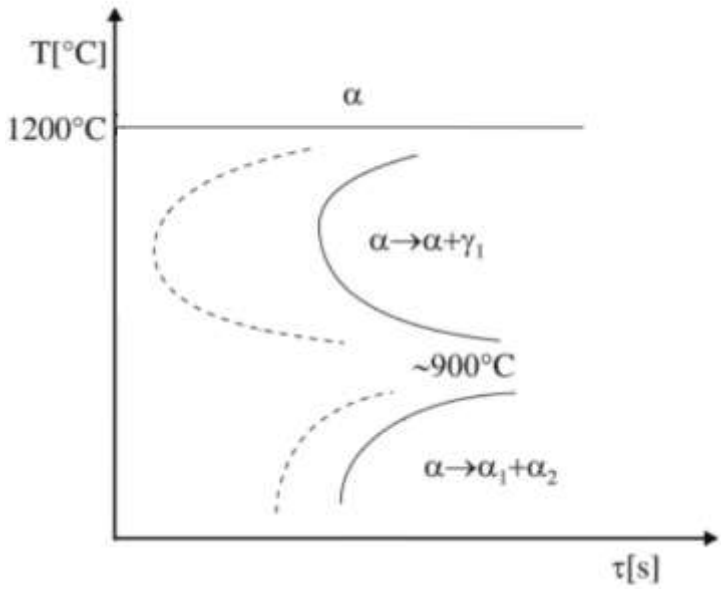

Figure 9 TTT diagram for Alnico alloy [16]

Alnicos have the best magnetic properties when their structure is composed of a mixture of $\alpha_1 + \alpha_2$ phases of the linear dimensions of a few nanometers. It's extremely important then to avoid the formation of the undesired phase γ_1 through a fast cooling. Nevertheless, considering that Alnico alloys are quite brittle materials, quenching can't be too fast otherwise microcracks will appear and the material characterization will be compromised. Thus, besides an appropriate temperature and time, a correct cooling rate must be identified as well.

1.2.5.2 Thermomagnetic annealing

The second step of the heat treatment on Alnico alloys consists in isothermal annealing in order to start the spinodal decomposition process. During this stage a magnetic field is applied with the aim to foster the rods development in one crystallographic direction. The temperature of thermo-magnetic treatment should be high enough to provide the required rate of diffusion in magnetic field, but also it should never take the alloy in the region of γ_1 phase stability. The product of the correct spinodal decomposition is a microstructure of Fe-Co rich magnetic rods (α_1 phase) which are embedded in non-magnetic Ni-Al rich matric (α_2 phase). This morphology is linked with the magnetic properties of the alloy through the magnetic anisotropy already mentioned. After the solubilization treatment the magnetic properties are poor while after the thermo-magnetic annealing the magnetic properties are developed. Thus, it is possible to trace the spinodal decomposition measuring the magnetic properties of the alloy.

Theoretical studies on magnetic aging of the spinodal decomposition alloy showed that in the spinodal decomposition process, the composition wavelength is determined by the interplay of chemical free energy, elastic energy, and magnetic energy. The elastic energy suppresses the reaction, while the magnetic energy suppresses the development of composition waves along the external field direction. The magnetic energy can have a serious effect on the process only when the

alloy is annealed just below the Curie temperature, where the change of magnetic energy is the largest[12].

Cahn predicted that in the early stage of the decomposition the composition waves with a certain specified wavenumber would be selectively amplified, leading to a modulated or periodic precipitate structure. The specified wavenumber β_m is given by

$$\beta_m^2 = -\frac{\left(\frac{\partial^2 f}{\partial c^2}\right)_0}{4K}, \tag{11}$$

where f is the free energy per unit volume of a homogeneous alloy of composition *c*, the subscript 0 indicates that the value of the second derivative is taken at $C=C_0$, and K is a gradient energy coefficient proposed by Cahn and Hilliard. According to their statistical mechanical derivation of the K for a regular solution on the assumption of nearest neighbor interaction,

$$K = \frac{N_v k T_c r_0^2}{3}, \tag{12}$$

where N_v is the number of atoms per unit volume, *k* is the Boltzmann constant, T_c is the critical temperature of the two-phase separation and r_0 is the interatomic distance. It should be noted that the *K* is always positive for the spinodal systems.

As the composition fluctuations are usually accompanied by a strain field, the elastic energy term should be included in f in *eq. 11*. The problem was theoretically considered by Cahn, who elucidated that the elastic term affects to suppress the spinodal decomposition in an interesting way. Particularly, for crystals with cubic symmetry, it was shown that an anisotropy in the elastic properties could be reflected in the decomposition processes. In most cubic alloys including Alnico, thus, the decomposition waves are found to develop selectively in the crystallographic directions, because the suppression effect is minimum in those directions. As the elastic term is taken into account, eq. (11) can be reformed into

$$\beta_m^2 = -\frac{\left(\frac{\partial^2 f_0}{\partial c^2}\right)_0 + 2\eta Y_{100}}{4K} \tag{13}$$

where f_0 is the Helmholtz free energy (or chemical free energy), η is the fractional change in lattice parameter per unit composition change, and Y_{100} is a specialized elastic constant in the direction, which is expressed as $(C_{11} + 2C_{12})(C_{11} - C_{12})/C_{11}$ by using the cubic elastic constants.

Moreover, considering the relation between β_m and the decomposition temperature, *eq. 13* can be written as

$$\beta_m^2 = \frac{N_v k}{4c_0(1-c_0)K} \cdot (T_s - T) \tag{14}$$

which shows how the wave number of the modulated structure depends on the decomposition temperature.

In a case where ferromagnetic materials are concerned, another extra term, the magnetic energy term must be added to the free energy. It has been found that the term plays an important role in the spinodal decomposition of some alloys such as Alnico. In the case of a cubic ferromagnetic crystal, as it was already noticed, the sinusoidal composition waves due to spinodal decomposition

take place exclusively along on of the three principal directions. Furthermore, if during the decomposition a magnetic field is applied along one of three principal directions, for instance along the [100] direction, then, according to Cahn, the [100] wave which is parallel to the field has the wavenumber described by

$$\beta_m^2 = -\frac{\left[\left(\frac{\partial^2 f_0}{\partial c^2}\right)_0 + 2\eta^2 Y_{100} + 4\pi\left(\frac{\partial M}{\partial c}\right)_0^2\right]}{4K} \quad (15)$$

where M is the magnetization, which is assumed a saturation magnetization if the magnetic field strength is sufficiently high.

It should be remarked, however, that the magnetic term might have a serious effect only when the alloy is annealed near its Curie temperature. Under the Weiss approximation for ferromagnetism the value of $\left(\frac{\partial M}{\partial c}\right)_0^2$ tends to infinity as the Curie temperature is approached. The right side of eq. 15, then, might become negative so to fully suppress the decomposition. It follows that the [100] wave parallel to the applied field should disappear. On the other hand, with respect to the other directions perpendicular to the field, such a magnetic term is not involved in the free energy. It follows that the [010] and [001] waves should develop whose wavenumber is given by eq. (13). Thus, the resultant decomposition structure will be expected as schematically shown in *Figure 10*. An observation of the cross-section perpendicular to the field would reveal a checkerboard-like pattern, which may be favorable to determine the wavelength involved. And an observation of the cross-section parallel to the field would reveal a striped pattern.

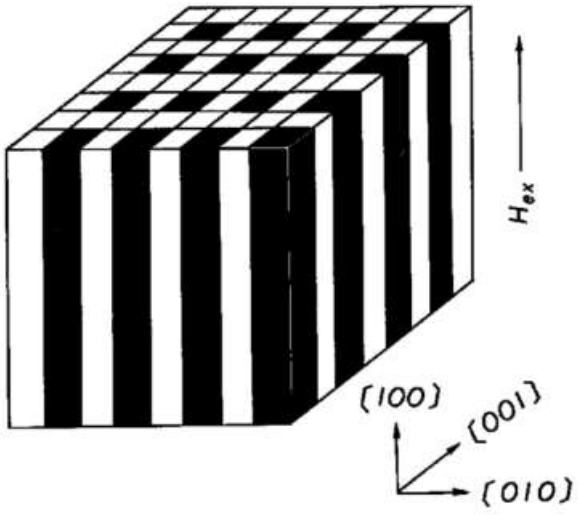

Figure 10 A schematic representation of the precipitate structure of ferromagnetic alloy resulting from spinodal decomposition in a magnet field [3.2]

The best magnetic properties are promoted by well aligned rods of the α_1 phase in a uniformly spaced mosaic pattern. For instance, the ideal morphology that brings optimum coercivity in higher grade alnico 8 and 9 series is a mosaic structure consisting of periodically arrayed 40 nanometers diameter α_1 phase embedded in a continuous α_2 matrix obtained by thermomagnetic annealing at

840°C [12]. It can be noticed from the last example that the morphology must respect certain specific shape parameters as Alnico's magnetic anisotropy originates almost entirely from magnetostatic dipole-dipole interactions. Thus, appropriate heat treatment parameters must be selected in order to tailor the right morphology. The annealing temperature and the annealing time must be within a range that leads to the requested configuration. Therefore, spinodal decomposition may occur without exhibiting a strong improvement the magnetic properties. As it can be noticed, measuring of the magnetic properties could not be the most appropriate method of tracking the spinodal decomposition. If a consistent improvement in the magnetic properties is not shown after the heat treatment, other direct investigation techniques must be used to observe the process.

1.2.5.3 Step-drawing annealing/low temperature tempering

The last step of the heat treatment consists in another isothermal annealing with lower temperatures and longer periods of time. This step aims to improve furthermore the coercivity of the material already developed. During the thermo-magnetic annealing step, the kinetics of the spinodal decomposition are rapid and the near optimum geometric spacing is quickly reached due to higher annealing temperature. The draw step is responsible for the finer microstructural and chemical tuning. It does not introduce dramatic microstructural changes of α_1 and α_2 phases, but other changes on the nano scale take place.

Several transformations occur during drawing, especially when copper-containing alloys are processed. Copper bridges, formed during the thermomagnetic treatment, undergo elements redistribution and morphology changes. This phenomenon is important as bridges with very high copper concentration and sharp boundaries in the final configuration may be one reason for the better magnetic properties after tempering because they contain less magnetic elements and increase the difference of saturation between bridges and the other two main phases. Other transformations may be a reason of the magnetic properties changes as well. In general, the drawing temperatures are too low to provide a rapid diffusion, nevertheless the elements are still able to diffuse in order to reach a more stable and closer to the equilibrium configuration. As a result, the element distribution changes between α_1 and α_2 phases and the interface becomes sharper. Also, as the two phases are furthermore separated, the distinction of the lattice parameters between α_1 and α_2 phases is expanded. This phenomenon can be seen on the XRD patterns as the peaks corresponding to the different parameters BCC structure of the phases are split[10, 11] so the process can be tracked.

In any case, considering the consistency of improvements and the costs required to develop them, the step drawing annealing is not always applied in the industry of the Alnico alloys.

2 CHAPTER 2

SAMPLE PREPARATION AND INVESTIGATION TECHNIQUES

Two different Alnico casted alloys are studied by the following experiments. The first set of the samples is the Alnico 5 alloy. The other two sets deal with Alnico 2 alloy and Alnico 5 alloy again. The several investigations on the material are illustrated in this and in the following chapters.

2.1 MATERIALS AND METHODS

A set of twenty-five samples of Alnico 5 and a set of twenty samples of Alnico 2 were given for the study. Initially all the samples were already magnetized. Thus, one of them for each set was selected to be the sample of reference and has been called Sample 25 for the Alnico 5 set and Sample REF for the Alnico 2 set. Composition tests were done on the specimens to obtain the exact content of elements in the alloys as the elements strongly influence the parameters of the heat treatments that will be applied on the samples. EDS analyses were done for this purpose. The results of the average compositions are showed by *Table* 2 and the *Table 3*.

Element	Weight %	Atomic %	Net Int.
AlK	9.45	18.28	90.78
NbL	0.70	0.40	4.97
FeK	46.01	43.00	345.88
CoK	22.58	19.99	143.25
NiK	13.00	11.56	70.63
CuK	8.25	6.78	36.00

Table 2: average composition of the set number one (Alnico 5 alloy) from EDS analysis

Element	Weight %	Atomic %	Net Int.
AlK	9.27	17.83	150.75
FeK	55.14	51.24	705.83
CoK	10.79	9.5	117.05
NiK	17.6	15.56	161.47
CuK	7.2	5.88	53.74

Table 3: average composition of the set number two (Alnico 2 alloy) from EDS analysis

The project concerns in the investigation of spinodal decomposition in Alnico alloys by applying heat treatments on the specimens and by their later characterization. The main interest is to develop magnetic properties in the Alnico alloys as this phenomenon is a direct consequence of the spinodal decomposition. Thus, the decomposition can be studied. Other investigation techniques are applied to the samples with the same purposes.

As the spinodal composition takes place at a nanometric level, it is not possible to observe it with OM and SEM microscopy. For this purpose, several techniques and strategies can be suggested and used. This is the case of the magnetic and the hardness tests. As it has already been discussed, magnetic properties are developed during the heat treatments as a consequence of the spinodal decomposition. Measuring them it is possible to foresee the grade of the spinodal decomposition in the alloy. Nevertheless, magnetic properties not always represent in a proper way the spinodal decomposition. Therefore, other strategies are required. The hardness measurements aim to investigate the mechanical properties of the processed alloy. The main interest of this part of the

experiment is to determine if consistent changes occurred in hardness and if a link between changes in this property and the spinodal decomposition process can be defined.

2.2 HEAT TREATMENTS

Alnico magnets are characterized by high degree of magnetization and high remanence but compared to other types of magnets, their coercivity is relatively low. Considering this fact, the aim of the experiment was also to investigate possible effect of heat treatment on the maximum increase of coercivity.

The complete heat treatment is made up of three steps. The first step is solubilization and it aims to homogenize the composition along the sample. The homogenizing temperature and time are selected taking into account the phase diagram of the alloy (*Figure11*). A heat treatment at 1250°C for one hour of time in air was performed. Afterwards, the samples were cooled in the water and oil bath. At the beginning, two different substances were experimented in order to choose the better one for the future treatments. Water cooling is considered better as it is faster, but it risks to compromise the investigation of the samples as the microcracks can arise because of the brittle nature of the material. On the other side, oil bath cooling is characterized by a lower cooling speed so microcracks should not appear but then some unwanted transformations could take place. After a quick observation, it was established that water quenching could be considered appropriated for the experiment.

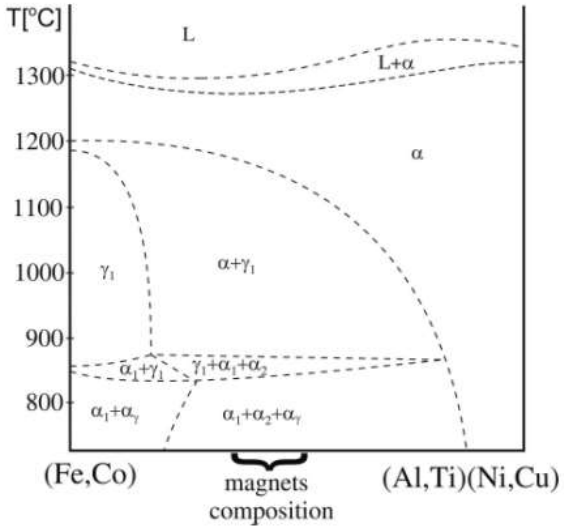

Figure 11: Alnico's phase diagram [2.7]

At the beginning, fourteen samples of the first set were homogenized following the already mentioned heat-treatment program. To keep them all together in the furnace a small box made up of carbon steel had been adopted. The following picture shows the homogenizing step of the heat treatment.

Figure 12: Homogenizing step of the heat treatment

The second step, the annealing step, is usually performed at a lower temperature than the homogenizing step. The annealing temperature must be high enough to allow the diffusion process to perform the spinodal phase separation but at the same time, it cannot be too high in order to avoid the unwanted transformations already discussed in the *Chapter 1*. The several temperature values for the first set of samples have been taken from a previous work on the samples made by Veres Janos at the BME University in 1984[30]. These values are summarized in the *Table 4.* For the second and the third sets of samples other considerations were done in order to choose the right parameters.

A1	Annealing at 840°C for 15 minutes
A2	Annealing at 840°C for 1 hour
A3	Annealing at 650°C for 6 hours
A4	Annealing at 650°C for 6 hours and then 550°C for 24 hours
A5	Annealing at 730°C for 10 minutes
A6	Annealing at 700°C for 10 minutes
A7	Annealing at 670°C for 10 minutes
A8	Annealing at 600°C for 10 minutes

Table 4 Temperature and time parameters for the annealing step from the Veres Janos work

The third step of the heat treatment is postponed to the end of the project when all investigations on the annealed samples are done. The drawing temperatures are chosen from the literature and

they are 650°C for the first step and 550°C for the second step. Drawing time was chosen in the same way and it is 6 hours for the first step and 24 for the second one.

A qualitative program of the whole heat treatment for all the sets of the samples is shown in the following figure:

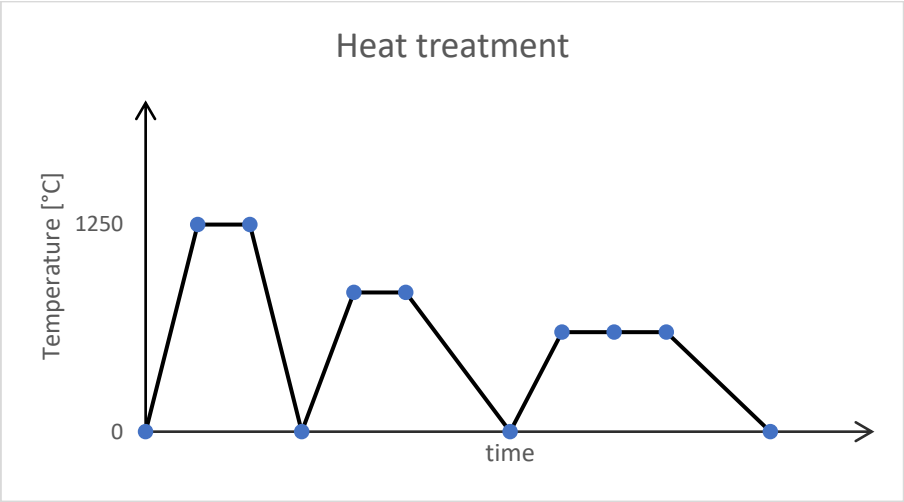

Figure 13 Complete qualitative heat-treatment program

2.3 SAMPLE PREPARATION

After the heat treatments the samples are oxidized because of the high temperatures and the oxidant atmosphere. Moreover, if the oil bath is used to cool them down, cleaning is necessary. Finally, in order to observe the microstructure or to do the hardness tests it is necessary to reduce the rugosity of the surface to the mirror-like surface. For this purpose, grinding and polishing are done on the samples.

For grinding, SiC abrasive papers with decreasing particle size (220, 320, 500, 800,1000, 1200, 2400 Grit) mesh were used and for polishing clothes discs with diamond paste (6 µm, 3µm and 1µm). These operations have to be carried out carefully, it must avoided to harden or to overheat the material. This is the reason why the operations are accompanied by the water flux. After these operations the sample are ready to be investigated.

2.4 HARDNESS TESTS

In general, hardness is defined as a measure of the resistance to localized plastic deformation induced by either mechanical indentation or abrasion. This property is measured considering how resistant is a solid material exposed to a compressive force applied on it. Moreover, it's a mechanical property which is quite simple to obtain.

Figure 14 Hardness tester

In this study, the hardness tests were done using the microhardness test machine produced by KB Prüftechnik, it is showed in the *Figure 13*. There are several different systems of measuring the hardness and it mostly depends on the shape of the indenter: the Vickers scale has been adopted in this study. The value of the hardness of the material in the Vickers scale is obtained by measuring the two diagonals of the rhomboidal imprint. The main parameters for the test are the applied test load and the dwell time of the test load. In this study, the load used is 30 kgf and the dwell time is 12 seconds. According to ISO 6507 for the Vickers hardness test, the value of the measuring is followed by HV30; the dwell time of the test load is in between 10 and 15 seconds so it is not reported in the measure. In the *Figure 13* it is possible to see the rhomboid imprint on the screen of the machine.

As it has already been mentioned, the hardness test had been done in order to study the eventual correlation between spinodal decomposition and the mechanical properties. The tests are done after the sample preparation. Any correlation will be analyzed in the final chapter.

2.5 MAGNETIC TESTS

2.5.1 Diamagnetism, paramagnetism and ferromagnetism.

A material placed in the magnetic field will undergo magnetic polarization of its molecules. Two different effects can manifest.

The first effect consists in the following behavior of the material. When *magnetic field* is applied, each molecule acquires an *induced magnetic dipole moment*, which gives rise to an *induced magnetic field* whose intensity depends on its nature and arrangement with respect to the inducing magnetic field (B_0): the induced magnetic dipole moment is always antiparallel to the inducing field. The inducing field and the induced field are summed up vectorially within the material and the effect

is a decrease in the magnetic field within the material ($B<B_0$). This effect is always present. In this case the overall phenomenon is called *diamagnetism*.

The second effect occurs in materials in which the molecules already possess a nonzero magnetic dipole moment; the inducing field B_0 exercises a mechanical moment on the molecules tending to align the magnetic dipole moment, and thus the induced field associated with it, with the inducing field. This effect overlaps the previous one and is generally stronger. In this case, the dipole moment is in concordance with B_0 and therefore the magnetic field strength in the material increases ($B_0>B$). In this case two possible phenomenon can arise. *Paramagnetism* takes place if, once the inducing field is taken off, the magnetic induced field of the material is zero again as the alignment of the dipoles is destroyed by the thermal agitation motion. Otherwise, if the inducing magnetic field is removed, there is a residual magnetic field in the material as the interaction between dipoles is too strong to be removed by the thermal agitation motion. This phenomenon is called *ferromagnetism*. To be noticed that every material has a transition temperature from the ferromagnetic state to the paramagnetic state if the thermal agitation motion grows with higher temperatures. This temperature is called Curie Temperature.

2.5.2 Magnetization and the main correlations

A material is made up of elementary magnetic dipoles that are normally randomly oriented in the space providing an average zero dipole moment. The material becomes magnetized if the average dipole moment is no longer zero.

The magnetization of a material is defined as its overall dipole moment per unit volume. Once defined $\overrightarrow{\mathrm{m}_i}$, the magnetic dipole moment for each elementary dipole, it's possible to express the magnetization of the material as

$$\overrightarrow{m_{TOT}} = \frac{\sum_i \overrightarrow{\mathrm{m}_i}}{V}. \tag{16}$$

In the magnetization induced by orientation, dominating in paramagnetism and ferromagnetism, the number of dipoles oriented in the direction of the external magnetic field B is an increasing fraction with the increasing magnetic field strength. A certain number of dipoles remain randomly oriented because of collisions between elementary components due to thermal agitation, so the number of aligned dipoles decreases as the temperature T of the material increases. Also, at constant temperature, the fraction of aligned dipoles can only increase as long as all dipoles are aligned, so there is a maximum of magnetization beyond which the magnetic field strength increases without causing any effect. The *equation 17* is the Curie law and takes into account the correlation between the magnetization and the temperatures and it fixes a certain limit to the maximum magnetization.

$$m = C\frac{B}{T}. \tag{17}$$

The total magnetic field is given by the *equation 18*

$$\vec{B} = \vec{B}_0 + \mu_0 \overrightarrow{m}, \tag{18}$$

where $\mu_0\vec{m}$ is the contribution given by magnetization to the electric field within the material, that is, a magnetization field $\vec{B}_m$.

Defining the magnetizing field $\vec{H}$ as

$$\vec{H} = \frac{\vec{B_0}}{\mu_0}, \tag{19}$$

other important correlation is derived between the magnetic field (B), magnetizing field (H) and the magnetization (m):

$$\vec{B} = \mu_0 \cdot (\vec{H} + \vec{m}) . \tag{20}$$

The introduction of $\vec{H}$ is useful in order to simplify the equations as for every material it is possible to establish an experimental relationship between $\vec{H}$ and $\vec{m}$ expressed as

$$\vec{m} = x_m \cdot \vec{H} \tag{21}$$

where x_m is magnetic susceptibility of the substance. The magnetic susceptibility is a criterion to characterize the substances in the following way:

- x_m< 0, constant and temperature-independent for the diamagnetic substances,
- x_m> 0, temperature-dependent, in a weak way for paramagnetic substances and strongly for the ferromagnetic substances.

From these equations it is possible to obtain the final magnetic law used in the magnetic tests of this study:

$$\vec{B} = \mu_0 \cdot \left(\vec{H} + \vec{m}\right) = \mu_0 \cdot \left(\vec{H} + x_m \cdot \vec{H}\right) = \mu_0 \cdot (1 + x_m) \cdot \vec{H} = \mu_0 \cdot \mu_r \cdot \vec{H} = \mu \cdot \vec{H} \tag{22}$$

where $\mu = \mu_0 \cdot (1 + x_m)$ is magnetic permeability of the matter and $\mu_r = \frac{\mu}{\mu_0} = (1 + x_m)$ is the magnetic permeability of the matter with respect to the vacuum. From the experimental works some results are derived:

- $\mu_r < 1$ for diamagnetism,
- $\mu_r > 1$ for paramagnetism,
- $\mu_r \gg 1$ for ferromagnetism.

To be noticed that for the diamagnetic and paramagnetic materials the relationship between the magnetic field $\vec{B}$ and the magnetizing field $\vec{H}$ is almost constant while for the ferromagnetic materials it is not constant, and it depends also on the magnetizing history of the samples.

2.5.3 Magnetic hysteresis and magnetic domains

It is observed that the magnetic dipole moment of the material is not due to the contribution of elementary dipoles diffusely and randomly distributed within it, but of large areas, of the order of $(10^{-3} \div 10)$ mm^2 in extension, called *Weiss domains*, showed in the *Figure 14* , in which all magnetic dipoles have the same orientation. A magnetic domain is sharply separated from adjacent domains

by very thin zones, of the order 10^{-7} m thick, called *Bloch walls*, in which the direction of the magnetic dipole moment varies continuously from one domain to another.

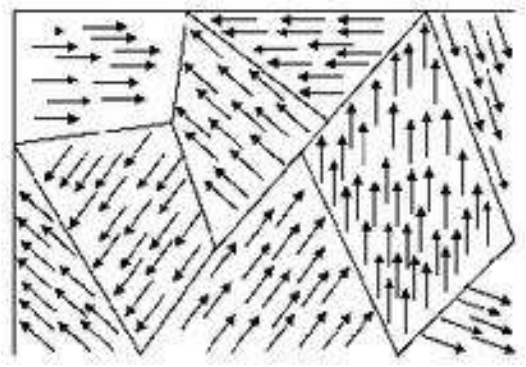

Figure 15 Weiss domains

In ferromagnetic materials, thermal agitation fails to destroy dipole alignment in microscopic domains, but the material may not manifest macroscopic magnetization because the various domains are randomly oriented. By applying an external magnetic field, the domains orient in the direction of the field, but the process does not occur continuously; rather, domains with magnetic dipole moment at a small angle with B expand, englobing adjacent domains. Thus, whole domains change direction in a process called the *Barkhausen effect*: the more the magnetic field increases in intensity, the more domains orient, until saturation[1].

Let now consider a ferromagnetic material. If this material is magnetized by increasing the strength of the magnetic field in which it is immersed and bringing it to its maximum magnetization from zero magnetization and if subsequently the magnetic field is brought back to zero by gradually reducing its intensity, then it is observed that a residual magnetization of the material remains and it is cancelled only by applying a magnetic field of opposite sign to that of first magnetization, called a *coercive field*. By continuing to increase the magnetic field strength, the material can be brought to maximum inverse magnetization, and again, by canceling the magnetizing field, residual magnetization remains. By repeating these operations, the material always follows the same symmetric curve, which is called the *hysteresis cycle*. The hysteresis loop is normally represented as a graph of the magnetic field (B) as a function of the magnetic intensity field in the material (H). A representation of the hysteresis cycle is showed in the *Figure 15*.

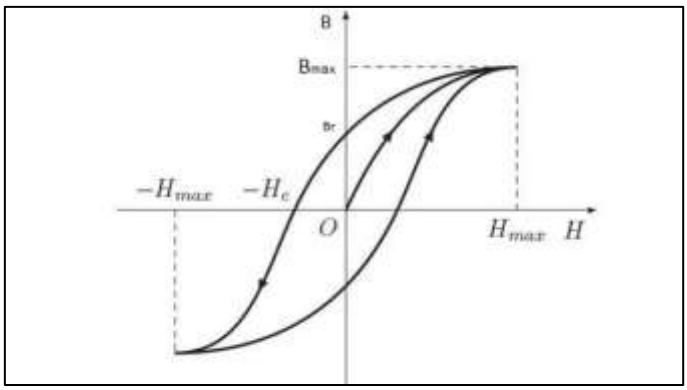

Figure 16 Generic hesterysis cycle

The hysteresis loop shape is used to classify ferromagnetic materials into soft and hard materials. Soft materials have a tight hysteresis cycle, low residual field, low coercive field and they are easily demagnetized. Hard materials have a wide hysteresis cycle, high residual field and high coercive field and they are difficult to demagnetize. Soft materials, for instance iron, are used to produce electromagnets, generators, motors and transformers; hard materials, for instance some steels, are used to produce permanent magnets. Demagnetization is achieved by rapidly reversing the magnetic field, for example by reversing the current that generates it, after bringing the material to maximum magnetization while slowly reducing its intensity. Basically, the material is forced to go through increasingly narrow hysteresis cycles until when a practically zero area of the last loop is obtained.

2.5.4 Stäblein Steinitz test

In this work, Stablein Steinitz Dc magnetometer had been used for the measuring of the magnetic properties. It is a close circuit magnetic equipment designed to reach high coercivity and magnetization field with samples which have small length/transverse dimensions ratio. It consists of a two U-shaped soft iron yokes, placed opposite one another and with an air gap between each of the two pairs of transverse limbs. If the measuring air gap does not contain sample the arrangement is magnetically symmetrical consequently there is no flux through the middle bridge. If the sample is fixed into the measuring air gap the symmetry is broken therefore some part of the magnetic flux closes through the middle bridge. The magnetic field which is measured by a Hall-sensor in the middle bridge is directly proportional to the magnetization of the sample. The Stablein-Steinitz DC magnetometer is capable to excite the bulk steel samples into magnetic saturation which makes it one of the most precise ways of the measurement. The maximum excitation field strength was about 2700 A/cm. This set-up is not portable, it is only for laboratory use because of its extensive size. The instrument is shown in the figure below.

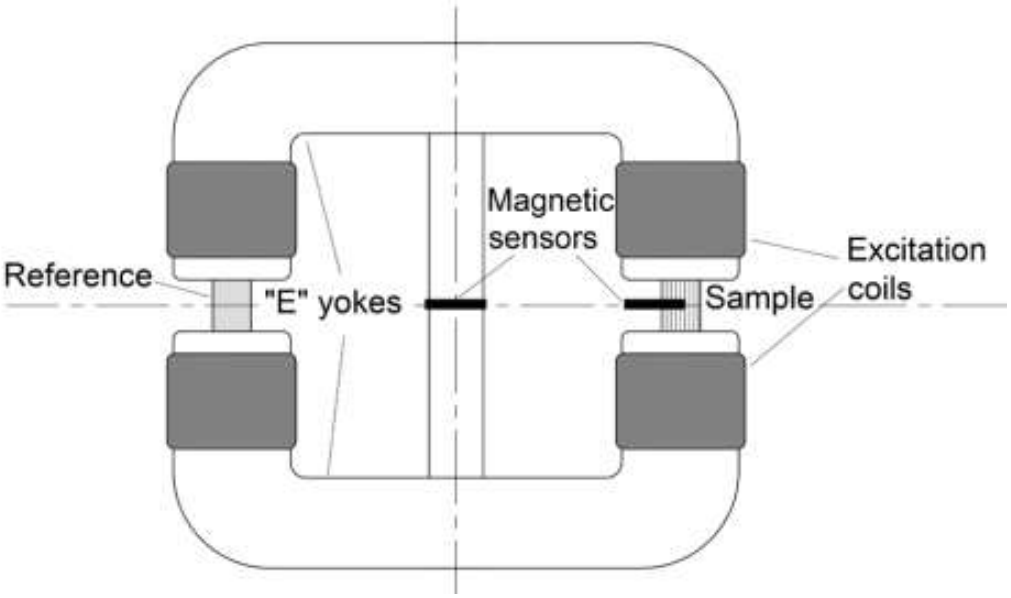

Figure 17: Construction of Stablein Steinitz DC magnetometer [26]

2.6 OPTICAL MICROSCOPY

2.6.1 Optical microscopes

Optical microscopes are usually used for the following microstructural analyses: grain shape and size, phase distribution, presence of defects. They are generally equipped with an acquisition system (camera) and image analysis software. It uses the light reflected by the metal surface, which appears different in color and intensity because of the different corrosion by chemical reagents in the various areas.

The working principle of the optical microscope is the following. The surface to be observed is placed on a small table, adjustable using two micrometric screws, at the center of which there is a hole for the transit of the light. The light coming from a source suitably collected by baffles and condensers, is directed through a mirror to the specimen surface after passing through the lens. The reflected light is concentrated back into the objective; the light signal is deflected by the prism towards the ocular lens, which allows a magnified view of the preparation. The signal can finally be deflected by a mirror and sent to a photographic screen or camera. This process is shown in the *Figure 18*.

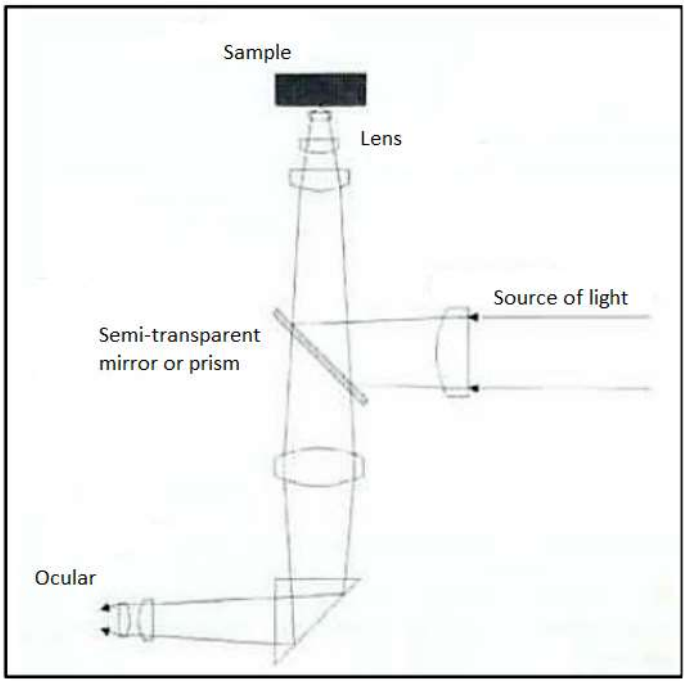

Figure 18 The working principle of the optical microscope

The microscope Olympus PMG3 was used for the microstructure analysis of the heat-treated samples and it is characterized by Olympus DP70 camera and Olympus DP controller software. The microscope is shown in the figure below.

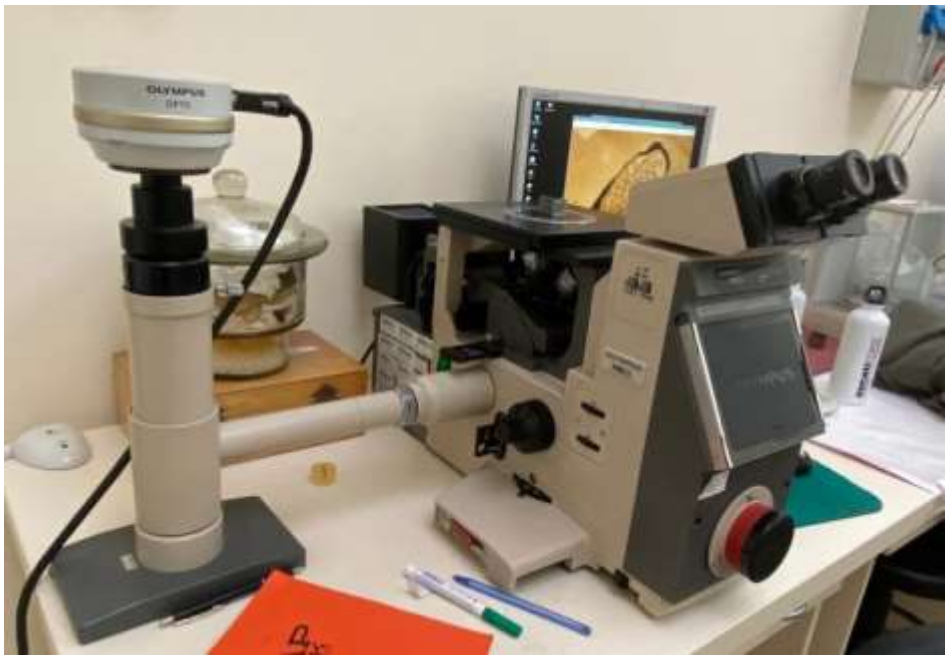

Figure 19 Optical microscope Olympus PMG3

2.6.2 Metallographic preparation

An appropriate metallographic preparation is essential to observe the microstructure of the sample with the microscope. Several steps of the preparation must be done for this purpose. In this study, the samples were initially grinded and polished and then they were etched with a chemical solution called etching agent. Grinding operation consists in several passages on the abrasive papers of controlled grit size (80-120-320-600-1200-2400 Grit). Rotating disks of abrasive paper are used to grind and a liquid (generally water) flows to remove heat and residues. Afterwards, polishing operation consists in several passages on the fabric discs sprinkled with abrasive aqueous solutions (based on alumina/diamond/SiC paste based). Etching agent is the chemical solution which better evidence the microstructure of the specimen through the selective corrosion. In this study Nital10 and Marble's reagent were chosen from the ASM Handbook and have been used in order to obtain the better-quality images from the observations.

Grit number	Size of the particles [µm]
80	212-180
120	150-125
320	46
600	26
1200	15
2400	12
4000	8

Table 5 Grinding: abrsasive papers

Nital 10 etching agent was already present in the BME University laboratory while Marble's reagent had to be prepared. The preparation involves 10 grams of copper sulphate ($CuSO_4$), 50 milliliters of hydrochloric acid (HCl) and 50 milliliters of hydrogen peroxide. The reagents must be put together and mixed until a homogeneous solution is formed. For this purpose, a magnetic agitator is used. Other tools for the chemical solution preparation used are spatula and graduated cylinder. The preparation can be seen in the figures below.

Figure 20 on the left: Magnetic agitator and the mixing step

Figure 21 on the right: Several reagents for the etching agent preparation

After having prepared the samples with grinding and polishing, have cleaned the samples with water and soup and have prepared the etching agents the etching operations can take place. Etching is a delicate operation that requires careful handling. Furthermore, several tools are involved and the steps of the process must be done quickly. The several steps to be followed involves the etching in the Marble's or Nital 10 etching agents, the immediate cleaning in ethanol and the submersion of the sample in the ultrasonic machine. The last step is quite important for the Alnico cast alloys as they show several microcracks which can act as traps for the etching agent, so the water cleaning is not enough to take away the reagent and the reaction goes one even after the etching step is supposed to be finished. All the operations are done under the chemical fume hood. The laboratory rules must be respected as the substances used are dangerous for the health of the human being. The tools and the worktable are shown in the figures below.

Figure 22 on the left: The substances used in the etching step

Figure 23 The worktable for the etching operations

2.6.3 Microscope observations

After having etched the specimens and cleaned them the observations with the microscope can be done. The use of the microscope involves the various possibilities of magnification and focusing. Every observation, a picture from the software has to be taken and saved on the computer. It is extremely important to check the scale on the picture. The scale is provided by the total magnification which is usually given by the objective multiplied for the intermediate optics multiplied for eyepiece. With the BME optical microscope it is enough to multiply the objective value for the eyepiece value which is always 10.

2.7 ELECTRON MICROSCOPY AND EDS ANALYSIS

2.7.1 Electron-matter interactions

2.7.1.1 Elastic interactions

Elastic interactions between the electron and matter consist of energy-loss-free collisions of the incident electron with the electric field of the nuclei of the atoms of which the sample consists of. The interaction gives rise to changes in path of the primary electron at angles higher or lower than 90°. In the first case, the bounced electrons are called backscattered electrons. If they are close to the surface, then they can re-emerge from the sample. In the second case, the phenomenon is known as the multiple scattering. In this case the electrons, although having deviated from their original trajectories, still move within the material, resulting in the possibility of interacting with other atomic structures through further elastic or inelastic collisions. The cross section of impact, Q, quantifies the probability that elastic diffusion will occur, and is proportional to Z/E_0, where Z is atomic number of the material and E_0 is the energy of the incident electron. For the same incident energy, materials with high Z offer higher probability of elastic events, efficiently giving rise to backscattered electrons close to the surface of the sample from which they re-emerge. In addition, as electrons lose energy proceeding along the diffusion path, the probability of elastic events increases with Z^2/E_m^2, where E_m is the energy at a generic point of the diffusion path that tends to zero as the path traveled increases. For high Z the possible diffusion paths results in an inverted cup.

For small Z, the primary electrons penetrate, on the contrary, deeper as there are fewer surface collisions, resulting in broad and protracted trajectories toward the interior of the material and the consequence is that the volume of interaction in this case is similar to a pear.

2.7.1.2 Inelastic interactions

Inelastic interactions between the electron and the sample consist of energy-loss collisions of the primary electrons with the nuclei of atoms or the bound electrons of atoms. The loss of energy as the path *s* within the material increases is described by Bathe's equation: $-dE/ds = \rho S$, where *E* is the average energy of the primary electron at a generic point in the diffusion path *s*, *ρ* is the density of the material and *S* is the braking power of the material. *S* is related to the average ionization energy *J*, which is the average energy lost by the primary electron in a single inelastic interaction, and, since J is greater the higher the atomic number Z, in materials with high Z the average length of the total diffusion path is shorter than in materials with low Z. As a result, the size of the interaction volume depends on the atomic number: the higher Z is, the smaller the volume of interaction at the same incident energy E_0 of the electron beam. It is important to emphasize the fact that the interaction volume depends only on the energy of the incident electrons E_0 and the properties of the sample Z, and not on the size of the incident beam, since the interaction volume has dimensions of the order greater than one µm, while the diameter of the incident beam is usually of the order of a few tens of nm.

2.7.1.3 Backscattered electrons

Let *η* be the backscattering coefficient defined as the fraction of backscattered electrons relative to the number of incident electrons. Since the cross-section Q for elastic interactions is proportional to Z^2/E_0^2 it turns out that η grows as Z increases for constant incident beam energy E_0, while it decreases as E_0 increases for constant Z and manages to penetrate deeper making their re-emergence from the surface (backscattering) more improbable. Backscattered electrons have energies close to or equal to that of the incident E_0 electrons, so they have sufficient energies to re-emerge from the deepest layers of the interaction volume, about a few hundred nm deep from the sample surface. The broadening of the incident electron beam by scattering of the primary electrons within the material results in the source region being broader than the electron beam's area of incidence on the surface and, therefore, the spatial resolution associated with that signal is greater than the size of the incident beam. The backscattered electrons have a variable energy with an energy distribution having the maximum E_u less than the incident beam energy E_0, since an appreciable energy loss occurs as a result of multiple scatterings: this maximum, however, increases and approaches the energy E_0 for higher and higher Z. The fact that η depends on Z and that the energy distribution of the backscattered electrons also depends on Z means that the backscattered electrons provide information about the average composition of the sample, what is called Z contrast (compositional contrast).

The backscattered electron detector is a solid-state proportional detector, whereby an electron hitting it of energy E produces an electrical output signal that is proportional to the energy E. A material with a high Z number not only gives rise to a larger number of backscattered electrons but these electrons also have a higher average energy, closer to that of the incident beam. The signal from the proportional backscatter detector is, therefore, more intense from a material with high Z atomic number. Elastically scattered electrons have a nonuniform scattering angular distribution

f(γ) defined as the angle of incidence of the primary beam ϕ and the angle of scattering γ we have that the scattering probability is maximum for γ 180° if the angle of incidence of the primary beam ϕ is 90°. This is why solid-state backscatter detectors are annular and coaxial with the primary beam in conventional SEMs and are placed near and below the objective lens where the distribution of backscattered electrons is maximum. For angles of incidence less than 90°, there is an increase in η and the average EM energy of the emerging electrons that increasingly approximates that of the incident beam E_0. In addition, the interaction region is reduced because scattering in the material is limited to thin surface layers of the material before reemergence, so that for reduced angles of incidence, the spatial resolution increases significantly (at the expense of Z resolution) C ambles also the angular distribution of the backscattered electrons, so that γ tends to 90° (grazing emergence), so that different detector positioning is required if one you want to use such a signal In this case we speak of Low Energy loss Electron Microscopy. On a flat sample of the type used in metallographic investigations, such that there is no contrast topography, it is possible to distinguish consecutive elements in the periodic table with differences of 2 in Z. The resolution of backscattered electron images is essentially related to the emission volume. Because of the greater penetrating power of high energy electrons, the resolution is much greater than the corresponding for secondary electrons: true resolution not less than 0.3 microns. The depth of the analysis is in the range from 0.1 to 1 μm. The degradation in the resolution occurs due to the need to operate at currents relatively high to get a signal of sufficient intensity.

2.7.1.4 Secondary electrons

The primary electrons, diffusing within the material, interact with the more external electrons of the atoms and supply them sufficient energy to make them free. The kinetic energy of such electrons, called secondary electrons, is given by a continuous distribution of values generally smaller than 50 eV and with peak values of a few eV units, which depend on the nature of the material. Because of their low energy, only the secondary electrons close to the surface (5 to 50 nm) are in a condition to emerge from the material by winning the extraction work of the material. The production of secondary electrons is independent on the atomic number Z of the material: defining *δ* as the coefficient of the secondary electrons emission, that is the fraction of secondary electrons relative to the number of incident electrons, we have that δ fluctuates around the value 0.1 for each Z and for incident beam energies E_0 typical of a conventional SEM (20 to 30 keV). δ depends, however, on E_0 since it increases as E_0 decreases and exceeds unity for values of E_0 close to 1 keV. Since δ is independent of Z and the secondary electrons come exclusively from a thin surface layer of the sample, the secondary electrons can provide exclusively information related to the morphology of the surface. The backscattered electrons have sufficient energy to generate secondary electrons, but the ratio between the secondary electrons produced by the primary electrons and those produced by the backscattered electrons is, however, equal to 1/5 such that only the surface portion related to the impact zone of the incident beam identifies the source region of the secondary electrons. The spatial resolution relative to the secondary electrons is, therefore, determined by the size of the incident electron beam focused on the surface and is certainly better than the resolution from backscattered electrons. The conventional detector for secondary electrons (Everhart-Thornley type), consists of a scintillator in front of which is a grating placed at variable potential with respect to the grounded sample. The secondary electrons are accelerated by this potential difference, and those that reach and pass the grid are further accelerated by an additional 10 kV potential difference between the grid and the scintillator, which gives the

secondary electrons sufficient energy to penetrate the layer of a few nm of aluminum with which the entrance to the scintillator is covered. The scintillator transforms the flow of electrons into photons that through a light guide by total reflection are directed to a photocathode placed at the input of a photomultiplier, at the output of which an electrical signal is produced and modulated into a television signal. The special positioning of the detector of the secondaries, placed lateral to the surface of the sample, gives the images from secondary electrons the three-dimensional appearance that is characteristic of this type of imaging the regions placed in favor of the detector are bright and well defined, while the unfavorably placed regions appear dark and poorly contrasted. It is remarkable the analogy with optical microscope image because the variation of the emission secondary electrons at different locations on the sample is related to its external morphology and the angle that the surface forms with the incident beam. They give the maximum resolution that depends on the wavelength of the radiation used, the minimum beam diameter, (electron optics), the fact that the secondary electrons come from an extended area-about 50 angstroms-around the point of impact of the primary electrons. The actual resolution is not less than 20 nanometers. The magnification (ratio of the size between the image final produced and the field explored by the electron beam on the sample) is from 10 to 200'000 times. The depth of the analysis is between 1 and 10 nm.

2.7.1.5 X rays

An electron, passing in the vicinity of an atomic nucleus, results in being deflected by the electric field shield of the nucleus (inelastic collision) producing X-rays with wavelengths which variability depends on the magnitude of the deflection and the loss of energy by the primary electron, thus producing a continuous X-ray spectrum ranging from E_0, the energy of the incident electron, to zero. The intensity of X-rays should be expressed as a function of wavelength. The intensity of X-rays goes from 0 for $\lambda=\lambda_0$ (wavelength corresponding to E_0) to increasing values for $\lambda>\lambda_0$. The rapid decrease in intensity for low energies is due to the absorption of low energy photons by the interaction volume. The continuous spectrum has no particular interest, since it does not contain significant information related to the analyzed specimen.

The primary electron can also interact with the atomic structure by ionizing it, if it has sufficient energy if an electron of the inner orbitals (K, L, M . . .) of energy E_1 and generating a vacant orbital. The excited structure relaxes through the transition of an electron from an orbital more external (of energy $E_2 < E_1$), which generates the emission of an X-photon of characteristic energy, the value of which is given by the relation: $E_{photon} = E_1 - E_2$ The remaining unoccupied orbital is filled by successive transitions electrons that produce photons with wavelengths close to the visible and of no analytical interest. The characteristic photons produced by such electronic transitions give rise to an X-ray spectrum or lines characteristic of each element and can be used for analytical purposes. An X-ray spectrum is presented as the sum of the continuous spectrum and characteristic lines.

Chemical analysis (microanalysis) in the scanning electron microscope (SEM) is accomplished by measuring the energy and intensity distribution of the X-rays generated by the electron beam on the sample using an energy dispersive spectrometry (EDS) detector. The analysis relative to an area or point of interest on the surface of the sample (microanalysis). Given that the portion of space excited by the electron beam, which produces the X-spectrum, is a few microns around the spot, the SEM&EDS is a powerful mean of investigating chemically inhomogeneous solids at the microscopic scale. The maximum resolution is of 1 µm and depth of analysis between 1 and 10 µm.

2.7.2 Scanning Electron Microscope

The Scanning Electron Microscope (SEM) exploits the generation of a high-energy electron beam in the vacuum. The beam is focused by a lens system and deflected to scan an area of the sample. The beam-sample interaction generates various signals that are acquired by appropriate detectors and then processed to form a 3-D gray-level image. The scheme of the function of scanning electron microscope is shown in *Figure 23*.

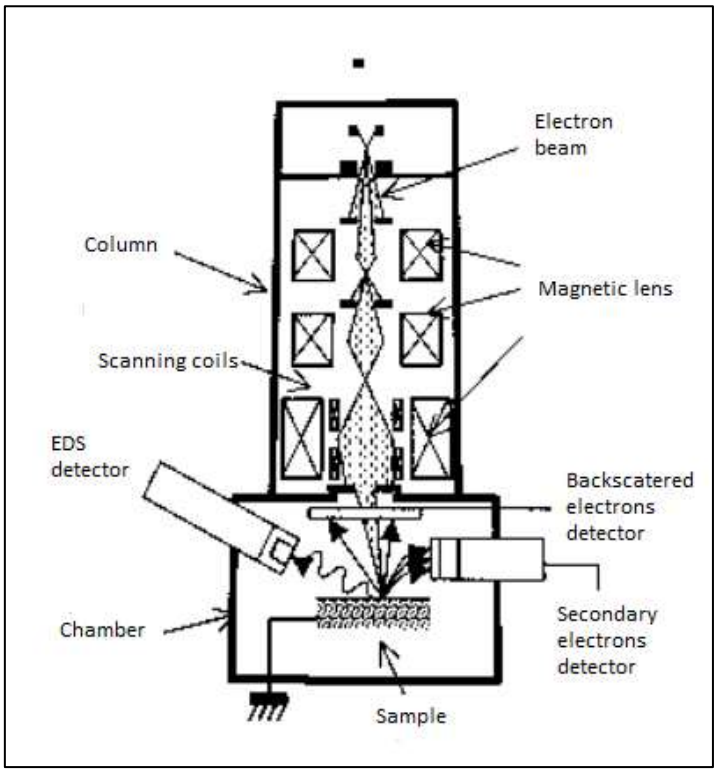

Figure 24 Scheme of Scanning Electron Microscope

By using its detectors several information can be obtained:

- Morphology of the sample surface,
- Chemical and physical composition,
- Electrical defects,
- Surface contamination,
- Measurement of surface potentials.

The function of a SEM is the following. A beam of electrons with kinetic energies between 1 and 30keV, called primary electrons, is generated by an electron gun (cathode) located at the top of the column. The beam is attracted in the direction of the anode, it is condensed by collimating lens and it is focused through objective lenses onto the massive sample, one of the sufficient thickness to not to be crossed completely by the incident electrons. The electron beam strikes the sample, producing, x-rays, auger electrons, absorbed electrons, secondary and backscattered electrons. The set of possible paths of electrons in the medium goes to define the *volume of interaction* which at the same energy is inversely proportional to Z and goes to define the spatial resolution. These electrons are collected by a detector for secondary electrons and one for electrons backscattered,

converted into electrical signals and amplified. These are converted into pixels and processed by a system equipped with a computer. The X-rays are collected by a Si(Li) detector.

Information about morphology is obtained by analyzing the secondary while informations about composition of the sample are obtained by analyzing the X rays and the back-scattered electrons.

The combination of high magnification (up to 100000 times), high resolution (up to 2 nanometers), wide depth of focus, and easy preparation and observation of the sample makes SEM one of the most reliable and easy-to-use instruments for the study and analysis of the specimens.

2.7.3 EDS analysis

EDS analysis is used to obtain the composition of the sample. The working principle of the EDS technique is based on the ability of the solid-state Si(Li) detector to discriminate the incident X photons of different energies. The Si(Li) solid-state detector consists of a monocrystal Si with a surface area of around 30 mm^2 and thickness of 3 mm in which Li has been diffused to enhance its resistivity and restore Si to the condition of an intrinsic semiconductor. A potential difference is applied to the detector which, given the intrinsic semiconductor properties, induces no current. In case the Si(Li) is hit by an X-photon, electron-lacuna pairs are generated in its interior where these signals are collected at the electrodes resulting in an electrical pulse. The detector is proportional: each X photon energy corresponds to a number Na of gap-electron pairs equal to Ex/e, where e is the energy for the formation of a single electron-lacuna pair equal to 3.8 eV in Si. The system has no internal gain, and a field effect transistor (FET), also called a preamplifier, provides the necessary gain for the FET signal, which will later be modulated by the electronics. The entire Si(Li) and FET preamplifier system, is kept at liquid nitrogen temperature to reduce the electronic background noise. Since the surface of the detector at liquid nitrogen temperature would act as a trap for residual particles in the SEM chamber, the system is separated from the chamber by thin polymer windows supported by Al gratings that allow characteristic photons to pass through. The miniaturized detector can be placed extremely close to the sample surface from which the X photons originate so the solid angle of collection is extremely high, ~10-2 rad, compared with the WDS system. The signal intensity of the detected X-rays is linearly proportional to the solid collecting angle, and in addition, there are no reflection systems or other interposed between the X generation region and the detector, so that the efficiency of the EDS system is significantly higher than the WDS system: this results in a lower need than the WDS technique to resort to high electron beam currents. In addition, this efficiency results in spectra with characteristic peaks with high peak P values (but low values of P/B ratios). The acquisition of the X-rays in the EDS system occurs simultaneously, and a multichannel analyzer system is used to count the X photons detected in each energy channel ΔE equal to 20 eV or 10 eV, into which the spectrum acquired, generally between 0 and 20 keV or 0 and 10 keV.

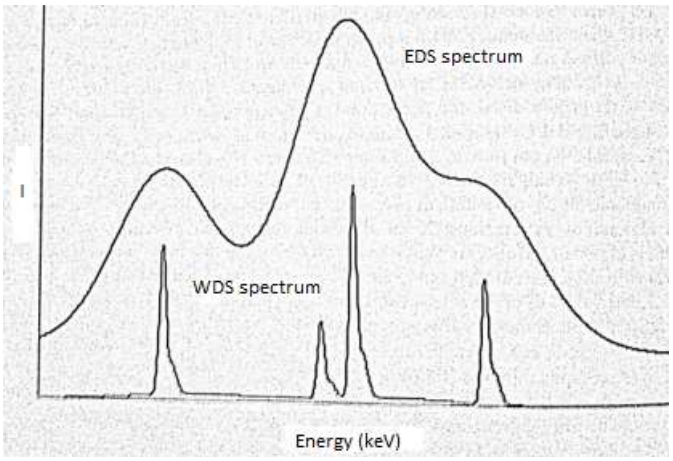

Figure 25: Comparison between EDS spectrum and WDS spectrum

The resolution of the EDS technique is sufficient to separate Kα lines of neighboring elements, but it is not sufficient to separate Kα lines and Kβ lines of Z and Z+1 elements in the range from Z = 16 (S) and Z = 27 (Co). Furthermore, lines L and M of elements with high Z numbers affect energies close to K lines of elements with Z lower, so that peak overlap in the EDS technique is normal and not an exception as in the WDS technique. As shown in the figure, the poor resolution of the EDS technique causes lines for close features come to overlap forming a single appearing peak. Recently also available solid-state Ge detectors (High Purity Ge detectors HPGe), which having a lower of electron-moon bonding lower than Si (ε= 3.0 eV), allow the resolution to be reduced to 120 to 130 eV for the MnKα characteristic line. Because of the low resolution and low P/B ratio, which characterizes the spectrum acquired in EDS the system has a rather low limit of detectability such that it is not suitable for the detection of trace elements (< 1 wt. %). Furthermore, these characteristics make the EDS system capable of acquire elements up to C and with much lower accuracies than for heavy elements. The EDS system has, however, the advantage of being rapid in acquisition on the order of a few minutes for the entire spectrum versus hours for the WDS system, since the acquisition of photons at various energies occurs simultaneously. In addition, the Sì(Li) detector is extremely sensitive that incident beam currents lower than those needed for the WDS technique are necessary. In the case of dealing with elements with high Zs (> 10) present in weight percentages greater than a few units, the EDS technique provides accuracies comparable to WDS because of the high peak P values, as long as one does not have an excessive number of overlapping peaks. For the acquisition of trace elements and light elements, the WDS technique is significantly superior to the EDS technique. The joint and complementary use of the EDS and WDS systems can ensure accuracy and rapid response, using the EDS system for elements major and high-Z elements and using the WDS system for trace and light elements.

2.7.4 Sample preparation

The electron beam is a current of electrons that procures, on an electrically non-conductive sample, the accumulation of a negative static charge with inevitable difficulties in image formation. Insulating materials, therefore, are covered with a conductive film that can generally be gold or carbon of such a small thickness (20 Angstroms) that the surface is not morphologically altered. The choice of material depends on the type of investigation to which the sample will be subjected: gold

for investigations of morphological features only, carbon for those concerning chemical constitution. The dimensions of the sample, in order to be easily "manageable," should be inscribed (maximum dimensions recommended) in a parallelepiped measuring 2.5cm x 2.5cm x 1.0 cm, with explorable faces the two largest. In the figures below, pictures of the SEM and its samples holder are reported in order to show the reason to have small samples. Furthermore, around 20 minutes of time are required to create the vacuum atmosphere in the chamber so in order to decrease the investigation time, several samples are observed at the same moment.

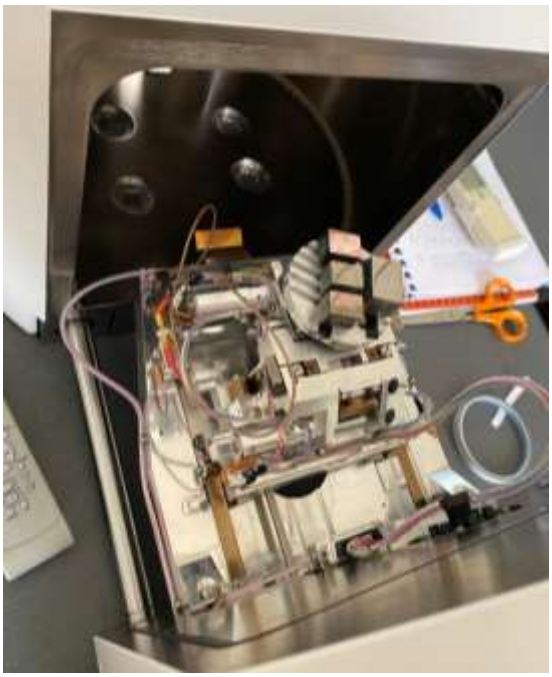

Figure 26 on the left: Sample holder of the SEM
Figure 27 on the right: SEM machine

3 CHAPTER 3

FIRST SET OF SAMPLES

The following chapter deals with the first set of samples and it has already been mentioned that it is made up of Alnico 5 alloy. First, the heat treatments with different parameters are done and then all the samples are investigated with several techniques. The results of the study are discussed in the last chapter.

3.1 HEAT TREATMENTS

It has already been mentioned that the heat treatments for the spinodal decomposition are made up of three steps: solubilization, annealing and step drawing annealing.

The first step of the heat treatment was done, on the suggestion of the professor, at 1250°C for 1 hour of time in the furnace with air. Afterwards, it was necessary to establish the different times and temperatures to develop the highest coercivity during the annealing heat treatment step. These temperatures were taken from the previous work of Veres Janos[30] and they are summarized in the following table:

A1	Annealing at 840°C for 15 minutes
A2	Annealing at 840°C for 1 hour
A3	Annealing at 650°C for 6 hours
A4	Annealing at 650°C for 6 hours and then 550°C for 24 hours
A5	Annealing at 730°C for 10 minutes
A6	Annealing at 700°C for 10 minutes
A7	Annealing at 670°C for 10 minutes
A8	Annealing at 600°C for 10 minutes

Table 6 Temperature and time parameters for the annealing step

The last step of heat treatments, known as step-drawing annealing, is postponed to the end of the experiment after the investigations are done.

3.2 HARDNESS TEST RESULTS

Hardness tests were done on the samples and the results are summarized in the following table:

	25	**REF**	**A1**	**A2**	**A3**	**A4**	**A5**	**A6**	**A7**	**A8**
	[HV30]	[HV30]	[HV30]	[HV30]	[HV30]	[HV30]	[HV30]	[HV30]	[HV30]	[HV30]
	624	523	487	442	558	605	520	554	550	561
	580	532	472	455	562	612	537	558	561	547
	584	493	419	436	568	602	554	583	568	568
	575	547	456	465	577	599	547	550	565	540
	544	489	459	455	553	609	550	580	550	540
mean	583,5	516,8	458,6	454,67	564,3	605,4	541,6	565	558,8	551,2
standard dev	26,06	25,1	25,3	14,35	8,5	5,22	13,61	15,36	8,41	12,72

Table 7 Hardness test results on the first set of samples

The main function of the results of the hardness test is to track the changes in the mechanical properties during the heat treatment and the spinodal decomposition, and to check if there is a correlation between the spinodal decomposition and the mechanic properties.

3.3 MAGNETIC PROPERTIES TEST RESULTS

Magnetic properties were tested on the samples to keep track of the spinodal decomposition. The first test was done on the original sample as it had been used as a reference for the other samples. The results of these tests are summarized in the *Chart 1*. The chart represents magnetic properties of the original sample, the homogenized sample and of the annealed samples using different time and temperatures parameters. Origin Pro 9.0 software had been adopted to analyze the data received from the Steblein-Steiner tester.

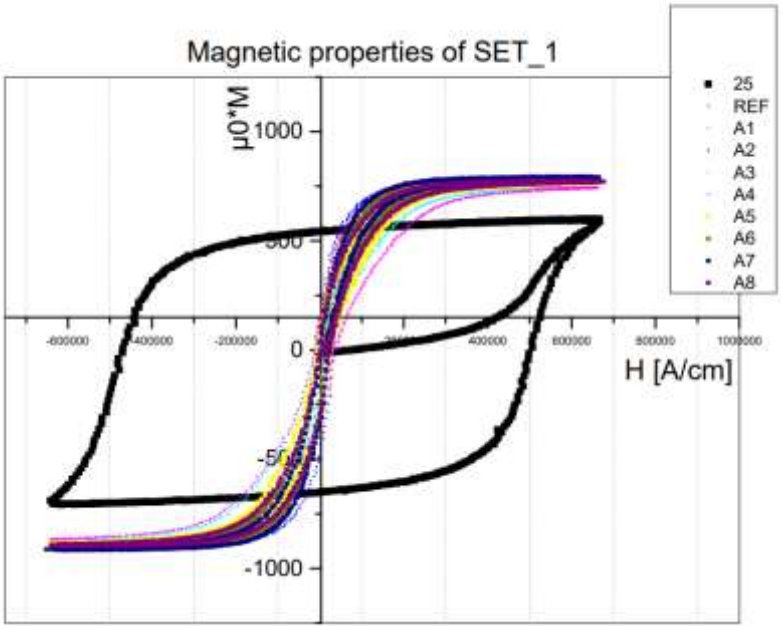

Chart 1 Hysteresis loops of the several samples from the set number one.

It is clear from the chart, observing the coercivity of the different specimens on the x-axis, that no specimen demonstrated the expected result. Then, it is legitimate to state that the experiment did not work as the main purpose of it was not achieved. The possible reasons of the failure of the experiment must be discussed.

3.4 DISCUSSION ON THE MAGNETIC TEST RESULTS

As the magnetic test results showed, the coercivity, which is strictly related to the spinodal decomposition, had not been developed. It is now necessary to analyze the possible reasons of why the experiment may not have worked. This work is necessary in order to adjust previous heat treatment conditions and to be able to obtain satisfactory results in the future experiments.

There are already some suspects about the oxidant atmosphere of the furnace (as in many articles on this work vacuum furnace or a protective gas are used during the first step of the heat treatment),

but also, the contact with carbon steel could represent a problem as carbon is a damaging element for the Alnico alloys. Another reason of the failure could be found in the phases diagram as there is a range of temperature where a new phase, which blocks the development of magnetic properties, is formed. These suggestions will be discussed in the next paragraphs.

Oxidant atmosphere

The first suspect about the failure of the experiment is the presence of air in the furnace atmosphere. Knowing the tendency of metals to oxidize at high temperatures, the concern here is that the main elements of the Alnico alloy, so aluminum, nickel and cobalt, may have oxidized, changing the chemical composition of the alloy and compromising its potential to be magnetized during heat treatment process. Moreover, analyzing the other works, where heat treatments are done on Alnico alloys, there is no work where explicitly oxygen atmosphere was adopted. Conversely, in many works it is specified that vacuum furnace was used in order to process the material in an inert atmosphere[12,14,17].

The assumption involving the oxidizing atmosphere needs to be validated with a proof. This could be the identification of new phases in the microstructure of the material not predicted by the phase diagram and composition of the material. For this purpose, optical and electron microscopy accompanied by EDS probe composition analysis is used. If new phases related to the oxidant atmosphere are identified the assumption can be accepted as a possible reason of why the heat treatments did not work on the samples.

Carbon contact

As it has been illustrated before, the furnace was equipped with a carbon steel box to hold together all the samples during the homogenizing step of the heat treatment. Nevertheless, the influence of the several elements on the alloy have not been discussed. Indeed, it was found in the investigation of Veres Janos[30] that carbon is a deleterious element for the magnetic properties of the Alnico alloys as it improves the precipitation of the γ_1 phase. Nothing more is written about it so the gravity of the presence of carbon in the carbon steel material of the sample holder is not known. Thus, some investigations will be done.

To study the impact of carbon, optical and electronic observations are done as well. In fact, the same strategy of the previous case is used in this case too. From the micrographies, it should be seen the occurrence of new phases to confirm the supposition of the influence of the sample holder because of the carbon. Otherwise, it is possible as well that the content of carbon in the carbon steel is too low to influence the composition of Alnico samples.

Another fundamental technique for this investigation is X-ray diffraction. Considering that the γ_1 phase lattice parameters are different from the α_1 and α_2 phase lattice parameters, using XRD would be possible to underline the appearance of a consistent quantity of γ_1 phase and the reason could be the contact with carbon steel. Unfortunately, XRD technique is not available for this project.

Process parameters

The last proposed supposition to explain the failure of the heat treatment is the choice of the wrong process parameters. It had already been discussed in the paragraph on solubilization of the first chapter that there is a possibility of formation of the undesired γ_1 phase which can compromise the development of the magnetic properties. The phase appears if the alloy is taken under particular temperature and time condition or if the alloy is taken to these conditions following a particular path during the cooling process. For these reasons, a fast cooling and appropriate temperature and time parameters are important.

Regarding to the time and temperature parameters, it was decided that the temperature set at 1250°C is correct, as from several phase diagrams this value seems to be high enough to avoid the γ_1 region. The temperature value has to be high as if the cooling is carried out from temperatures too low, then an undesired microstructure made up of $\alpha_1 + \alpha_2 + \gamma_1$ will be produced, instead of the $\alpha_1 + \alpha_2$ wondered combination. The time of the treatment, on the other side, is considered to be too long as further unwanted phase could appear when the spinodal decomposition has already started.

For what concerns the cooling step, some further considerations were done. It is possible to measure the cooling rate using the thermocouples with the metallic wires attached to the samples in the furnace but unfortunately this tool is not available for this work. Therefore, the cooling rate is unknown. Nevertheless, if that should have been the problem it is still possible to manipulate the cooling rate working on the cooling process. So, for instance, if the cooling rate was too slow then cold water would be used. Vice-versa, if the cooling rate was too fast then the cooling process could be done in the air using the natural convection.

4 INVESTIGATION ON THE FAILURE OF THE FIRST SET

The results of further investigations on the first set of samples are presented and discussed in this chapter. To be noticed that not all the samples are analyzed, only the characteristic ones. These are sample 25, samples REF_1, RER_2, REF_3 and sample A1. The thermal history of each sample is shown in the table below:

Samples	Thermal history
25	original sample before heat-treatments
REF_1, REF_2, REF_3	homogenized samples
A1	homogenized and annealed sample

Table 8 Thermal history of the investigated samples

The investigations are done in order to identify and to discuss the reasons of the failure of the experiments. As it has already been stated, there are three main suggestions. The best strategy to confirm or to deny the hypotheses of the failure is the XRD, but this technique is not available. Thus, other techniques are exploited with the same purpose. These are the investigations with optical microscopy and electronic microscopy. Moreover, the results of the electronic microscopy are accompanied with the EDS analysis. The main goal is to identify characteristic differences between the original sample and the heat-treated samples, and to check if these differences can represent a proof for the assumptions about the failure of the experiment made in the last chapter.

4.1 INVESTIGATION WITH OM

Several samples had been investigated and it was decided to analyze only the representative ones. The representative ones are the samples which certify the condition of the material at the key points of the heat treatment. Thus, a sample named ''25'' was chosen to represent the original state of the samples. Samples REF_1, REF_2, and REF_3 were chosen to represent the homogenized state of the material and sample A1 was chosen to represent the annealed state. Then, observations with several magnification were done and the most representative micrographies are reported and discussed below.

4.1.1 Sample 25

The micrographies of the original sample are shown in the *Figure 28* and *Figure 29*. It can be deduced from the observation that the grains are quite big and that some precipitation particles are present along the grain boundary but also within the grain. These micrographies will be kept as a reference for the future investigation. In order to have more information about the original sample, beside the already known average composition, other composition analyses can be done. It would be interesting to measure the composition of two different grain and to measure the composition of the precipitated particles. These analyses will be done with ESD technique in the future paragraphs.

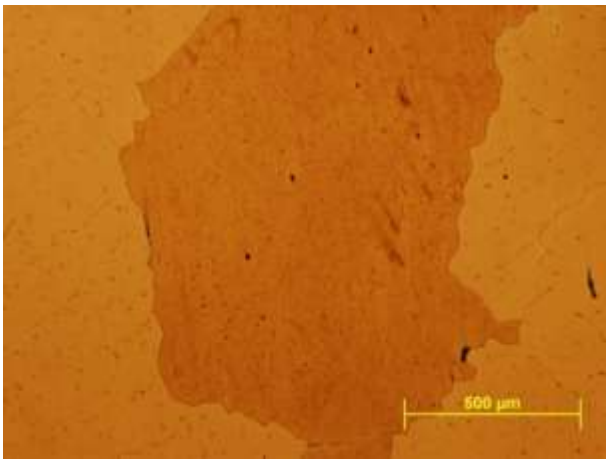

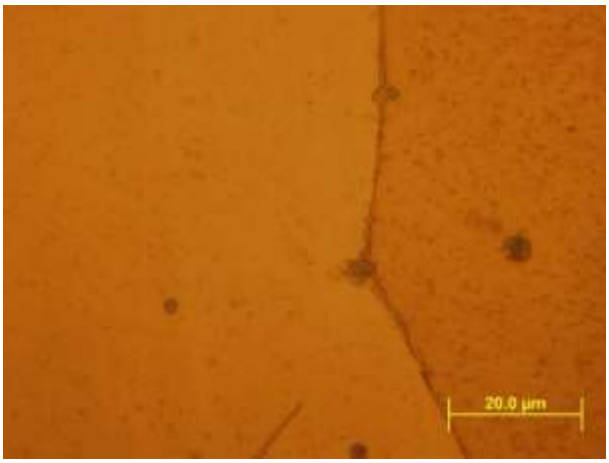

Figure 28 Micrography of the original sample with magnification x50

Figure 29 Micrography of the original sample with magnification x1000

After having analyzed the original sample and have taken the necessary micrographies to have a point of reference for the further investigations, the other samples were studied. It was decided to observe more samples after the homogenizing heat treatment to have more consistent data. Also, all the faces of a sample were observed. The reason of this procedure is that only one face of the samples was in contact with the carbon steel material of the box and after the heat treatment the face in contact was not marked. In this way, analyzing all the faces of three characteristic sample the results of the study can be considered reliable.

The observations with the optical microscope were done and some important results came out. Regarding to the the original sample, other notable features of the microstructure appeared. The new observed elements are not known so they will be called in the following chapter with some characteristic names or codes. In general, four different new elements appeared on the microstructures. These will be shown and discussed below.

4.1.2 Samples REF_1, REF_2, REF_3

First part

The first new element observed with OM is a small and completely *black area* on the samples REF_1 and REF_2. These elements are rare on the faces of the samples and were not found on all the samples. This appearance must be discussed .

First of all, the samples were cleaned multiple times with ethanol so unlikely these black elements are some kind of pollution. Also, they represent an evident difference between homogenized samples and the original samples so they should be analyzed. Using EDS composition analysis, the composition of the black area can be measured and the new element can be identified. This study will be done in the SEM and EDS paragraph.

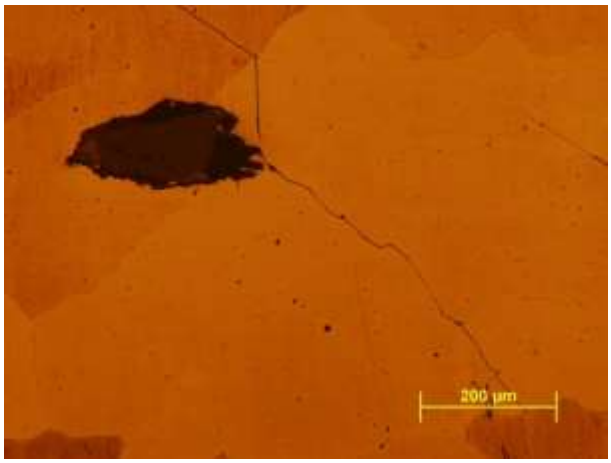

Figure 30 Micrography of the homogenized sample REF_1 with magnification x100 where a completely black area can be seen

Second part

Another new and interesting element which had been observed with the optical microscopy is a *black and white region*. These elements were not found on all faces of the samples as well but multiple of them were present on the same face when they were detected. They are shown in the below.

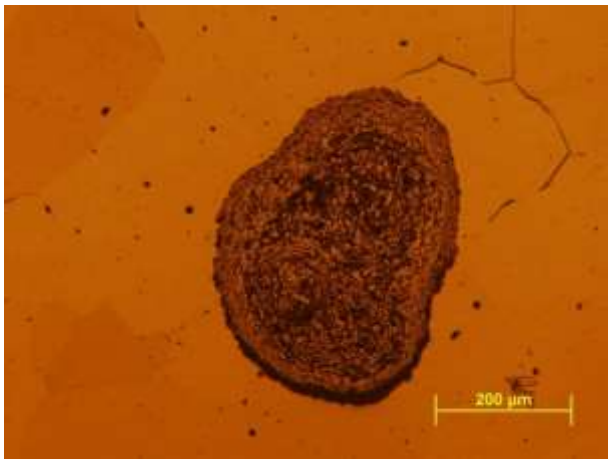

Figure 31 Micrography of the homogenized sample REF_3 with magnification x100

Some other important features can be observed in both of the previous micrographies: the small, black dots. These elements must also be investigated with the EDS analysis.

4.1.3 Sample A1

Sample A1 was analyzed as well with the aim of having as much information as possible about the new elements after the annealing step. In the *Figure 32*, an anomalous region with a particular texture, very similar to the already seen black and white region, was detected. As in the previous case, nothing more can be said about it.

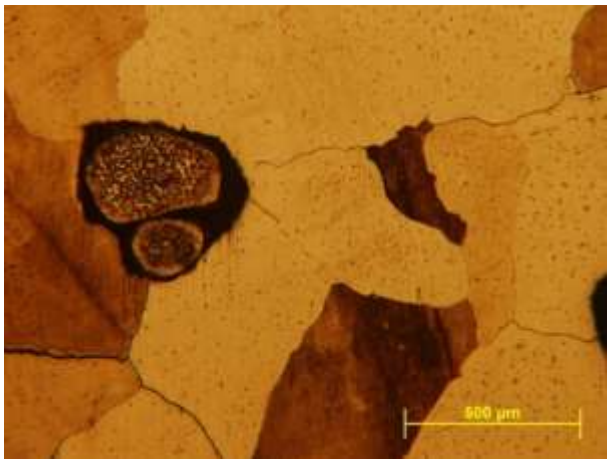

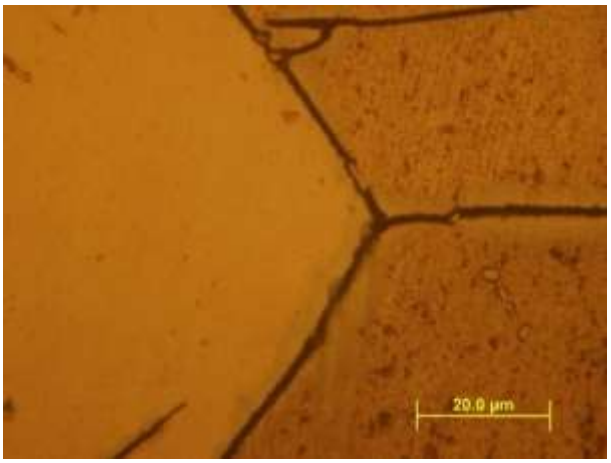

Figure 32 Micrography of annealed sample A1 with magnification x100

Figure 33 Micrography of the annealed sample A1 with magnification x1000

Another interesting analysis that could be done on the heat-treated samples is the comparison between the small, precipitated particles. it is not taken for granted that the composition of the precipitated particles of the original sample is the same of the precipitated particles of the heat-treated samples. This analysis will be done with the EDS technique as well.

4.2 Investigation with SEM and EDS

After optical microscopy it's clear that there are several elements that need to be elaborated as the optical microscopy can only provide micrographies with limited magnification and no information about the composition. These are the reasons why other techniques as SEM and EDS were adopted. The first one, SEM, is used to obtain bigger magnifications while the second one is used for the spot and average composition analyses. The results of these tests on the samples chosen for the investigation are illustrated below.

As it had been done with optical microscopy, only characteristic samples were analyzed in order to verify the conditions of the material after the main steps of the heat treatment. Moreover, only a few of the chosen samples for the optical microscopy were analyzed with SEM and EDS; the ones that presented new features in relation with the original samples. The main purpose at this point of the investigation is to identify the new elements that appeared on the treated samples. Thus, the assumptions made previously about the failure of the experiment can be confirmed or rejected.

4.2.1 Sample 25

The original sample was analyzed in order to obtain further information on its particular features. After the average composition on a big area of a face of the sample presented at the beginning of *Chapter 2*, other composition analyses were done. The attention at this point is focused on the composition of different grains and on the precipitated particles already detected with OM. The results are reported in the figures below.

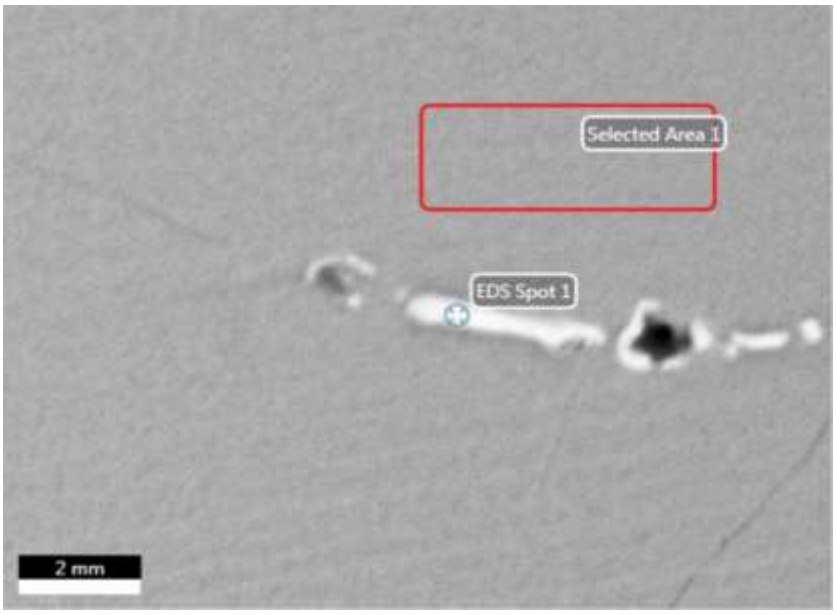

Figure 32 SEM micrography of the original sample 25

As it can be seen from the SEM micrography in the *Figure 32*, a spot EDS analysis was done on the precipitate particle and an average analysis was done on the grain next to the precipitated particle. The composition analysis results are the followings.

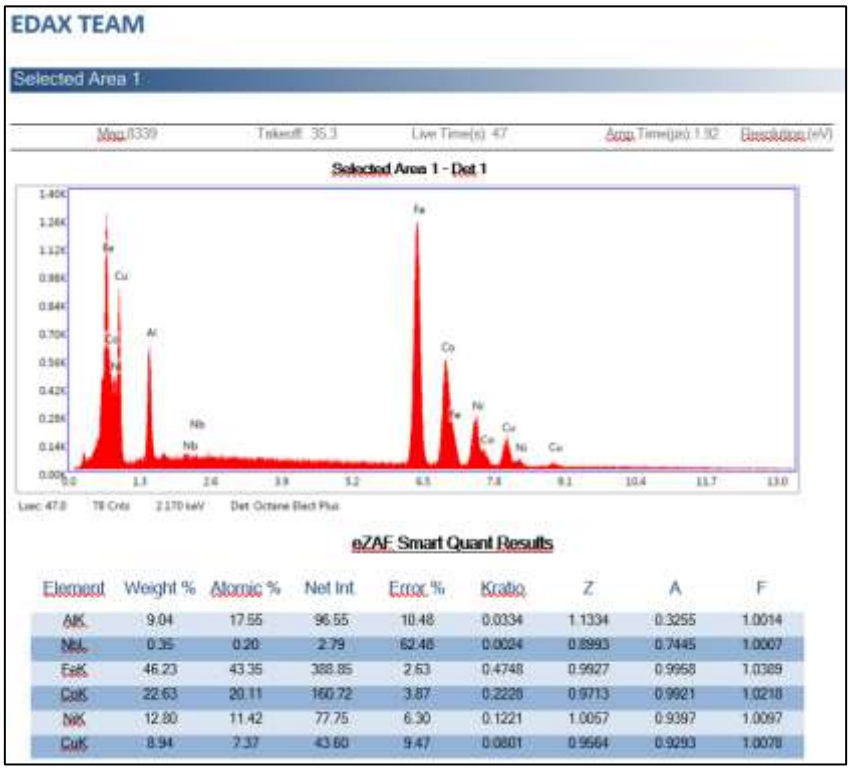

Element	Weight %	Atomic %	Net Int.	Error %	Kratio	Z	A	F
AlK	9.04	17.55	96.55	10.48	0.0334	1.1334	0.3255	1.0014
NbL	0.35	0.20	2.79	62.48	0.0024	0.8993	0.7445	1.0007
FeK	46.23	43.35	388.85	2.63	0.4748	0.9927	0.9958	1.0389
CoK	22.63	20.11	160.72	3.87	0.2228	0.9713	0.9921	1.0218
NiK	12.80	11.42	77.75	6.30	0.1221	1.0057	0.9397	1.0097
CuK	8.94	7.37	43.60	9.47	0.0801	0.9564	0.9293	1.0078

Figure 33 EDS average composition analysis of the original sample

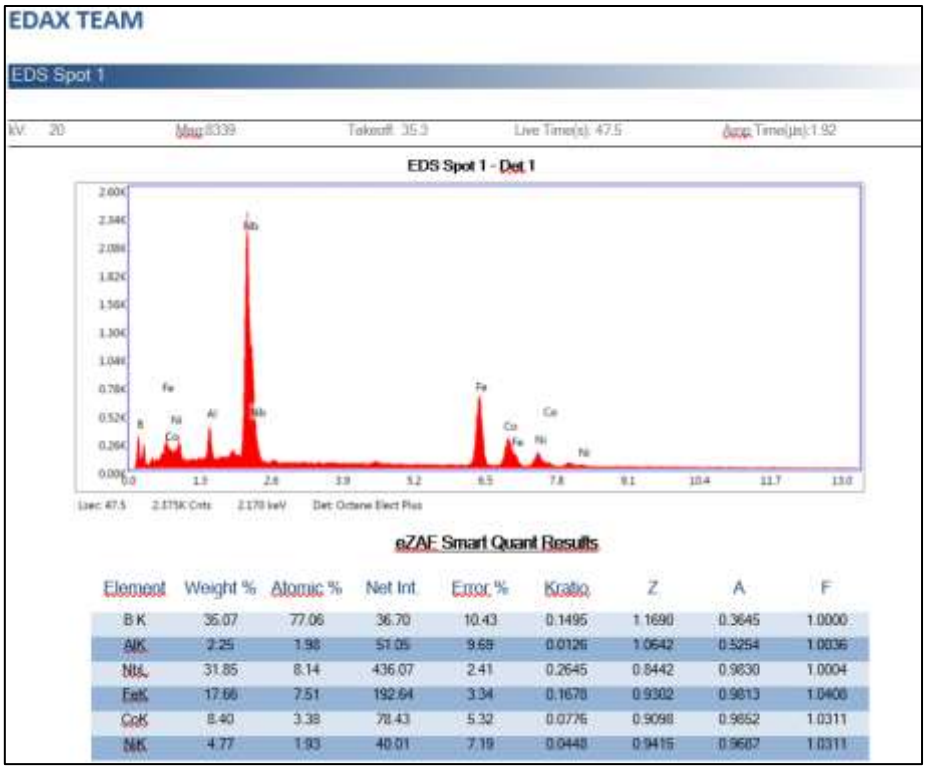

Figure 34 EDS spot composition analysis of the original sample

It must be noticed that small amounts of Niobium are present in these Alnico 5 samples. Usually, niobium is added to Alnico alloys to improve the grain size and this improvement has benefits on the magnetic properties. There is plenty of this element in the precipitates, as the micrographies shows.

Now, everything needed is known about the original sample so a comparative investigation with the remanent samples can start.

4.2.2 Sample REF_3

It was observed that, after having done the optical microscopy analysis, the most meaningful sample of the type ''Reference'' is the sample REF_3 as it contains a lot of typical features that must be investigated. The features to investigate are the black and white regions and the black dots. Another important task to do is to measure the composition of the precipitated particles in the heat-treated samples and to compare it to the composition of the precipitated particles of the original sample already measured.

The results are illustrated separately in two parts. The first part deals with the black and white region while the second part deals with the black spots and with the precipitated particle.

Part 1

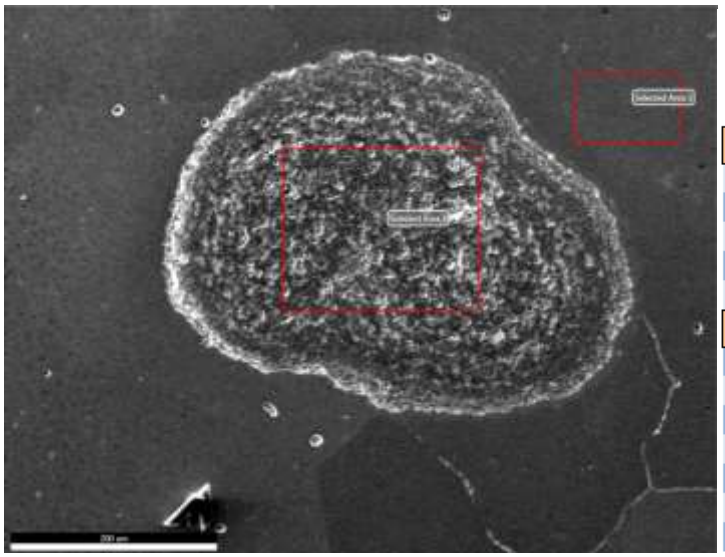

eZAF Smart Quant Results

Element	Weight %	Atomic %	Net Int.
AlNiCo | New Sample | Area 10 | Selected Area 2			
O K	20.8	42.97	282.47
AlK	17.63	21.6	274.53
FeK	27.65	16.37	274.57
CoK	22.18	12.44	183.73
NiK	11.75	6.62	85.52
AlNiCo | New Sample | Area 10 | Selected Area 3			
AlK	9.47	18.19	154.68
SiK	0.17	0.31	3.46
NbL	0.38	0.21	4.49
FeK	48.41	44.9	600.43
CoK	24.21	21.28	252.56
NiK	14.3	12.62	127.9
CuK	3.06	2.49	22.03

Figure 35 on the left: SEM micrography of sample REF_3
Table 9 on the right: EDS composition analysis of Area 2 and Area 3 of the REF_3 sample

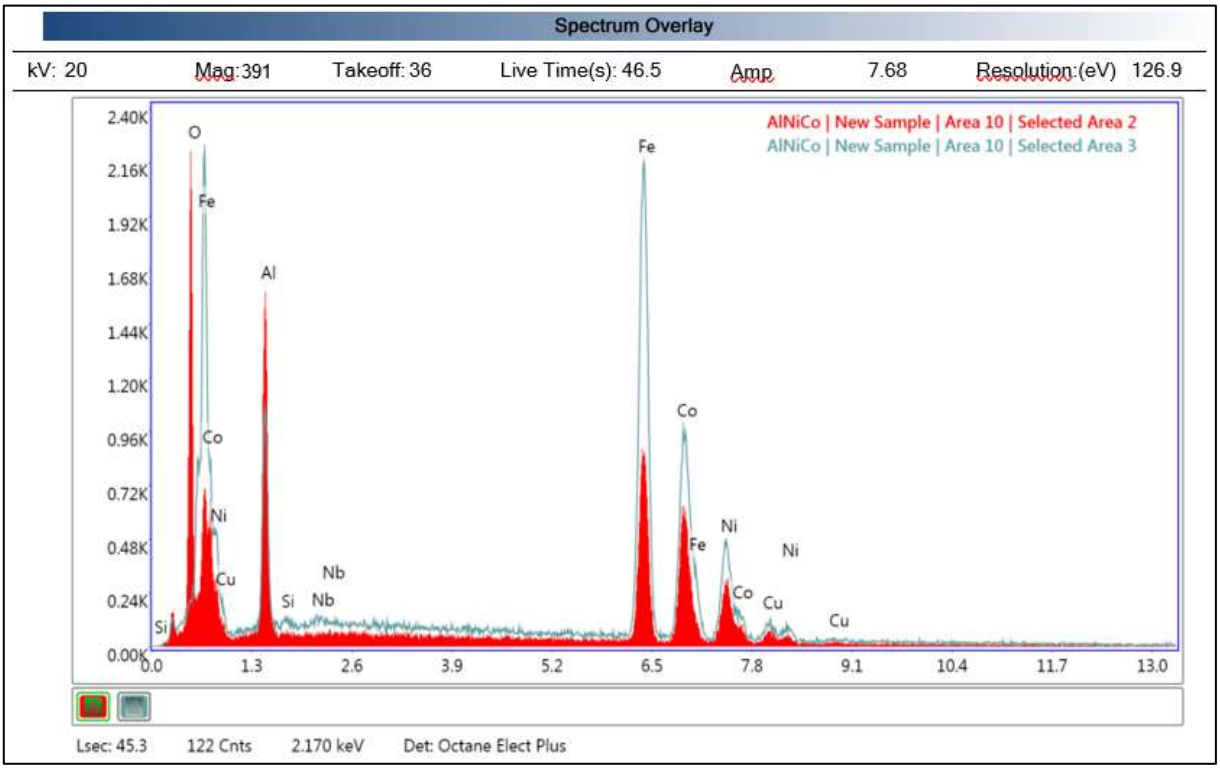

Figure 36 EDS spectrum of the composition analysis on the sample REF_3

After having investigated the black and white regions with the EDS analysis there is now a new information about the composition that is fundamental in the characterization of this feature. A consistent peak of oxygen was detected. As the heat treatments were done in the oxidant atmosphere these results are meaningful and fit the experimental conditions. It is legitimate to state that a local oxidation took place in the samples. Moreover, a big peak of aluminum was detected.

This result reflects the theoretical consideration, as aluminum is an element that oxidates at high temperatures, and represents a good proof for the oxidation supposition.

Part 2

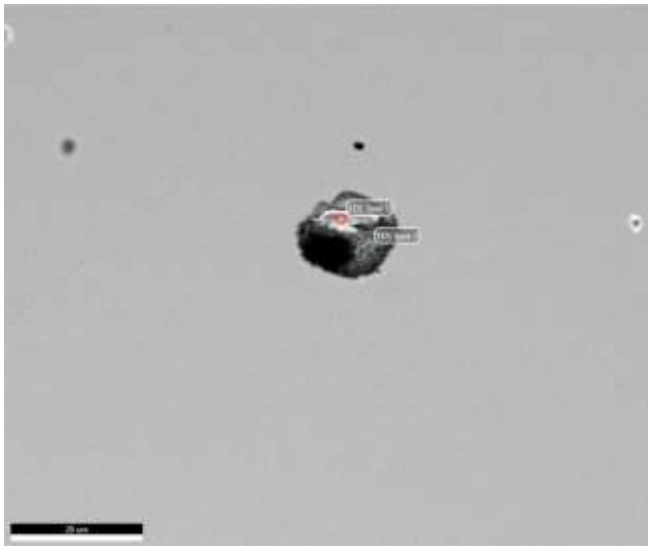

Figure 37: another SEM micrography of sample REF_3

eZAF Smart Quant Results

Element	Weight %	Atomic %	Net Int.
AlNiCo | New Sample | Area 11 | EDS Spot 1			
AlK	1.59	3.7	24.52
NbL	57.53	38.93	544.2
S K	14.01	27.47	257.35
TiK	0.77	1.01	8.21
FeK	17.76	19.99	132.12
CoK	8.35	8.91	54.21
AlNiCo | New Sample | Area 11 | EDS Spot 2			
AlK	7.3	14.29	107.81
NbL	0.2	0.12	2.22
FeK	52.82	49.98	597.7
CoK	26.1	23.4	248.06
NiK	13.57	12.21	110.33

Table 10: EDS composition analysis of REF_3 sample; Area 2 and are 3 from the micrography in Figure 39

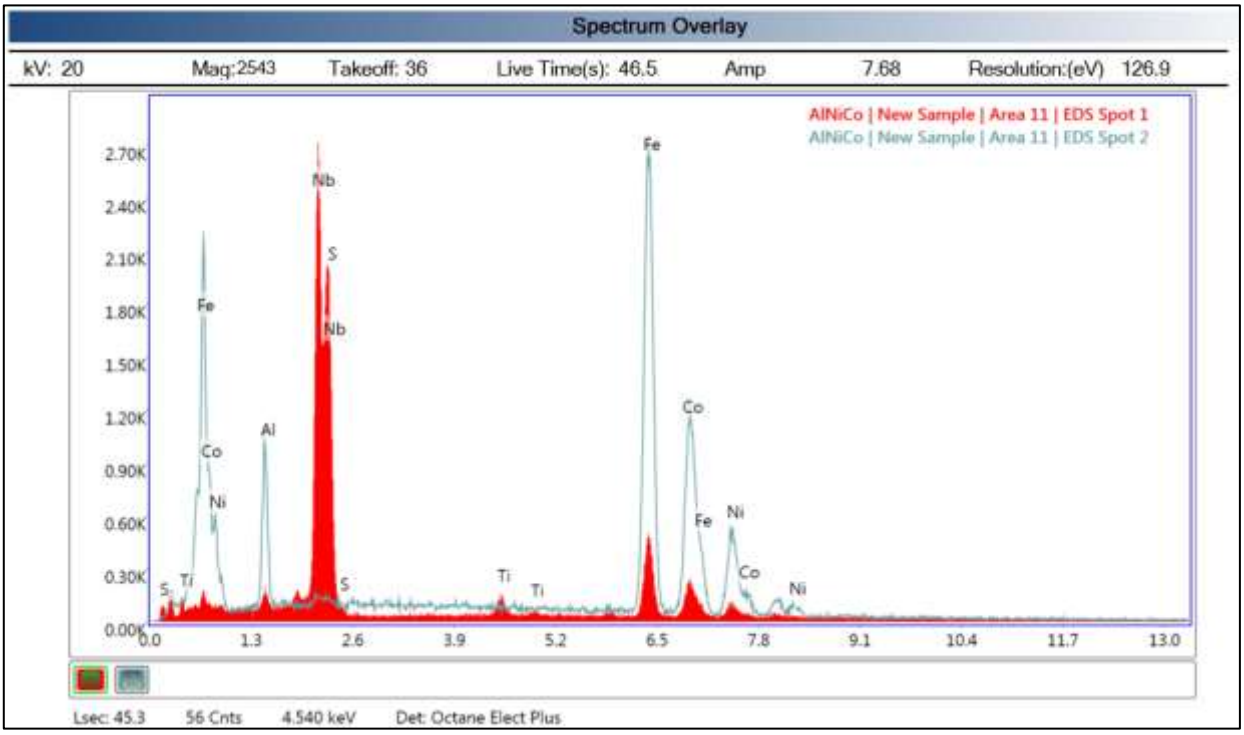

Figure 38 EDS spectrum of the composition analysis on the sample REF_3

It has been found from the EDS analysis that the *spot 1* contains Sulfur (*Table 10*). This result can be explained as pollution from Marble's etching agent where $CuSO_4$ is one of the main reagents. Thus, the black spots are not more considered for the explanation of the failure of the heat

treatments. Spot 2, on the other side, contains big amount of iron and cobalt. The composition of the precipitated particle of the heat-treated sample are very different form the composition of the original sample particle. This result will be discussed at the end of the chapter.

4.2.3 Sample A1

The anomalous grain of the sample A1 was checked as well with SEM and EDS techniques. The results show a coherent distribution of the elements inside the grain so this can't be linked with the failure of the experiment. The results are reported below.

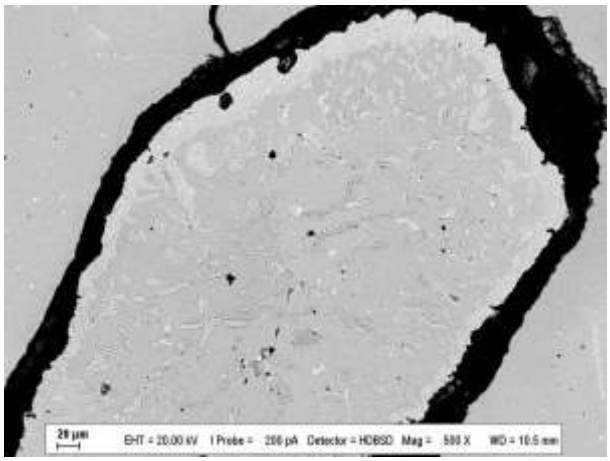

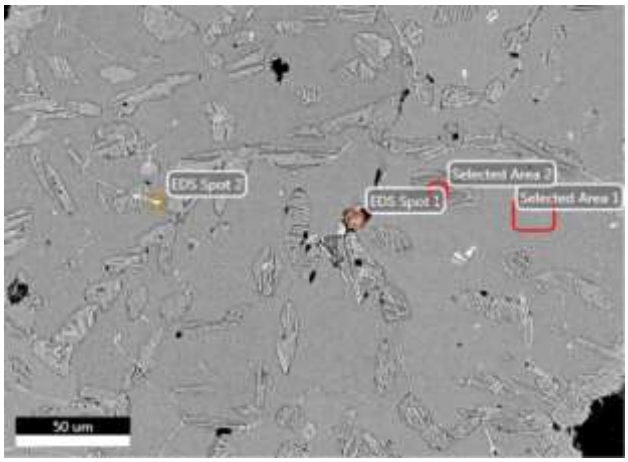

Figure 39 on the left: SEM micrography of the annealed sample A1

Figure 40 on the right: SEM micrography of the annealed sample A1 with higher magnification

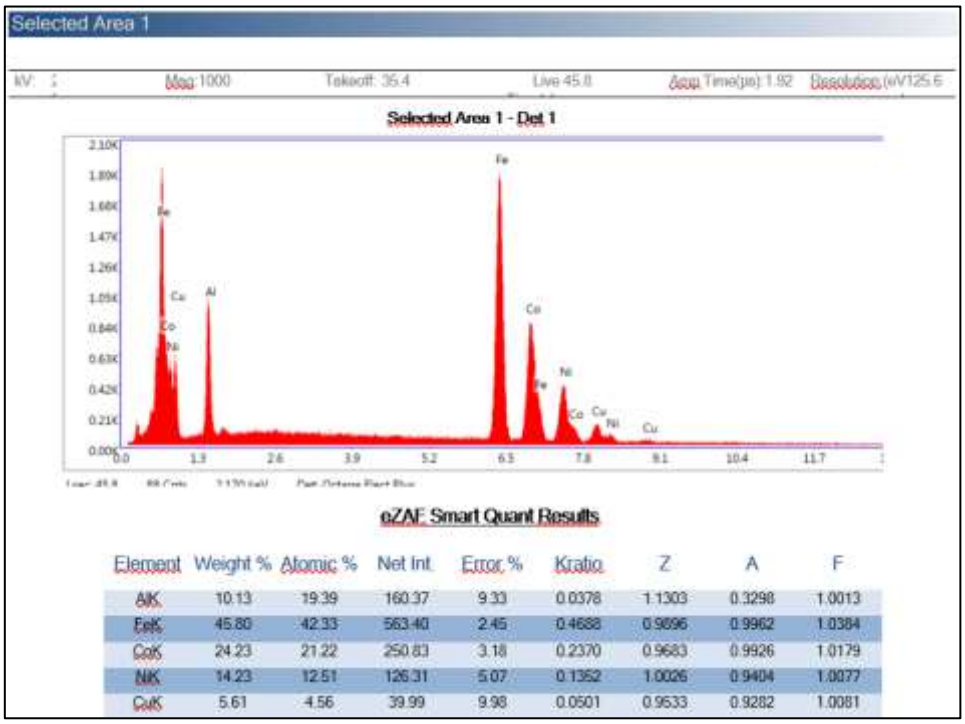

Element	Weight %	Atomic %	Net Int.	Error %	Kratio	Z	A	F
AlK	10.13	19.39	160.37	9.33	0.0378	1.1303	0.3298	1.0013
FeK	45.80	42.33	563.40	2.45	0.4688	0.9896	0.9962	1.0384
CoK	24.23	21.22	250.83	3.18	0.2370	0.9683	0.9926	1.0179
NiK	14.23	12.51	126.31	5.07	0.1352	1.0026	0.9404	1.0077
CuK	5.61	4.56	39.99	9.98	0.0501	0.9533	0.9282	1.0081

Figure 41 EDS analysis on the annealed sample A1, Area 1 on the micrography

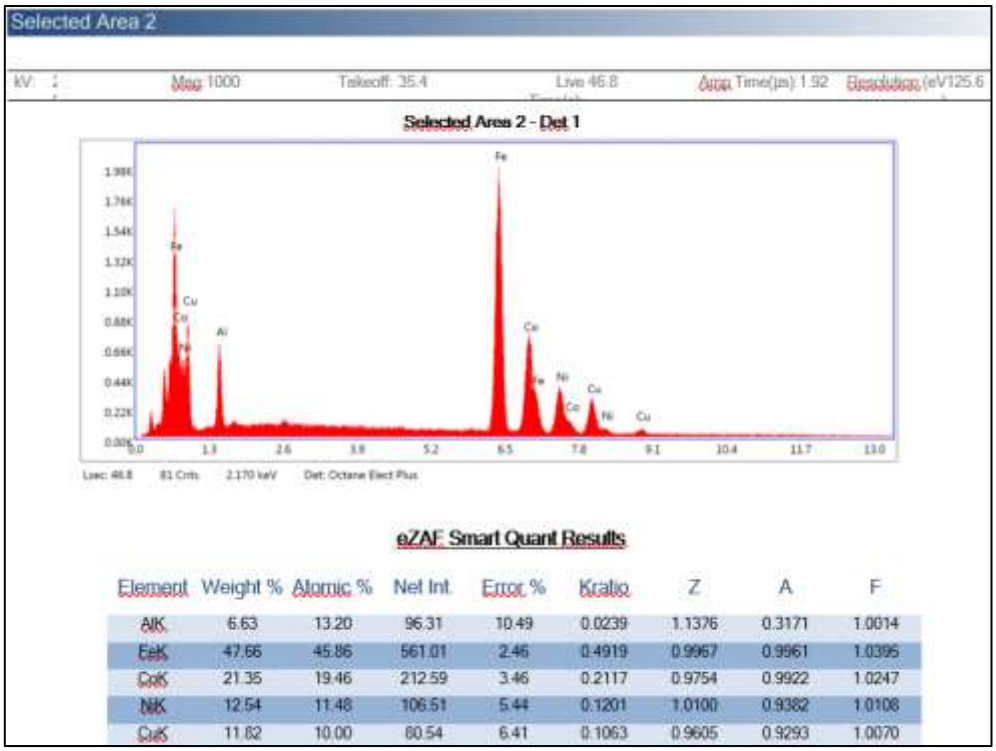

Figure 42 EDS analysis on the annealed sample A1, Area 2 on the micrography

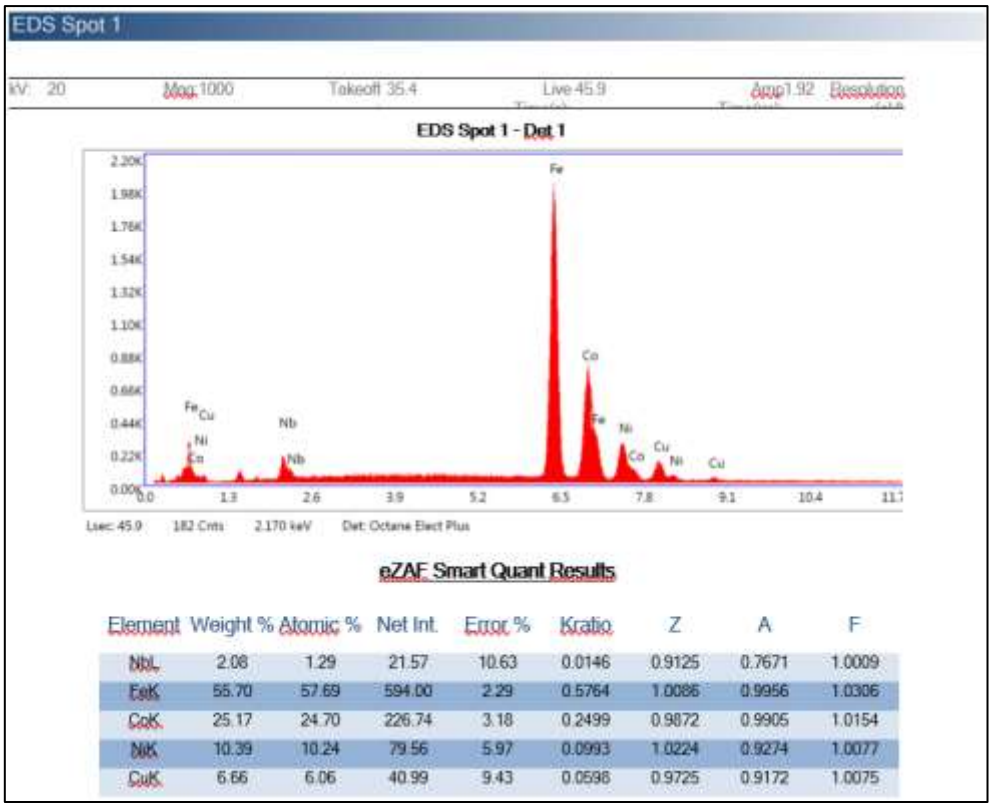

Figure 43 EDS analysis on the annealed sample A1, Spot 1 on the micrography

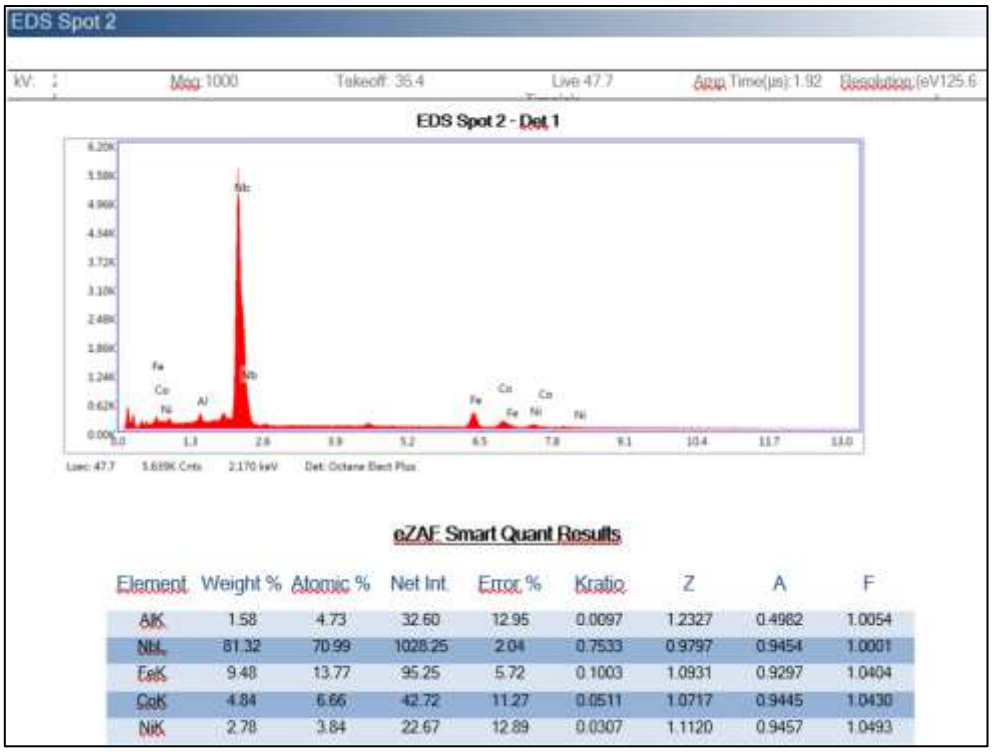

Figure 44 EDS analysis on the annealed sample A1, Spot 2 on the micrography

4.2.4 Sample C1

A sample of the third set was used for the compositional analysis of the black area. Sample C1 is made up of the same Alnico 5 material and it is heat-treated in similar conditions. The black area features are identical to the ones seen in the first set samples, so it was considered fair to take this sample as the reference for the investigation. The reason of this move is that on the C1 sample there is plenty of black areas, so it was quite simple to detect and to analyze them.

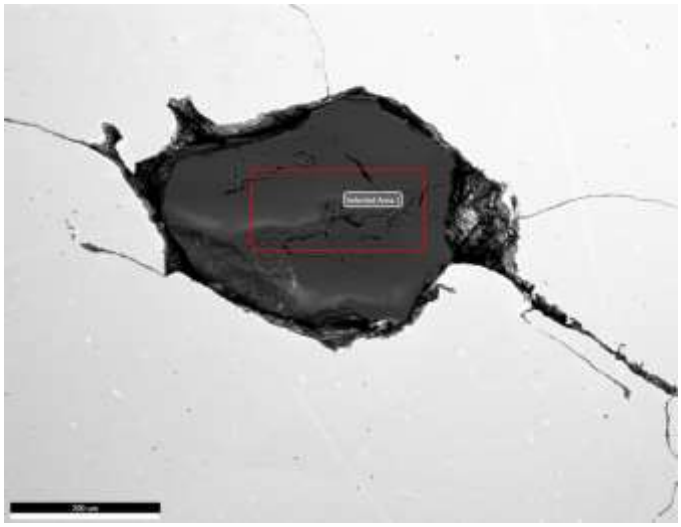

eZAF Smart Quant Results

Element	Weight %	Atomic %	Net Int.
O K	52.87	66.33	696.65
SiK	47.13	33.67	1827.68

Figure 45: SEM micrography of C1 sample on the left; EDS composition table on the right

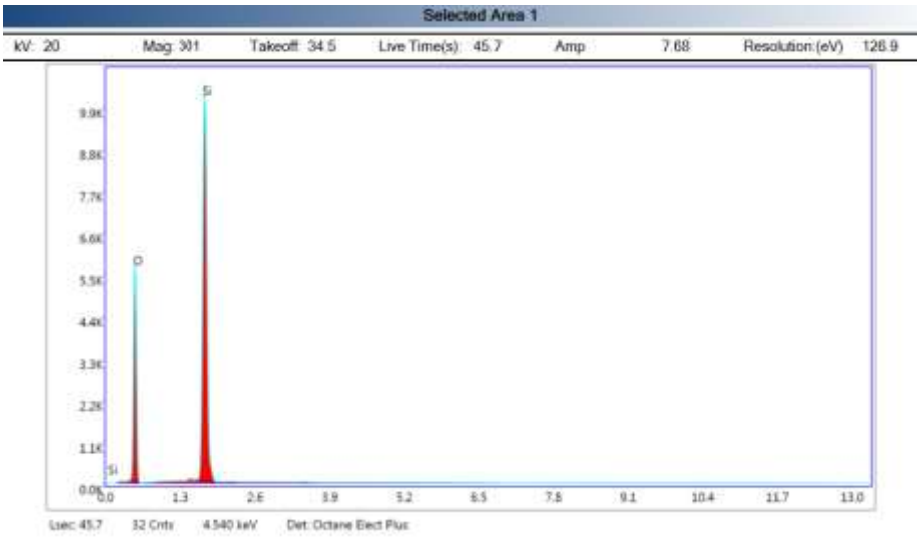

Figure 46 EDS composition analysis chart

The composition analysis result shows that the completely black is a ceramic particle which is not predicted by the composition of the alloy. The explanation is quite simple: it is a sort of pollution particle that was introduced on the sample by grinding operation. In any case, the is no reason to link this appearance to the possible cause of the failure of the heat treatment process. In fact, *Figure 46* shows that there is no trace of the alloy composition so the black area can be considered as an external body.

4.3 CONCLUSIONS

After having analyzed the selected samples with OM, SEM and EDS, a more complete discussion can be done on the samples and the heat treatment process. It was clear from the magnetic test results that the heat treatment did not work, as the magnetic properties were not developed. The investigation of this chapter is aimed at confirming or refuting the theoretical assumptions made at the beginning. In the following paragraph these assumptions will be discussed considering the new results.

4.3.1 Black and white regions

The most interesting result is for sure the EDS composition analysis on the black and white regions. After having found big amounts of oxygen in these elements, not predicted from the phase diagrams and from the composition of the alloy, it is legitimate now to confirm the assumption of the oxidizing atmosphere as a possible reason of the failure of the experiment.

The composition analysis confirmed that new phases containing oxygen appeared in the material. Firstly, it could be stated that in this way the local composition of the alloy is changed as some amounts of aluminum were employed in the formation of this phase, so this is the reason of the failure of the experiment. Nevertheless, the complete correlation between the appearance of these phases and the poor magnetic properties can’t be approved as the mechanism behind is not clear.

So, in view of these results, it is legitimate just to confirm that the assumption of the oxidizing atmosphere is correct, but this assumption can't exclude the other assumptions made or not made yet.

4.3.2 Precipitated particles

Another interesting result concerns with the detection of big amounts of iron and cobalt in the precipitate particles. It can be noticed from the results that the precipitates detected in the sample 25 are different from the precipitates detected in the samples ''reference'' as the composition is completely different. Also in this case, the local concentration of the alloy is changed as the amounts of iron and cobalt are employed in the formation of the precipitates. The spinodal decomposition process then can be affected as the main condition, the composition, is not respected anymore. Nevertheless, it is not clear the mechanism and the reason of the precipitation of these elements so no theoretical assumption on the failure is made.

5 CHAPTER

SECOND SET OF SAMPLES

Since the first heat treatment was unsuccessful, it was decided to repeat the experiment on another set of specimens. The new samples are made of Alnico 2 alloy, which composition was already reported alongside the composition of the first set of the samples. It was also decided to make some modifications on the solubilization heat treatment in order to not to fail again.

5.1 HEAT TREATMENTS

The modifications to the heat treatment conditions are linked with the possible reasons of why the first work failed. Therefore, oxidizing atmosphere was replaced with a shielding gas (argon), the box containing the samples was made of stainless steel and the samples were cooled in oil and no longer in water to avoid to damage the surface too much. Some pictures of the new modified furnace are shown in the *Figure 47*. It is possible to see that the chamber is closed, and a pipe with the gas blowing in the chamber is introduced through the furnace

Figure 47: pictures of the modified furnace

There are 12 samples in the second set and all of them were subjected to the initial solubilization treatment at the temperature of 1250°C for 20 minutes with a shielding gas. The temperatures and the times for the annealing step were selected following a strategy of another work made by L. Zhou, W. Tang et al.[12] The strategy is to determine the best temperature keeping the time fixed on a certain value, and then to determine the best time with the best temperature chosen fixed. It was decided to fix the time to ten minutes for the first part of the heat treatment where several temperatures had been tried.

The different temperatures and times are illustrated by the following table. The table has also the aim to uniquely correlate the specimens with their thermal history.

Sample	Heat treatment
B1	Homogenizing step + 750°C for 10 min
B2	Homogenizing step + 790°C for 10 min
B3	Homogenizing step + 820°C for 10 min
B4	Homogenizing step + 850°C for 10 min
B5	Homogenizing step + 750°C for 20 min
B6	Homogenizing step + 880°C for 10 min
B7	Homogenizing step + 850°C for 20 min
B8	Homogenizing step + 850°C for 40min
B9	Homogenizing step + 850°C for 60 min
B10	Homogenizing step + 850°C for 5 min
B11	Homogenizing step + 790°C for 5 min
B12	Homogenizing step + 880°C for 5 min
B13	Homogenizing step + 820°C for 20 min
B14	Homogenizing step + 850°C for 10 min + 600°C for 8h step-drawn
B15	Homogenizing step + 850°C for 10 min + 600°C for 24h step-drawn
NEW_REF	Homogenizing step at 1250° for 20 min
NEW	Not heat treated

Table 11 new time and temperature schedule of the heat treatments for the samples

5.2 HARDNESS TEST RESULTS

After the heat treatments the samples were cleaned and grinded to the 320 Grit grinding papers. Then the hardness test was done. The hardness results are shown in the following table.

Sample	Heat treatment	Mean hardness [HV_{30}]	Standard deviation [HV_{30}]
NEW	Not heat treated	582,2	19,4
NEW_REF	Homogenized at 1250° for 20 min	556,8	8,8
B1	Homogenized + 750°C for 10 min	650,4	4,5
B2	Homogenized + 790°C for 10 min	597,7	8,5
B3	Homogenized + 820°C for 10 min	573,4	5,8

B4	Homogenized + 850°C for 10 min	561,0	11,5
B5	Homogenized + 750°C time 20 min	592,2	18,9
B6	Homogenized + 880°C for 10 min	522,7	39,2
B7	Homogenized + 850°C time 20 min	536,2	13,9
B8	Homogenized + 850°C time 40min	575,8	9,6
B9	Homogenized + 850°C time 60 min	591,4	13,5
B10	Homogenized + 850°C time 5 min	656,2	10,0
B11	Homogenized + 790°C time 5 min	560,8	8,1
B12	Homogenized + 880°C time 5 min	556,8	10,5
B13	Homogenized + 820°C time 20 min	531,3	12,6
B14	Homogenized + 850°C for 10 min + 600°C for 8h	572,4	17,6
B15	Homogenized + 850°C for 10 min + 600°C for 24h	551,3	19,9

Table 12 Hardness test results for Alnico 2 samples set

5.3 MAGNETIC PROPERTIES TEST RESULTS

Magnetic tests were done on the heat-treated samples and from the beginning the results appeared successful. This is the reason why many samples were treated.

First, all the homogenized samples were tested in order to check if every sample was successfully heat treated. The reason of this analysis is that the chamber for the samples was small so only a couple of samples had been treated at a time. Looking at the hysteresis loops in *Figure 48*, it

emerged that the loops are a bit different but in general it can be stated that the homogenizing step was successful.

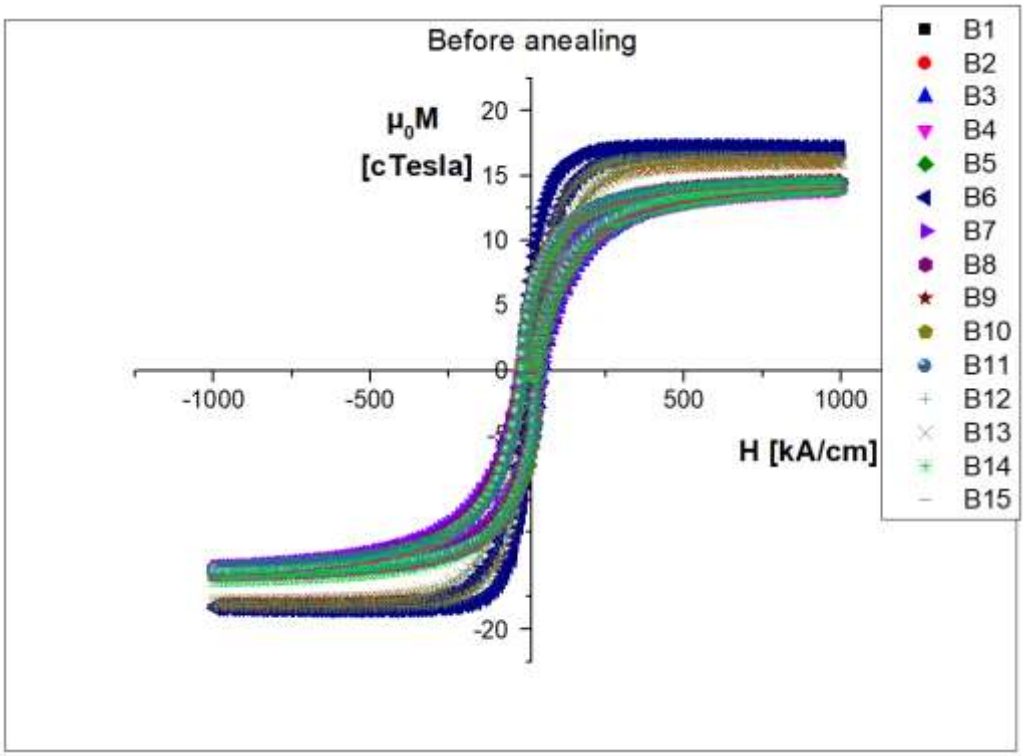

Figure 48 Hysteresis loops of the homogenized samples

Once it was clear that the samples were successfully homogenized, the first five samples were annealed following the already mentioned strategy. The magnetic test results of these samples are reported in the *Figure 49*.

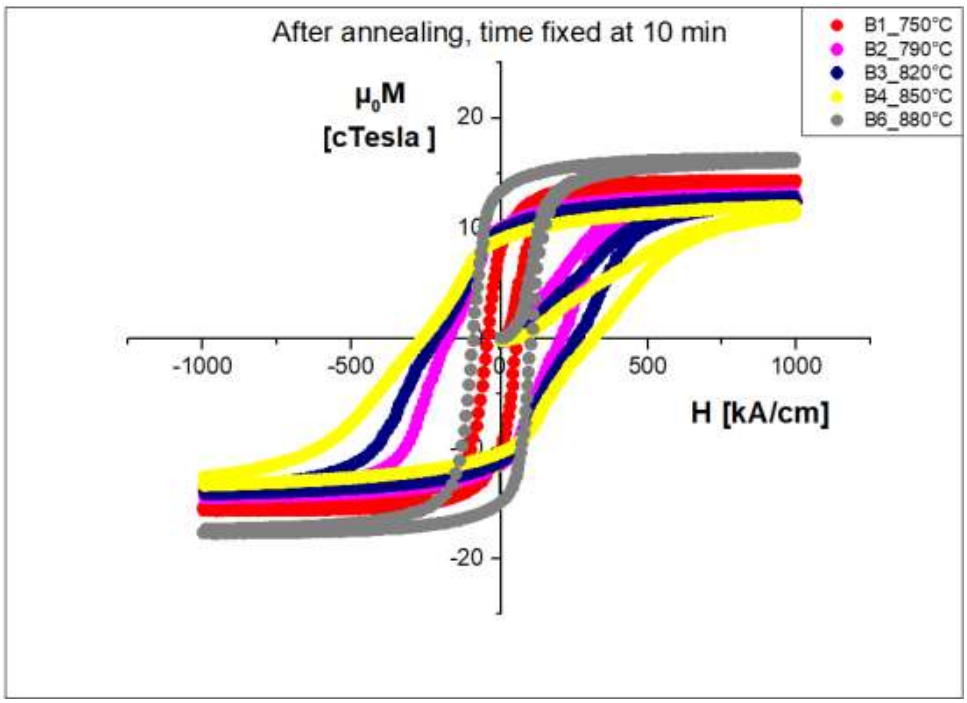

Figure 49: Hysteresis loops of the annealed samples

It can be clearly seen from the hysteresis loops in *Figure 49* that there is a sample (B4) which shows the best coercivity with respect to the other samples. The temperature of this sample was chosen for the further heat treatments where different times were tried. These annealing treatments results are showed in *Figure 50*. It is also interesting to observe how the magnetization decreases when coercivity increases. This aspect has already been treated in the first chapter.

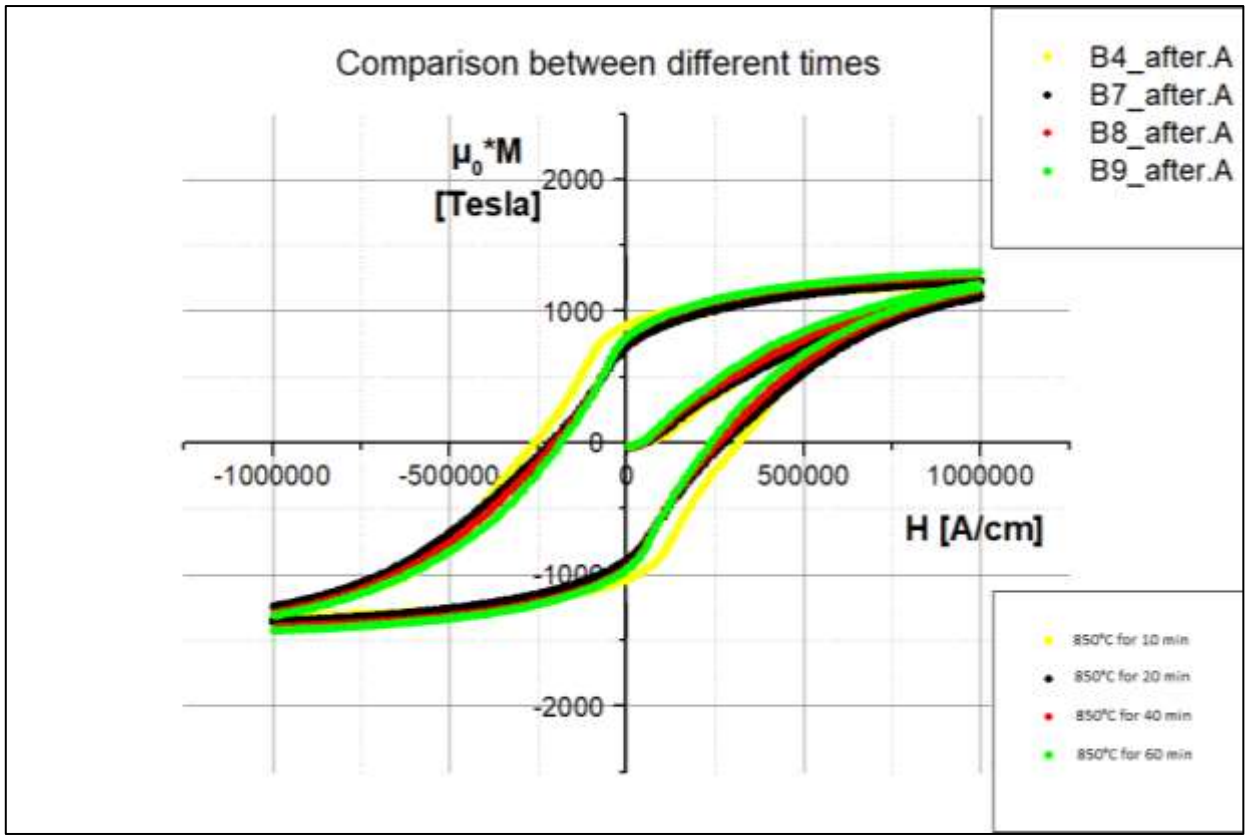

Figure 50 Hysteresis loops of the samples treated at the temperature of 850°C and different times

At this point, several times for the annealing heat treatment were tried and from the magnetic tests it was evident that the best time parameter to develop the highest coercivity was of ten minutes. Thus, after having found both of the two parameters, the annealing step can be considered investigated and done.

The heat treatment, then, is terminated with the drawing step. The last two samples of the set are prepared in order to test two different times. The results showed that sample B14 was the most successful so its hysteresis loop after step drawing is compared in *Figure 51* with the hysteresis loop of the original state sample. It is interesting to observe that a good coercivity had been developed in the sample, even if the original sample coercivity is the best one. This fact is probably due to the better heat treatments that the original sample had been submitted as in industry the companies are much better equipped for this kind of activities.

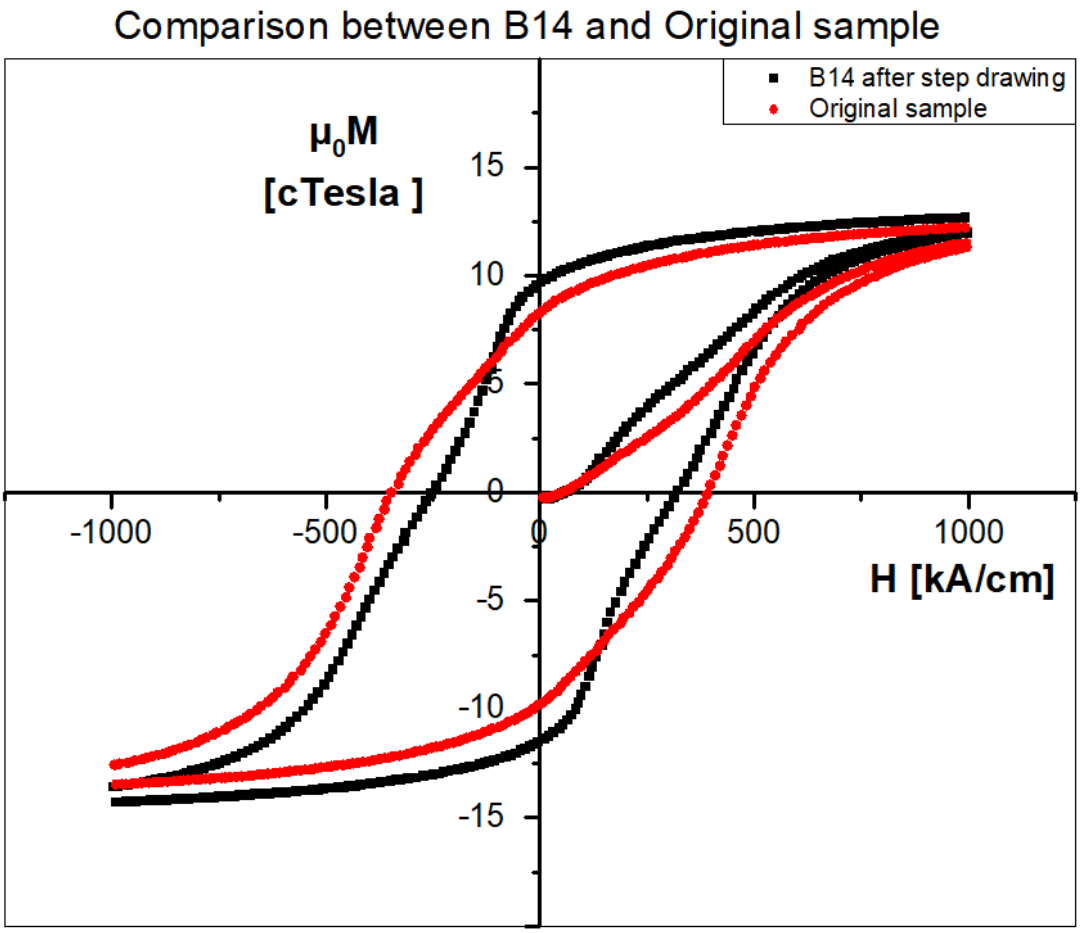

Figure 51 Comparison of the hysteresis loop between B14 and the original sample

5.4 OPTICAL MICROSCOPY RESULTS

The microstructure was observed in order to compare it with the microstructure of the samples of Alnico5 as the compositions of the two alloys are different. The results are the following:

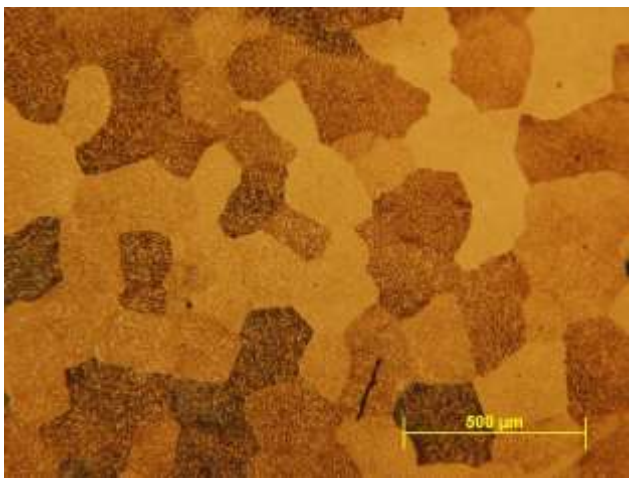

Figure 52: Alnico2 after solubilization heat treatment x50

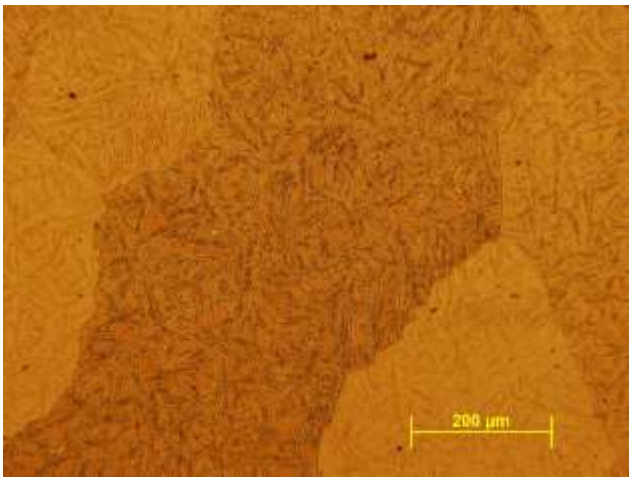

Figure 53 Alnico2 after solubilization heat treatment x10

It is possible to notice from the previous micrographies that there are some important differences in the microstructure between the second set homogenized samples and the first set homogenized samples. The most evident feature is the texture of the grains. First set samples presented a smooth surface inside the grains while the second set samples present a particular texture inside the grains. It's legitimate to state, in this case, that two phases coexist. Nevertheless, this aspect is contradictory as after solubilization heat treatment, according to the phase diagram, only one phase should be present. This aspect is further investigated with electronic microscopy and composition analyses.

5.5 ELETRONIC MICROSCOPY RESULTS

The anomalous microstructure is now investigated with SEM and EDS techniques. The main goal is two discuss why two phases coexist. This can be done starting by measuring the composition of each phase and by comparing them. The results are the followings.

During the electronic microscopy investigation, some black spots were detected again. To be sure about their characterization a composition analyses of these spots, besides of the two phases, was done. In the micrography in *Figure 54* three different spots of the analysis can be observed. These are the spots where composition was detected. Spot 1 is the matrix of the microstructure while spot 2 is one of the precipitated elements, so the second phase. Spot 3 is the black dot.

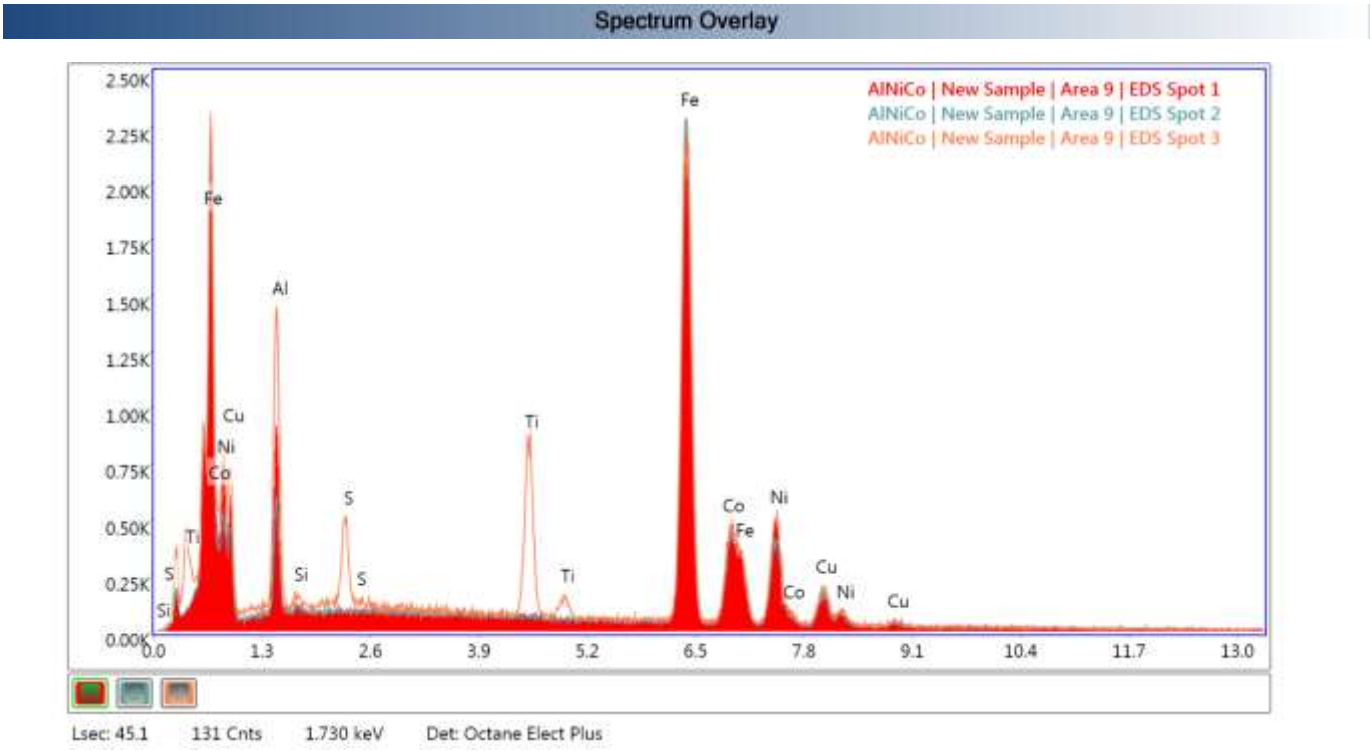

Chart 2 Comparison of the compositions of the 3 spots

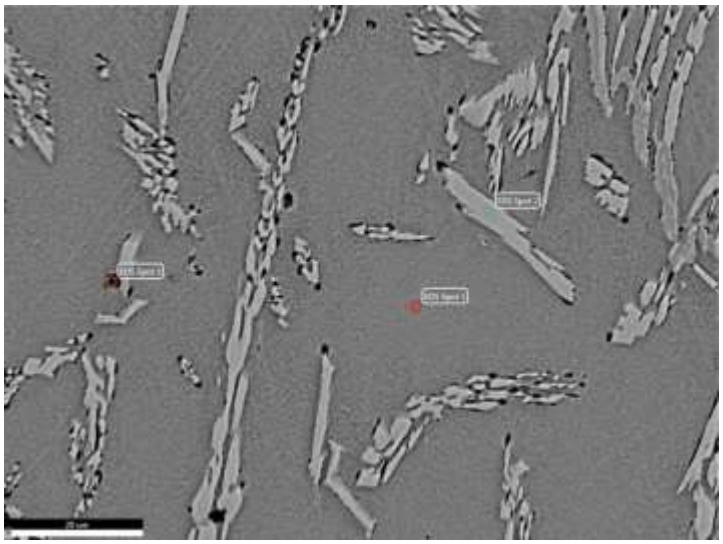

Figure 54: SEM micrography of the homogenized sample

Element	Weight %	Atomic %	Net Int.
AlNiCo | New Sample | Area 9 | EDS Spot 1			
AlK	9.12	17.52	150.07
SiK	0.25	0.45	5.17
FeK	55.75	51.72	720.12
CoK	10.81	9.5	118.24
NiK	17.61	15.54	162.93
CuK	6.46	5.27	48.72
AlNiCo | New Sample | Area 9 | EDS Spot 2			
AlK	5.81	11.52	102.05
SiK	0.28	0.53	6.4
FeK	61.46	58.88	863.15
CoK	10.47	9.51	124.69
NiK	15.33	13.97	153.69
CuK	6.65	5.6	54.4
AlNiCo | New Sample | Area 9 | EDS Spot 3			
AlK	11.84	21.33	230.38
SiK	0.38	0.66	8.98
S K	3.05	4.62	84.85
TiK	8.96	9.09	200.43
FeK	48.03	40.08	636.26
CoK	9.01	7.44	106.12
NiK	14.42	11.94	145.68
CuK	6.32	4.84	52.08

Table 13: EDS composition analysis results

The results of the EDS composition analysis show the compositions of the spots. First of all, the results confirm that the black dots can be linked with sample pollution as sulfur is present. Regarding to the two phases, their compositions are a bit different but still in the range of Alnico 2 alloys. There is no explanation of why two phases were detected in a homogenized sample. Nevertheless, this is not the main topic of the project so no further investigation will be done on it.

6 CHAPTER

THIRD SET OF SAMPLES

New conditions for the heat treatment process were proposed so a new experiment was done on another set of Alnico 5 samples. The conditions of the solubilization heat treatment step are the same as the ones used for the second set of Alnico 2 samples. This means that the homogenizing step was done at 1250°C for 20 minutes in argon atmosphere. The outcome of the experiment is illustrated in the following chapter.

6.1 HEAT TREATMENTS

Regarding to the first set samples, a different schedule of temperature and time parameters was chosen for this set. It has been decided to focus the attention on the same schedule of the Alnico2 samples in order to be free to compare the best parameters and the magnetic properties of the two alloys. The schedule of the annealing treatment parameters is the following.

Sample	Heat treatment
C1	Solubilization + 750°C for 10 min
C2	Solubilization + 790°C for 10 min
C3	Solubilization + 820°C for 10 min
C4	Solubilization + 850°C for 10 min
C5	Solubilization + 880°C for 10 min
C6	Solubilization
C7	Solubilization
C8	Solubilization
C9	Solubilization
C10	Solubilization
C11	Solubilization
C12	Solubilization
C13	Solubilization
C14	Solubilization
C15	Solubilization
C16	Solubilization

Table 14 Time and temperature schedule of the heat treatments for the third set samples

After the first five annealing treatments the magnetic properties were measured, and the experiment turned out to be another failure. Some problems occurred after annealing step, so the heat treatment was stopped afterwards.

6.2 MAGNETIC TESTS

Magnetic measurements were done after the homogenizing step and after the annealing step of the first five specimens. The results are shown and discussed below.

Chart 3 shows several hysteresis curves of the solubilized samples. It's legitimate to state that the first step was successful and the samples present similar curves.

On the other side, *Chart 4* shows that the annealing step did not bring the hoped result. The coercivity was developed but the values of the best samples are not even close to the original sample. This means that the experiment with Alnico 4 samples failed again.

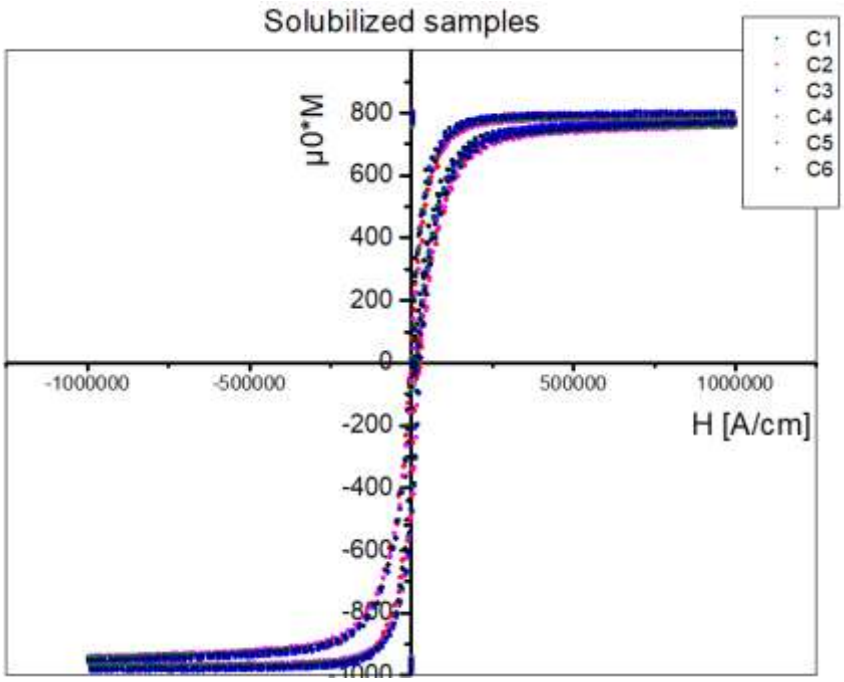

Chart 3 Hystetesis curves of the solubilized samples

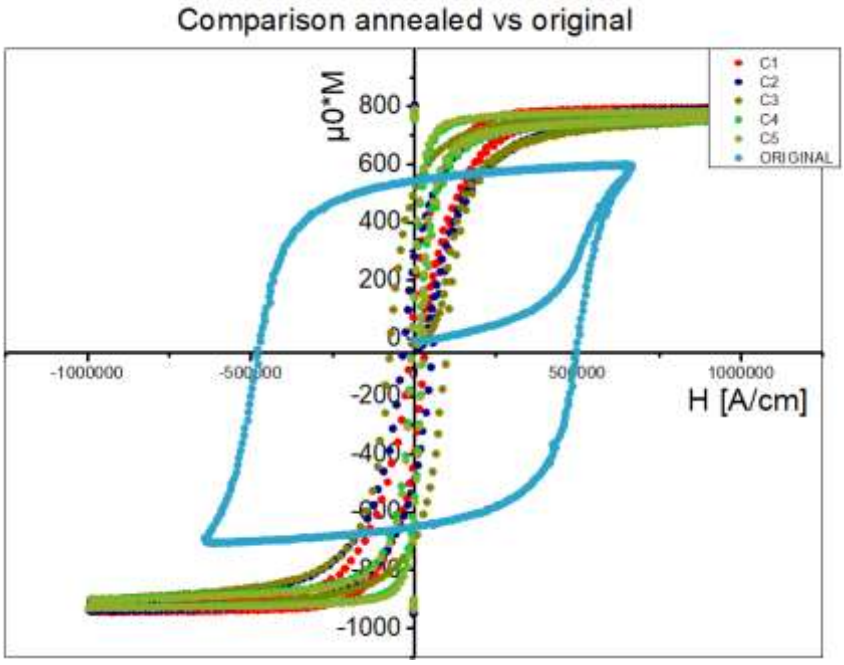

Chart 4 Comparison of the hysteresis curves between annealed samples and the original sample

6.3 CONCLUSIONS

After have changed the conditions of the heat treatments, the coercivity was not developed as it was supposed to do. It is legitimate to consider a failure the experiment with the third set of samples as well. The topic about the possible reasons of the failure had already been discussed in the *Chapter 4,* where several hypotheses were proposed and discussed. This means that something missed in the analysis. As the oxidizing atmosphere and the contact with carbon steel were already discussed, other hypotheses should be done to explain the failure.

In general, various aspects could have contributed to the failure. These can deal with the furnace again, with the temperature program or with the samples. The furnace conditions were already analyzed and there is nothing more to add. Regarding the temperature program, a wide range of temperatures had been proved so about this topic there is nothing to suppose about the failure. Regarding to the samples, finally, the original condition was a magnetic state so with spinodal decomposition occurred and, on the other side, the composition was measured at the beginning, and it respected the ranges of Alnico 5 alloys composition. Nevertheless, in the same conditions the work on the set number two, so with Alnico 2 alloys, was a successful one while the same work on the third set, so Alnico 5, failed. The difference between the two works is the material used so probably that should be the start point of a further investigation.

Another important point of the results is that coercivity increased but of a meaningless amount. So, it can be also possible that the modified furnace with the blowing gas just did not work properly. In this case, the next experiments should be done in a better equipped furnace.

7 CHAPTER

SUGGESTIONS AND CONCLUSIONS

There are many aspects to discuss about as the conclusion of the project. Besides of the study of the spinodal decomposition and developing of the highest values of the coercivity in Alnico alloys, there had also been other investigations on the possible reasons of the failure of the heat treatment. Furthermore, it was already mentioned several times that other techniques were more appropriate, but these ones were not available. Thus, suggestions about other investigations and other techniques will be proposed and discussed at the end of the chapter.

7.1 ALNICO COERCIVITY DEVELOPMENT

The main purpose of the work was to investigate spinodal decomposition which is linked with the development of the coercivity in Alnico alloys. As these alloys are currently important, for the already explained reasons, this study was a side but still significant target of the project.

Unfortunately, the Alnico 5 samples treatment was not successful and the coercivity was not developed as much as it was supposed to do, or it was not developed at all in the case of the first set of the samples. Nevertheless, some important results were obtained with the second set of the samples, so with Alnico 2 alloy. The most important result is shown in *Figure 55.* The hysteresis loop shows that values of coercivity obtained through the heat treatment are very close to the values of the original samples. Furthermore, the original sample derives from a steel company, where the heat treatments were done with specific equipment. The result of this work, then, is considered a great achievement.

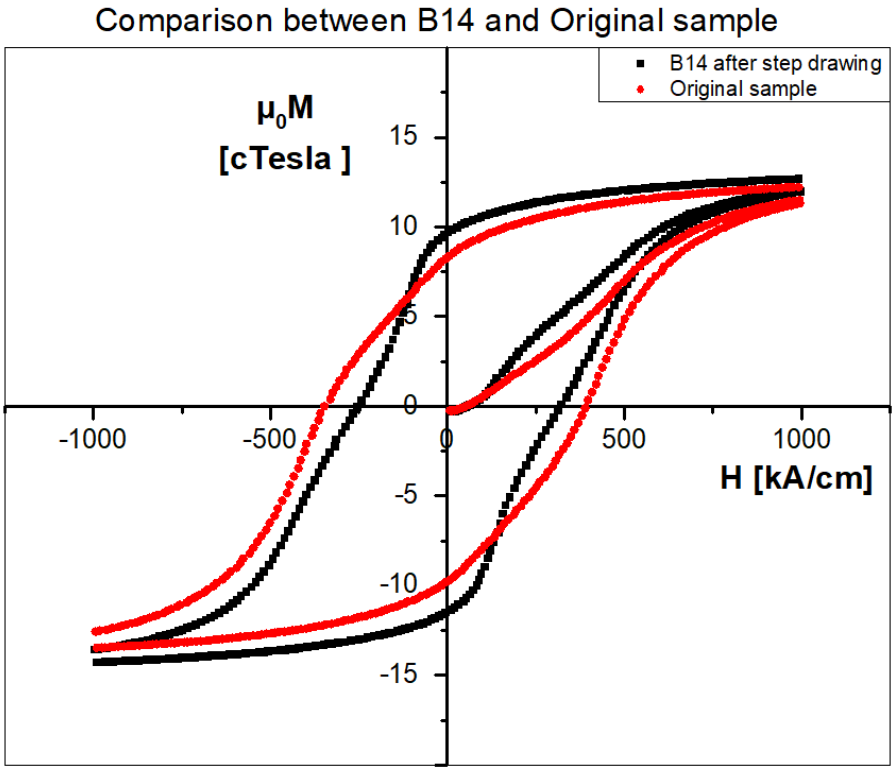

Figure 55 Comparison of the hysteresis loop between B14 and the original sample

7.2 SPINODAL DECOMPOSITION INVESTIGATION

As it has already been mentioned, the spinodal investigation was the main topic of the study. During the introduction to this work the process was deeply discussed, and it came out that of the available investigation techniques, two tests in particular could be used to track the process: hardness test and magnetic test. Both of them are illustrated and discussed below.

7.2.1 Magnetic tests

When spinodal decomposition starts, two different phases appear: α_1 rich in Fe and Co and α_2 rich in Al and Ni. It has already been mentioned that different magnetization of the two phases is extremely important to enhance the magnetic properties. When the samples start the spinodal decomposition process, so to separate in two distinct phases, then the magnetic properties start to be modulated. This is a key point as due to this change in magnetic property values, the spinodal composition can be tracked, measuring the magnetic properties after the annealing heat treatment.

Particular efforts were done in finding the best annealing parameters in order develop the highest coercivity of the samples. But, after having done these experiments, the results can be exploited for another study. With testing several parameters for the annealing step, spinodal decomposition process can be discussed in terms of the conditions required to start it up. In Table *15,* six meaningful samples are shown. Their magnetic properties will be helpful to understand what conditions must be satisfied in order to start the spinodal decomposition process.

Name	Heat treatment
B1	750°C for 10 min
B2	790°C for 10 min
B3	820°C for 10 min
B4	850°C for 10 min
B5	750°C time 20 min
B6	880°C for 10 min

Table 15: annealing parameters of the second set

The magnetic properties, on the other side, are shown in *the* following figures. In *Figure 56,* the first one, samples B1, B2, B3, B4, B6 are compared as these ones are annealed with the same time but different temperatures. The results show the temperature value that is high enough to ensure the diffusive process that gives rise to the phase separation, and the kinetic aspect is also showed. The kinetic aspect is illustrated in *Figure 57* as well, where sample B1 and sample B5 are compared in order to show that the diffusive process can also start at a lower temperature but it needs more time to process.

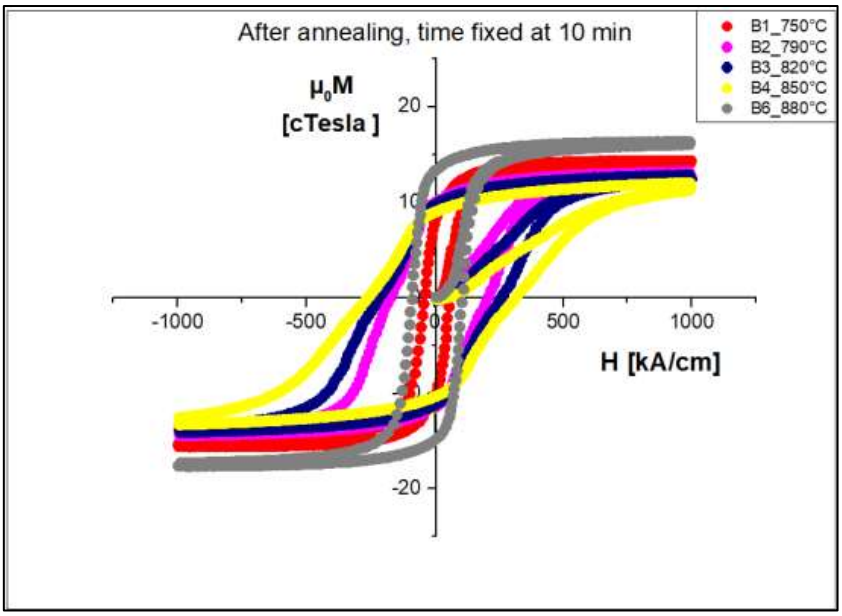

Figure 56 Hysteresis loops of samples with the same annealing time

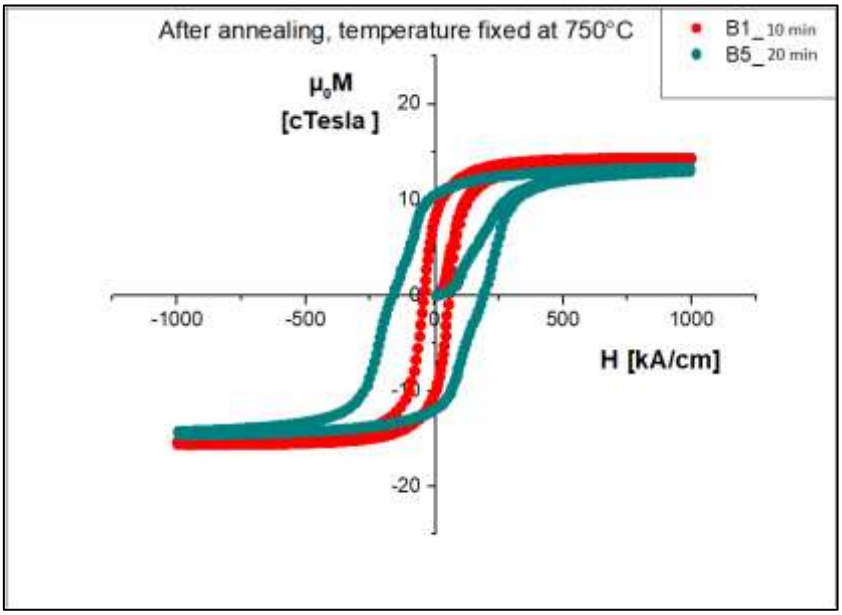

Figure 57 Hysteresis loops of sample B1 and B5

No further heat treatment parameters were explored as the samples of Alnico 2 alloy available for the study were limited.

7.2.2 Hardness tests

During the characterization of the three sets of samples, hardness tests were done as well. Hardness is measured as it is the mechanic property that is the simplest one to obtain. Furthermore, it has already been mentioned that the spinodal decomposition has some benefits on the mechanic properties, so measuring the hardness values could be another way to track the process. The followings studies on the hardness values are done on the second set of samples as that was a successful one.

A good strategy must be planned as it is not sure that there is a correlation between hardness and spinodal decomposition. Furthermore, a correlation between spinodal decomposition and magnetic properties had been confirmed so it is legitimate to work on the correlation between hardness and magnetic properties instead.

The following studies will be based on a strict comparison between hysteresis loops, that are indicators of the spinodal decomposition, and the hardness values of two groups of samples with a characteristic thermal history. The first characteristic group is the set of samples heat treated with different annealing temperatures but a fixed annealing time. These ones are B1, B2, B3, B4 and B6 samples. The second characteristic group is the set of samples which are heat treated with different annealing times but at the same annealing temperature. Finally, the hardness values will be ordered from the highest value to the lowest and it will be checked if a correlation exists following this order.

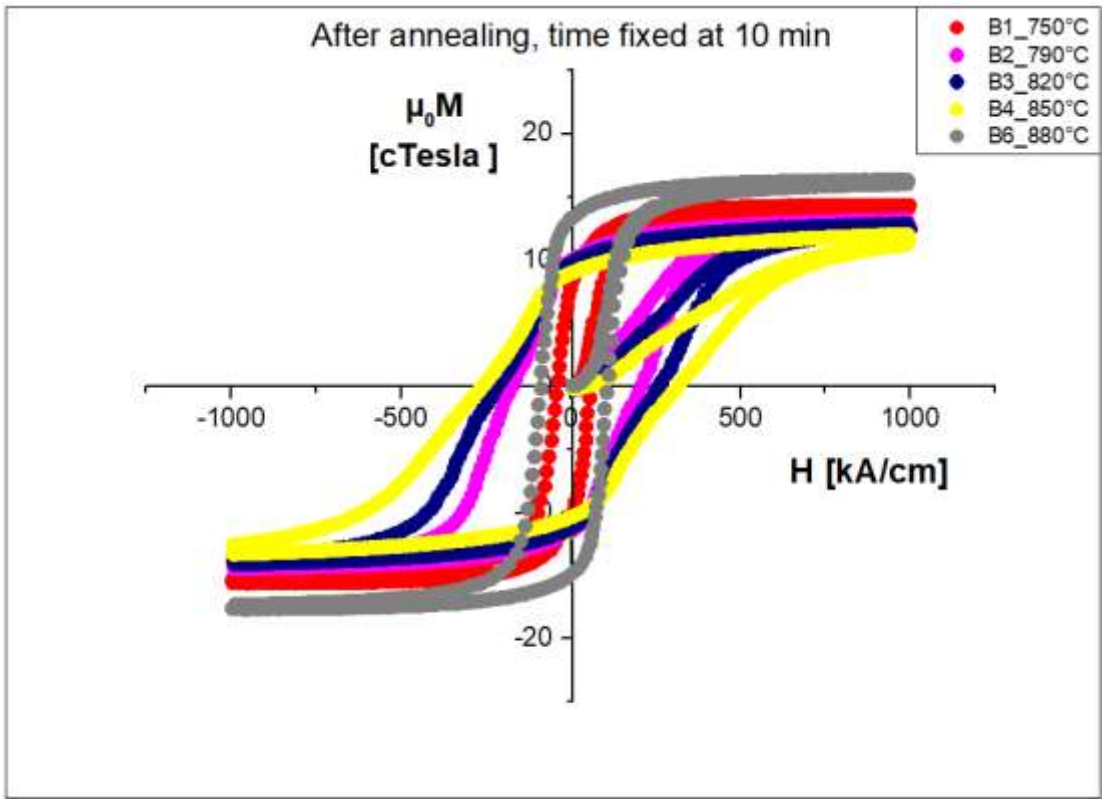

Figure 58 first group of samples

Sample	Annealing	Mean hardness [HV_{30}]	Standard deviation [HV_{30}]
B1	750°C for 10 min	650,4	4,5
B2	790°C for 10 min	597,7	8,5
B3	820°C for 10 min	573,4	5,8
B4	850°C for 10 min	561,0	11,5
B6	880°C for 10 min	522,7	39,2

Table 16 first group of samples

Once the results of the magnetic tests and hardness tests have been introduced, a comparison between them must be done. The strategy is to put in a decreasing order, so from the highest value to the lowest value, the coercivity and the hardness and to see if there is a difference between the samples order with these two criteria. This work is done in the following table.

Coercivity order		Hardness order
B4 (850°C)		B1 (750°C)
B3 (820°C)		B2 (790°C)
B2 (790°C)		B3 (820°C)
B6 (880°C)		B4 (850°C)
B1 (750°C)		B6 (880°C)

Table 17 Comparison between coercivity and hardness values

After a careful observation two aspects seem to be evident. The first one is that the hardness decreases when the annealing temperature of the heat treatment increases. This correlation fits the theory of the annealing heat treatment during which one the mechanic properties of the alloy tend to decrease because of the softening process. The second aspect to be noted is that there is no evident correlation between the hardness and the coercivity of the samples. That means that the first try to find a correlation between hardness values and the spinodal decomposition failed.

The second attempt is based on the comparison between hardness values and the coercivity of the samples heat treated at the same annealing temperature but with different annealing times. There is no dependency on the temperature but still the softening effect should be considered as it depends also on the time. Nevertheless, the study is done, and the results are illustrated and discussed below.

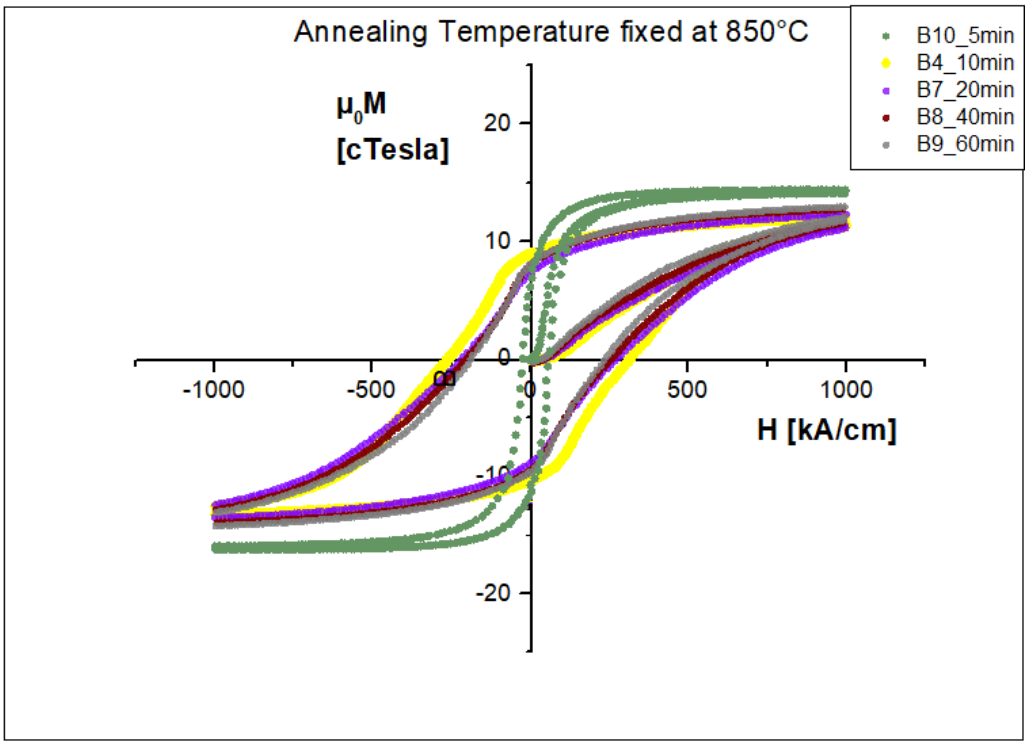

Figure 59 Second group of samples

Sample	Annealing	Mean hardness [HV_{30}]	Standard deviation [HV_{30}]
B10	850°C time 5 min	656,2	10,0
B4	850°C for 10 min	561,0	11,5
B7	850°C time 20 min	536,2	13,9
B8	850°C time 40min	575,8	9,6
B9	850°C time 60 min	591,4	13,5

Table 18 second group of samples

As it was done previously, a comparison table is built and the results are reported below. The values of the properties are ordered again from the highest value to the lowest.

Coercivity		Hardness [HV_{30}]
B4		B10 (5min)
B7		B9 (60min)
B8		B8 (40min)
B9		B4 (10min)
B10		B7 (20min)

Table 19 Second group comparison between magnetic and hardness orders of values

Looking at the orders of the properties an inverse correlation between them can be supposed. It seems that lowest values of hardness correspond to the highest values of coercivity. Furthermore, it is interesting to notice that there is no correlation between annealing and softening as the hardness values don't follow the annealing times. Nevertheless, both factors, so the spinodal process and softening, can impact in the correlation so another study, a deeper and more accurate one, should be done. At this moment, the supposition on the correlation between hardness and spinodal process is only accepted.

Finally, the last try is going to be done. This one concerns in putting in order the hardness values from the highest one to the lowest one and to check if any correlation can be deducted. This procedure is done and it is illustrated in the following tables and graph.

Table 20 Risultati investigazione ordine della durezza

Hardness order	Hardness [HV_{30}]
B10	656,2
B1	650,4
B2	597,7
B5	592,2
B6	592,2
B9	591,4
B8	575,8
B3	573,4
B4	561
B11	560,8
B12	556,8
B13	531,28
B7	522,7

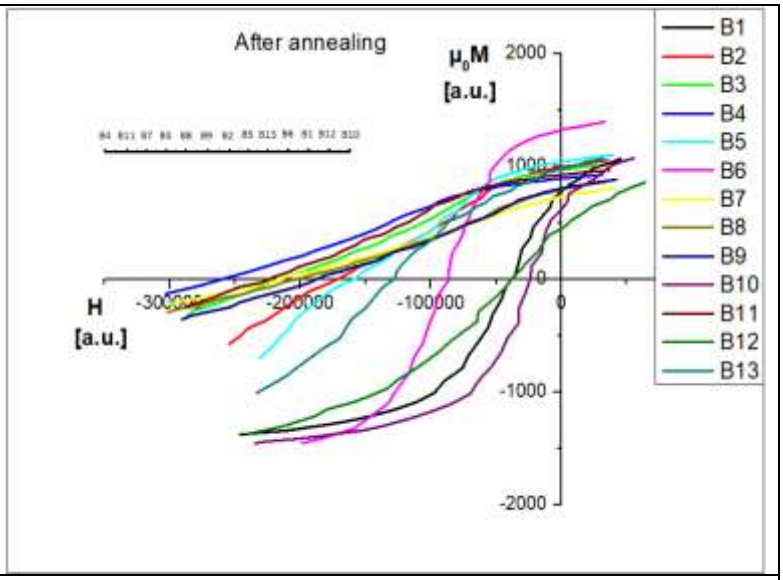

Coercivity order	B4	B11	B7	B3	B8	B9	B2	B5	B13	B6	B1	B12	B10
Hardness order	B10	B1	B2	B5	B6	B9	B8	B3	B4	B11	B12	B13	B7

As it can be seen from the *Table 20*, no evident correlation is found between hardness values order and coercivity order. This result completes the investigation. A discussion on all the results must be done.

The strategy of the three different comparisons had as the outcome no evident correlation between hardness and coercivity. This means that the spinodal process indirect tracking, considering the mechanic properties, had no success. Nevertheless, these results do not fit the theoretical background as the spinodal process can be used to enhance the mechanic properties.

There is an important aspect that must be taken in consideration. The spinodal decomposition process occurs at the nano scale level while the hardness tests are done with an indenter that has

dimensions in the range of micrometers. This means that the measurements and the results must be confirmed or refuted by more precise and accurate measurements using the micro and nano hardness tests.

7.3 SUGGESTIONS FOR FURTHER INVESTIGATIONS

The study is terminated but the results are not enough to track the spinodal decomposition. Magnetic tests proved that the process occurred but, for instance, if it was necessary to prove the Cahn equation on this experiment than the information would not have been enough at all. For this reason, some other investigation techniques are suggested in order to complete the following study.

Three techniques are suggested in order to obtain more useful results. These are Seebeck measurements, atomic force microscopy and neutron diffraction. Some technical aspects will be introduced about these techniques and the possible results will be explained.

7.3.1 Seebeck Measurement

A way to define the Seebeck coefficient is the voltage accumulated when a small temperature gradient is applied to a material and when the material has reached a steady state in which the current density is zero everywhere. If the temperature difference Δ T between the two ends of a material is small, the Seebeck coefficient of a material is defined as:

$$S = -\frac{\Delta V}{\Delta T} \tag{21}$$

where ΔV is the thermoelectric voltage seen at the terminals. Each material has a certain Seebeck coefficient corresponding to it.[38] This value is strictly related to its microstructure and to its magnetic properties. Thus, measuring a two-phase material, it is possible to establish the quantity of the two phases.

In case of Alnico alloys, where the spinodal decomposition generated the separation into two phases, this measurement can quantify the relationship between the α_1 and α_2 phases. The device for the measurement is even available for the testing, but unfortunately, the shape and the dimensions of the samples are not appropriate. Slender specimens are required, instead of the cubic shape ones. Thus, the Seebeck coefficient could not be measured and the two phases could not be quantified.

7.3.2 MAgnetic Force Microscopy (AFM)

Atomic force microscopy (AFM) or scanning force microscopy (SFM) is a very-high-resolution type of scanning probe microscopy (SPM), with demonstrated resolution on the order of fractions of a nanometer, more than 1000 times better than the optical diffraction limit. The information is gathered by "feeling" or "touching" the surface with a mechanical probe. Piezoelectric elements that facilitate tiny but accurate and precise movements on (electronic) command enable precise

scanning. Despite the name, the Atomic Force Microscope does not use the nuclear force. Magnetic force microscopy (MFM) is an atomic force microscopy (AFM) application that is widely used to characterize magnetic properties of various materials at the nanoscale. In this technique, a sharp tip coated with ferromagnetic material scans the surface and maps the distribution and strength of magnetic domains on the sample.[37]

In case of Alnico alloys and spinodal decomposition, Magnetic force microscopy could be used in order to provide the morphology of the two phases at the nanoscale detecting their difference in magnetic properties.

7.3.3 Neutron Diffraction

Neutron diffraction or elastic neutron scattering is the application of neutron scattering to the determination of the atomic and/or magnetic structure of a material. A sample to be examined is placed in a beam of thermal or cold neutrons to obtain a diffraction pattern that provides information of the structure of the material. The technique is similar to X-ray diffraction but due to their different scattering properties, neutrons and X-rays provide complementary information: X-Rays are suited for superficial analysis, strong x-rays from synchrotron radiation are suited for shallow depths or thin specimens, while neutrons having high penetration depth are suited for bulk samples. Although neutrons are uncharged, they carry a magnetic moment, and therefore interact with magnetic moments, including those arising from the electron cloud around an atom. Neutron diffraction can therefore reveal the microscopic magnetic structure of a material.[39]

Once again, in case of Alnico alloys, this investigative technique could be useful to detect the two phases at the nano scale level.

8 REFERENCES

[1] P. ZOTTO, S. LO RUSSO, P. SARTORI, *Fisica Generale: elettromagnetismo-ottica,* Ed. La Dotta, 2018.

[2] A. GUSAK, KING-NIANG TU, *Kinetics in Nanoscale Materials, Chapter Spinodal Decomposition,* 1st Ed. 2014.

[3] B.D. CULLITY, C. D. GRAHAM, *Introduction to Magnetic Materials,* 2nd Ed. 2009.

[4] GEORGE F. VANDER VOORT, *ASM Handbook Metallography and Microstructures,* Vol. 8, 2004.

[5] SOPHIA KALANTZAKOS, *Terre rare: la Cina e la geopolitica dei minerali strategici*, 2020.

[6] G. KOSTORZ, *Phase transformation in materials*, *Spinodal Decomposition Chapter*.

[7] FEHIM FINDIK, *Modulated (Spinodal) Alloys,* Periodicals of Engineering and Natural Sciences, Vol. 1, 2013. [1.1]

[8] V. A. HOSSEINI, M. THUVANDER, S. WESSMAN, L. KARLSSON, *Spinodal Decomposition in Functionally Graded Super Duplex Stainless Steel and Weld Metal,* Metallurgical and Materials Transactions, 2018. [1.2]

[9] E.P. FAVVAS, A. CH. MITROPOULOS, *What is spinodal decomposition*, Journal of Engineering Science and Technology Review (2008) pp. 25-27. [1.4]

[10] M. FAN, Y. LIU, R. JHA, G.S. DULIKRAVICH, J. SCWARTZ, C.C. KOCH, *On the Evolution of Cu-Ni-rich bridges of Alnico alloys with tempering,* Journal of Magnetism and Magnetic Materials, 2016. [2.1]

[11] J.T. ZHAO, Y.L. SUN, L. LIU, D. LEE, Z. LIU, X.C. FENG, A.R. YAN, *Correlations of phase structure and thermal stability for Alnico 8 alloys,* Journal of Magnetism and Magnetic Materials, 2017. [2.2]

[12] L. ZHOU, W. TANG, L. KE, W. GUO. J. D. POPLAWSKY, I.E. ANDERSON, M.J. KRAMER, *Microstructural and magnetic property evolution with different heat-treatment conditions in an alnico alloy,* Acta Materialia, 2017. [2.3]

[13] L. K. KE, R. SKOMSKI, T. D. HOFFMAN, L. ZHOU et al, *Simulation of alnico coercivity, 2018.* [2.4]

[14] L. ZHOU, W. TANG, W. GUO et al, *Spinodal Decomposition in an Alnico Alloy,* Microscopy Society of America, 2016. [2.5]

[15] Z. RAO, B. DUTTA, F. KORMANN, W. LU et al, *Beyond Solid Solution High-Entropy Alloys: Tailoring Magnetic Properties via Spinodal Decomposition,* Advanced Functional Materials, 2020. [2.6]

[16] M. STANEK, L. WIERZBICKI, M. LEONOWICZ, *Investigation of Thermo-Magnetic Treatment of Alnico 8 Alloy,* Archieves of Metallurgy and Materials, Vol. 55, 2010. [2.7]

[17] K. LOWE, M DURRSCHNABEL, L. MOLINA-LUNA et al, *Microstructure and Magnetic Properties of Melt-Spun Alnico 5 Alloys,* Elsevir Ed., 2015. [2.8]

[18] C. M. ELLIOT, *The Cahn-Hillard Model for the Kinetics of Phase Separation,* International Series of Numerical Mathematics, Vol. 88, 1989. [3.1]

[19] Y. IWAMA, M, TAKEUCHI, *Spinodal Decomposition in Alnico 8 Magnet Alloy,* 1974. [3.2]

[20] L. ZHOU, W. GOU, J. D. POPLASWKY et al, *On Spinodal Decomposition in Alnico-a Transmission Electron Microscopy and Atom Probe Tomography Study,* Acta Materialia, 2018. [3.3]

[21] J. B. ALDABBAGH, I. JASSIM, I. ODEH, *Effect of Annealing Temperature on Magnetic and Structural Properties of ALNICO-5 Alloy,* International Conference on Nanotechnology and Biosensors, 2011. [4.1]

[22] A. S. RAO, *Alnico Permanent Magnets, An Overview,* Thomas & Skinner, Inc. Indianapolis, Indiana. [4.2]

[23] E. R. CRONK, *Recent Developments in High-Energy Alnico Alloys,* Journal of Applied Physics, 1966. [4.3]

[24] X. YU, S. CHEN, F. GU et al, *Preparation of Alnico magnet with high magnetization by thermal deformation,* Materials Letters, 2021. [4.4]

[25] L. ZHOU, P. LU, M. K. MILLER et al, *Architecture and magnetism of alnico,* Acta Materialia, 2014. [4.5]

[26] B. BÖGRE, I. MÉSZÁROS, *Problems of Ferrite Content Determination,* 2020. [110]

[27] R. GLAS, O. BLASCHKO, *Structure functions in decomposing Au-Pt systems,* Physical Review B, 1992.

[28] KAREN SMITH STEGEN, *Heavy rare earths, permanent magnets, and renewable energies: An imminent crisis,* Elsevier, 2014. [6.1]

[29] DEVIN POWELL, *Sparing the rare earths: Potential shortages of useful metals inspire scientists to seek alternatives for magnet technologies,* Science News, 2011. [6.2]

[30] V. JANOS, *Alnico 5 investigations, 1984. [106]*

[31] G.M. COPPARI, *thesis on Spinodal Decomposition: Analisys Of The Process And Numerical Simulation*, University of Bologna 2020. [103]

[32] E. POŠKOVIĆ, *Thesis on Innovative Magnetic Materials for the New Applications in Electrical Machines*, University of Padua, 2019. [104]

[33] *Lecture 22: Spinodal Decomposition*, University of Utah's College of Engineering, 2004. [1.3]

[34] J.W. GIBBS, *Collected Works*, Yale University Press, New Haven, pp-105-115 (1948). [101]

[35] D.A. PORTER, K. E. EASTERLING AND M.Y. SHERIF, *Phase Transformation in Metals and Alloys*, CRC Press, third edition [102]

[36] I. Calliari, *Dispensa appunti sulla microscopia elettronica.*

[37] https://en.wikipedia.org/wiki/Atomic_force_microscopy

[38] https://en.wikipedia.org/wiki/Seebeck_coefficient

[39] https://en.wikipedia.org/wiki/Neutron_diffraction